SYNTHETIC REALIZATION OF OCEAN TURBULENCE ACROSS MULTIPLE SCALES

by

Kara Shipley

A portfolio submitted to Johns Hopkins University in conformity with the requirements for the degree of Doctor of Engineering

Baltimore, Maryland

August 2021

Abstract

This work is in the area of ocean flows with the objective of generating synthetic velocity and density fields. The smallest scales are implemented using a modified version of the Minimal Multiscale Lagrangian Map (MMLM) approach, a synthetic turbulence realization technique which generates isotropic non-Gaussian intermittent velocity fluctuations (Rosales and Meneveau, 2006). An anisotropic scalar density forcing term is added to the MMLM approach to account for the interaction of buoyancy and shear forces. The resulting small scale velocity and density fields exist on a uniform grid with a limited spatial extent. A tiling and down sampling technique is used to generate larger fields (300 m horizontal x 300 m horizontal x 25 m vertical) with approximately 1 m horizontal and 10 cm vertical resolution. Additional spatial variability and turbulent patches are added to the realization through kinetic energy dissipation rate specification, accounting for the non-uniform energy production and dissipation in the ocean. Finally, the realization is merged with larger-scale fields generated using an existing Garrett-Munk internal wave model to add in the effects from larger scales. The resulting synthetic turbulence realization compares favorably to ocean data for both the density and velocity fields, based on the spectra and observed gradients. This approach comes at a significantly reduced computational cost (40-80x reduction) when compared with more traditional Large Eddy Simulation (LES) modeling techniques.

Thesis Committee

Primary Readers

Charles Meneveau (Primary Advisor)
Louis M. Sardella Professor
Department of Mechanical Engineering
Johns Hopkins Whiting School of Engineering

Dennice Gayme
Associate Professor
Department of Mechanical Engineering
Johns Hopkins Whiting School of Engineering

Scott Wunsch
Principal Professional Staff
Force Projection Sector
Johns Hopkins University Applied Physics Laboratory

Intended to be blank.

Acknowledgments

Over thirteen years ago I graduated college with my Bachelor's of Science in Physics. I had several co-ops which lead me to love hands-on learning with real applications. My first mentor, Dr. Marc Litz of the Army Research Laboratory, encouraged me to find a job and pursue higher education simultaneously. As a result, my first post-college resume objective was to acquire a research position and pursue a PhD in physics. I came to work at JHU/APL with that resume and earned my Master's Degree in Mechanical Engineering (which was more applicable to my work than Physics) shortly thereafter through a part time program. After that time, life became more chaotic and I didn't think I was going to pursue my doctorate. When the JHU Doctor of Engineering was first announced, Dr. David Porter came to me and said I would be a great candidate. I thoroughly appreciate his push and vote of confidence without which I may not have made the leap into this program.

I'd like to thank my JHU advisors Dr. Charles Meneveau and Dr. Dennice Gayme. They have provided immeasurable guidance and support during my research and set me up for success by ensuring I had a solid learning foundation. I also would like to acknowledge when they agreed to be my advisors, the topic of my dissertation was on a completely different topic and their flexibility is greatly appreciated.

I've had tremendous support from colleagues at JHU/APL. I'd like to thank Dr. Alan Brandt for starting me on my advising journey and Dr. Scott Wunsch for stepping in after Alan's well deserved retirement. Work on this topic would not have been possible without a brainstorming session with

Dr. Steve Scorpio. Dr. Matthew Paoletti did some of the initial exploration with the Minimal Multiscale Lagrangian Map which provided a solid basis to launch this work from. I'd like to thank Jeremy Bruch and Dr. Amanda O'Rourke who run the Garrett-Munk internal wave code and Dr. Kurt Keller, Dr. D. Curtis Saunders, and Jeremy Bruch who were involved in the collection of data used for comparison and provided sage council when I was making the comparisons. I appreciate the consult on spectral processing from Howard Schoeberlein and Dr. Jonathan Ligo who helped me troubleshoot my analysis.

My participation in this program would also not have been possible without the love and support from my husband, Christoph, my now 6(!) year old daughter, Beryl, and my now 2(!) year old son, Eigen, my production baby, who was more influential of my journey than he will know.

Thanks!

Table of Contents

List of Tables

List of Figures

Chapter 1

Introduction

Oceanic internal waves are known to occupy a frequency continuum over approximately 6 octaves which extends from inertial to buoyant frequencies [1]. Gyre and overturning circulations fill entire ocean basins, while three-dimensional turbulence reaches down to millimeter scales [2].

This work generates synthetic velocity and density fields which incorporates multiple ocean scales. Synthetic turbulence generally refers to the calculation of field variables (e.g., velocity and density) having characteristic features of turbulent fluctuations that are obtained at a reduced computational cost in comparison with a formal numerical solution of the full Navier-Stokes equations [9].

The relative scales of oceanic structures in are given in Table 1.1. The gross structure and mesoscale regimes describe features such as internal tides (geostrophic eddies) which drive turbulence through the production of turbulent kinetic energy on a large scale [1]. These eddies are strongly constrained by the earth's rotation and the ocean's stratification, evolving typically over weeks to months [2] . Mesoscale eddies are dynamically well understood and are routinely observed with satellite altimeters.

The submesoscale is defined as horizontal ocean flows nominally in the range of 100 m to 10 km. Energetic submesoscale flows produce much larger vertical velocities than mesoscale eddies, consisting of narrow horizontal

Table 1.1: Scales Terminology [1–3]

Horizontal Scales	
Terminology	**Scale**
Mesoscale	10-100 km horizontal
Submesoscale	100 m-10 km horizontal
Microscale	less than 100 m horizontal
Vertical Scales	
Terminology	**Scale**
Gross structure	larger than 100 m vertical
Fine structure	1 m to 100 m vertical
Microstructure	less than 1 m vertical

currents associated with strong horizontal gradients in buoyancy [2, 4]. Submesoscale currents are prevalent throughout the ocean [5] and have been shown to have seasonal dependence (in contrast to mesoscale eddies which tend to be season agnostic and remain roughly constant throughout the year) [2]. Submesoscale features tend to have strong anisotropy [3].

Fine structure in the ocean, referring to scales from approximately 1 m to 100 m vertically, is typically dominated by internal wave straining [1]. Fine structure can be considered with two separate driving processes. The most common process is reversible distortions, where shear and straining from internal waves result in no mixing. The second fine scale process is irreversible, where an occasional mixing event alters the temperature profile [6]. Even so, the irreversible mixing in the thermocline produces relatively minor changes in the stratification with a very small increase in potential energy. Considering fine structure mostly reversible and uniform is a good approximation at scales larger than 2 m [6].

Anisotropy extends beyond the fine structure into the microstructure, down to dissipation scales (on the order of 1 cm) [1]. The deep ocean turbulent microstructure occurs intermittently and in patches [7]. These tend to be thin and elongated horizontally, and are often associated with internal wave activity [8]. This anisotropic patchiness and variability is present even in the

mean on microstructure scales, despite a relatively uniform fine structure [1]. Regions of increased turbulence intensity tend to have a higher energy flux rate as compared to smaller scales originating from them, and consequently the resulting smaller scales at these particular locations are more active [9].

The mean-square gradients largely reside in microstructure and microscale domains. Processes at these scales are vital components of ocean dynamics and have been observed to be concentrated in patches [1]. Microstructure scale activity in the ocean may be caused by a number of physical processes, such as breaking internal waves, shear instabilities, or double-diffusive effects such as salt fingering. These processes can produce compact regions of very high activity at short horizontal and vertical scales with strongly non-stationary statistics [1]. The degree of non-stationarity can depend strongly on location, season, and depth.

Different physics dominate at different wavenumbers. The most general division is between turbulence at small scales and non-turbulent motions, usually internal waves, at larger scales [10]. However, there is a strong correlation between breaking internal waves and the microstructure of density and velocity [1]. Breaking internal waves can modify the density profile and reduce gradients in turbulent patches while sharpening them elsewhere, leading to a steppy fine structure. Internal wave shear is concentrated at the steps, thus producing conditions for shear instability, and renewed breaking [1]. Doubling of the mean internal wave energy can lead to a large increase in the occurrence of breaking events and similarly, halving the wave energy can reduce the probability of breaking to very low levels [1].

There are two limiting forms of instability which may lead to internal wave breaking: advective instability and shear instability [1]. With advective instabilities, breaking occurs from existing large amplitude internal waves and steep isopycnal slopes leading to a local density inversion as the particles in the wave crest are advected forward of the crest. This can occur with or

without ambient shear. Shear instabilities, on the other hand, require a shear to exist in the wave background but can take place without the presence of internal waves [1]. In many cases, the shear experienced by a small internal wave is due to a much larger internal wave and represents a wave-wave interaction.

Energy from larger scales of shear and turbulence may be released at smaller scales through the dissipation of turbulent kinetic energy and the generation of a stabilizing buoyancy flux during the breakdown of Kelvin Helmholtz (K-H) billows [11]. DeSilva et al. (1999) observed this type of finescale density microstructure and small scale turbulence within the billows of laboratory generated K-H billows [11]. They saw a marked rise of spectral density at higher frequencies (larger than the buoyancy frequency, N) which could not be caused by internal waves propagating along the stratified layer (since the stratified layer cannot support propagating waves larger than N). The rise was instead attributed to internal waves excited by the free-stream turbulence associated with K-H billowing and small scale turbulence which can be explained with two disparate models: the billows are turbulent from the onset of their roll up, or conversely, that the billows breakdown into turbulence at an intermediate stage of evolution [11].

The Richardson number is often cited as a fundamental measure of stability and mixing [12]. Billows occurring at low Richardson number have been widely observed in oceans and lakes [12]. Estimates of the variation in Richardson number can be used to determine the rate of dissipation of turbulent kinetic energy per unit mass, ϵ, and the vertical eddy diffusion coefficient for heat, K_v, by empirical but well-established formulas [12].

Shear instabilities are thought to be an efficient energy dissipating mechanism in oceans [11]. Oceans dissipate energy and accomplish mixing in distinct regions when the Richardson number, Ri, drops below the critical value, Ri_c, where elsewhere Ri is typically close to (but larger than) the

critical value Ri_c [11]. A common value for Ri_c is $\frac{1}{4}$. DeSilva et al. (1999) observed that the drop of Ri below the critical value itself was not necessarily alone enough to lead to K-H overturning and instead there may be some time dependence on instabilities since the structures are intermittent and are advected by the the mean flow [11]. This is consistent with Thorpe and Jiang (1998) who specify that Ri instabilities have a finite growth rate and overturning of billows does not occur instantaneously with a drop in Richardson number [12].

Double diffusive effects also occur in the ocean which can invert the traditional theory of turbulence cascading from larger scales down to smaller scales. Processes such as salt-fingering, found in tropical oceans, or thermohaline staircases, found in polar waters, take a static fluid and initiate small scale turbulent convection which grows to larger scales [13, 14]. These effects will be excluded from the implementation discussed herein.

Regarding the flow structure at the microscales, Kolmogorov's 1941 version of his theory suggests mixing is so large that fluctuations in the inertial range are smoothed and only the average rate of dissipation is relevant to represent the rate of local energy cascade [7]. Since then, a number of different intermittency models have been introduced recognizing that turbulence is not homogeneous and isotropic at these scales and stratification of the ocean further weakens the validity of these assumptions. Inertial range (fine scale) intermittency is an important topic in the modern theory of turbulence, as it represents a departure from the 1941 Kolmogorov theory [9]. Meneveau and Sreenivasan [7] discuss a number of these early models for energy dissipation and the resulting intermittency.

It has been shown that the probability density function (PDF) of the small scale velocity fluctuations includes information about the large scale dynamics [15]. Modeling of small scales by a traditional large eddy simulation (LES) is currently limited by the resolution, nominally 30 m in the horizontal and

10 m in the vertical [16]. Understanding and accurately modeling the generation of three dimensional, vector valued, divergence-free functions that reproduce non-Gaussian statistics, intermittency, and nontrivial skewness remains a challenge [17]. The aim of this work is not to reproduce each of the phenomena discussed above in detail, but for practicality reasons, to propose a single method to introduce variability, intermittency, non-Gaussian statistics that is meant as a surrogate model for many of these effects while efficiently coupling the large scale and small scale dynamics.

There is no single, universal model for turbulence due to its complexity, and instead the most common approach to understanding turbulence is through the development of models for specific properties of interest [16]. Various attempts have been made to describe turbulence by using scale dependent stochastic models [15]. However, such stochastic models typically generate time series for a single velocity component or velocity increments that do not describe full 3D vector fields with multiple components and realistic levels of anisotropy [16].

This work discusses the method by which turbulence was synthetically generated at multiple scales (submesoscale / microscale and fine structure / microstructure) using and expanding upon existing models and approximations, while capturing the intermittency and non-Gaussianity observed in the ocean and subsequently favorably compared against ocean data.

Chapter 2 of this document describes the process used to generate a synthetic turbulence realization and includes discussion on the models and scales incorporated into the realization, including information on a Garrett-Munk internal wave simulation from which submesoscale and fine structure features are generated. The extension of the minimal multiscale Lagrangian map (MMLM) approach [17] to include the forcing from buoyancy, referred to as MMLM+density, is discussed in Chapter 3, from which information on the microscale and microstructure are introduced. Chapter 4 discusses the

methodology behind parameter estimation to link multiple models together. A limited number of MMLM+density realizations are then used to generate significantly larger fields via "tiling", as presented in Chapter 5. Details and results from the merging of a Garrett-Munk internal wave simulation (discussed in Chapter 2) with the tiled MMLM+density model (Chapter 5) plus consideration for turbulent energy production and dissipation can be found in Chapter 6. The resulting synthetic turbulence realization has been compared against oceanic probe data (Chapter 7). Chapter 8 provides a summary of this work.

Chapter 2

Synthetic Turbulence Generation Process

The term synthetic turbulence is used to refer to the calculation of field variables (e.g., velocity and density) having characteristic features of turbulent fluctuations that are obtained at a reduced computational cost in comparison with a formal numerical solution of the full Navier-Stokes equations [9]. The approach used here for generating synthetic turbulence realizations incorporates two models at different scales (Figure 2.1): a submesoscale Garrett-Munk internal wave (GMIW) realization [10, 18] with approximately 10 m horizontal resolution (x- and y- directions) and 1 m vertical resolution (z-direction) (discussed in Section 2.1) and a microscale expansion of the minimal multiscale Lagrangian map (MMLM) approach to include density (MMLM+density) [17, 19] with a uniform 10 cm grid resolution (introduced in Section 2.2 and discussed in detail in Chapter 3). For practical reasons, the results of the MMLM+density are horizontally down sampled and tiled to a larger size (Chapter 5).

Figure 2.2 shows how a synthetic turbulence realization can be built by compiling models of varying scales. The end realization will have a nominal horizontal grid resolution of 1 m with approximately 10 cm vertical resolution and cover a large horizontal domain (300 m x 300 m x 25 m).

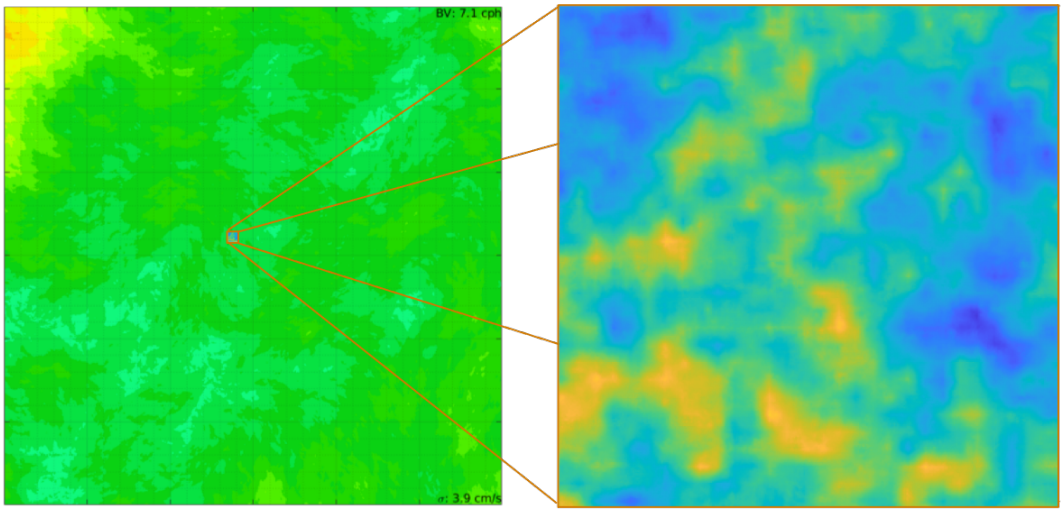

Figure 2.1: Turbulence realization will be initialized from and merged with a larger domain internal wave model. (Left) Superposition of internal waves via Garrett-Munk spectrum (GMIW) with a horizontal domain of 30 x 30 km^2. (Right) Merged field resulting from tiled MMLM+density and GMIW with a horizontal domain of 300 x 300 m^2.

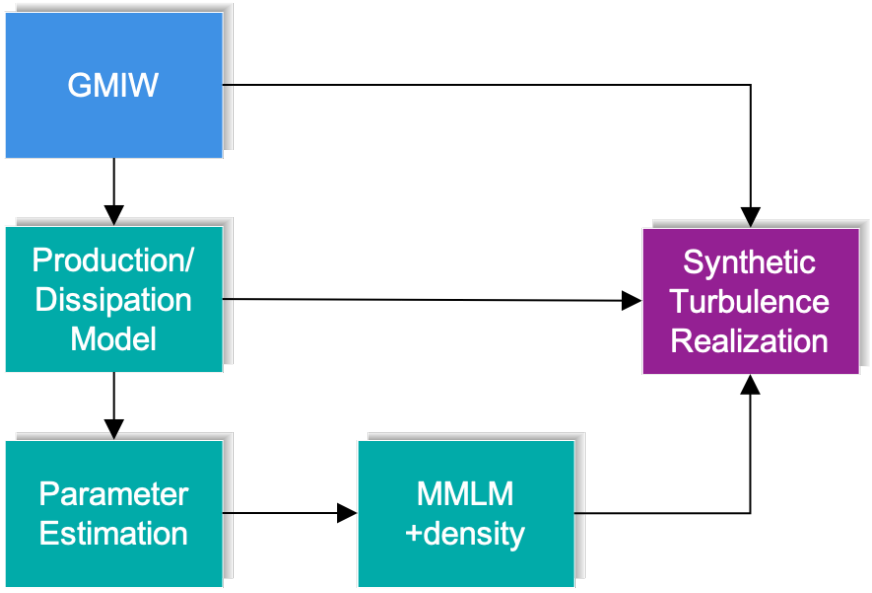

Figure 2.2: Flow of models tp generate the synthetic turbulence realization.

2.1 Garrett-Munk Internal Wave Realization

Ocean internal waves can be generalized into four broad categories: inertial waves, internal tides, internal solitary waves, and broadband stochastic or random internal waves. Stochastic waves are observed everywhere there is stratification; there are no records of an internal calm, even in the Arctic. They are named "stochastic" because they possess little coherence across frequency, wave, and mode number and behave essentially like Gaussian random noise [18].

Garrett and Munk developed an empirical model spectrum for stochastic internal waves using linear wave theory to synthesize observations in the horizontal, vertical, and time coordinates and to characterize the distribution of wave energy across scales [2, 18, 20, 21]. They focused on the frequency continuum and established that these waves dominate motions on horizontal scales smaller than 1 km throughout the thermocline and deep ocean [2]. The Garrett-Munk spectrum is widely used and has been shown to be quite accurate in space and time when applied in locations where boundary effects are not significant [1, 10, 18, 22].

The Garrett-Munk internal wave spectrum provides a 3D representation of the equilibrium internal wave energy field in the deep ocean as a function of frequency and wavenumber, assuming horizontal isotropy. Through the Garrett-Munk internal wave model, submesoscale internal wave structure and oceanic displacements are simply a linear superposition of plane waves with random amplitudes [18].

The Garrett-Munk spectrum can be used to define the distribution of energy by way of a random phase, linear internal wave model, hence referred to as GMIW. The vertical structure is defined by a Brunt-Väisälä (BV) or buoyancy frequency profile and the number of specified modes where the

BV frequency, N, is defined as

$$N = \sqrt{-\frac{g}{\rho_o}\frac{\partial \rho(z)}{\partial z}} \tag{2.1}$$

and where g is the gravitational acceleration, ρ_o is the potential density, and $\rho(z)$ is the water density as a function of depth, z. The Garrett-Munk model has been updated several times [10, 18, 20, 21]. The version used in this work is drawn from the *Garrett and Munk internal wave spectra Matlab toolbox* by Klymak [23].

Figure 2.3 shows cross sections of a horizontal velocity field, u, generated via GMIW. The dotted lines in the figure shows where the planes intersect for reference. The vertical dotted line in the top plot corresponds to the horizontal dotted line in the middle plot. The structure of the larger horizontal velocities can be observed. Similarly, the horizontal dotted line in the top plot corresponds to the horizontal dotted line in the bottom plot. Note that while the top plot is shown with axes to scale, the middle and bottom plots have skewed axes, with the vertical dimension stretched.

Figures 2.4 and 2.5 are analogous to Figure 2.3 with Figure 2.4 showing the vertical velocity and Figure 2.4 showing the density. The vertical velocities are shown to be smaller than the horizontal velocities and as expected, they also have less horizontal coherence. The stretching observed in the middle and bottom plots of Figure 2.4 is due to the skewed axis limits.

The vertical gradient of the density can be observed in Figure 2.5 in the middle and bottom plots. The top plot, showing a horizontal cross section has different color limits and roughly a constant mean value, such that the top effectively shows the density fluctuations resulting from GMIW.

The velocity and density fields from GMIW are used to initialize the microscale turbulent realization, MMLM+density (introduced in Section 2.2, discussed in detail in Chapter 3) through the production and dissipation model and parameter estimation (introduced in Section 2.3, discussed in

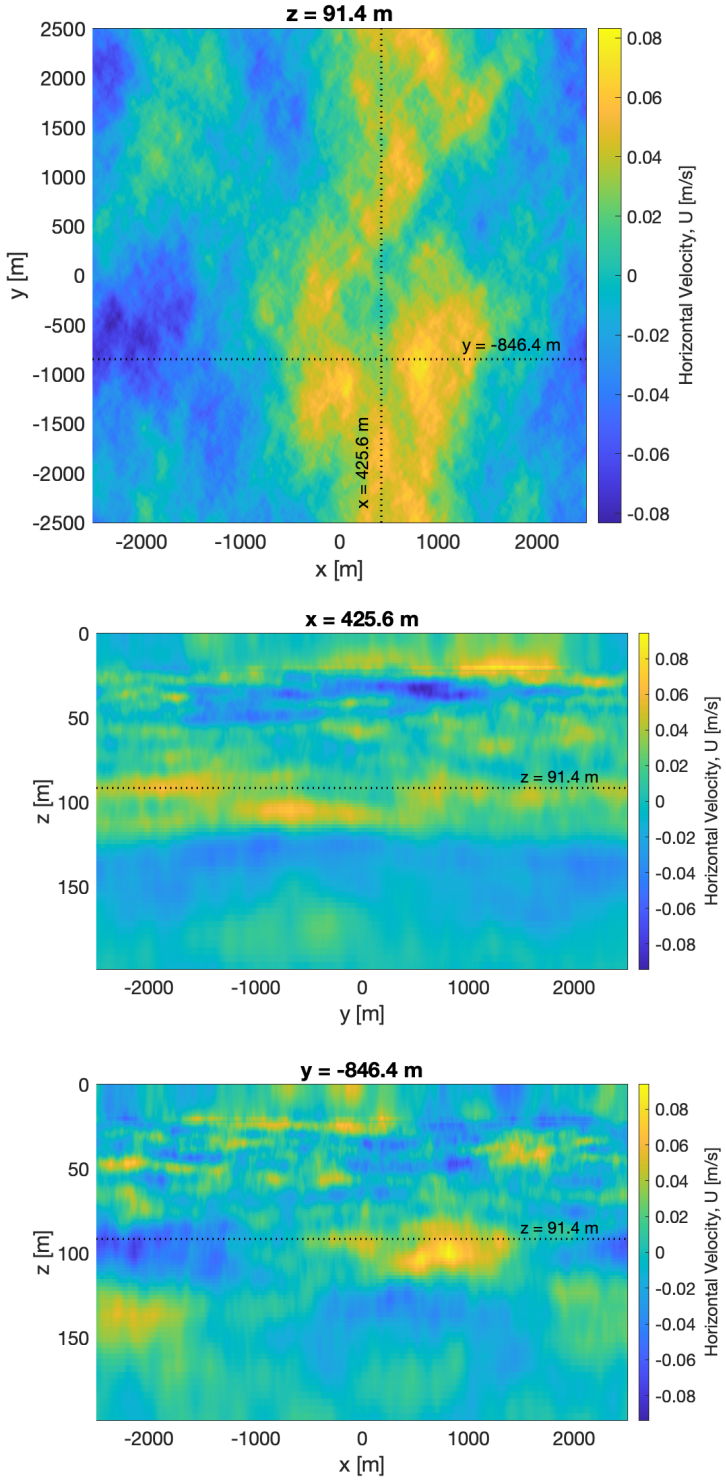

Figure 2.3: Cross sections of the horizontal velocity field, u, generated via GMIW. Dotted lines show where planes intersect. Note axes are not to scale for the middle and bottom plots.

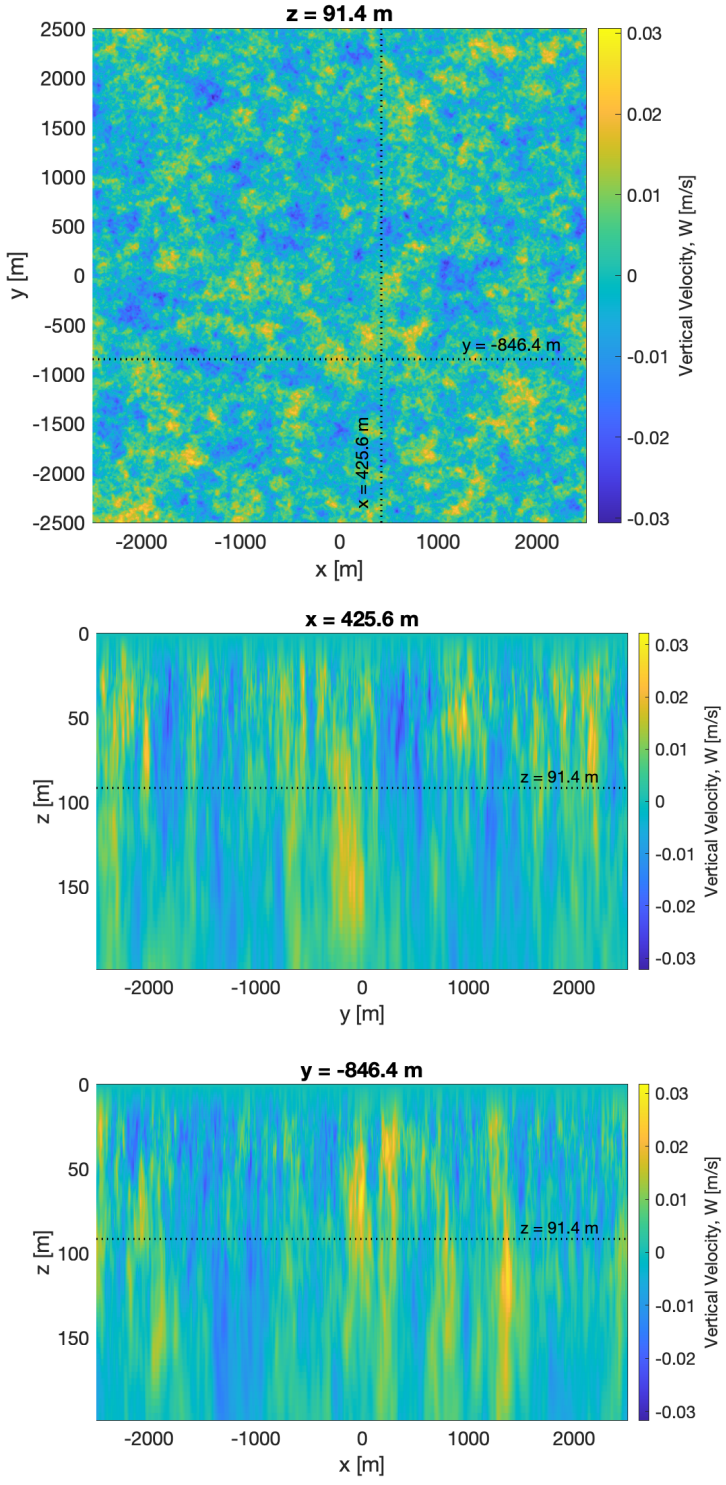

Figure 2.4: Cross sections of the vertical velocity field generated via GMIW. Dotted lines show where planes intersect. Note axes are not to scale for the middle and bottom plots.

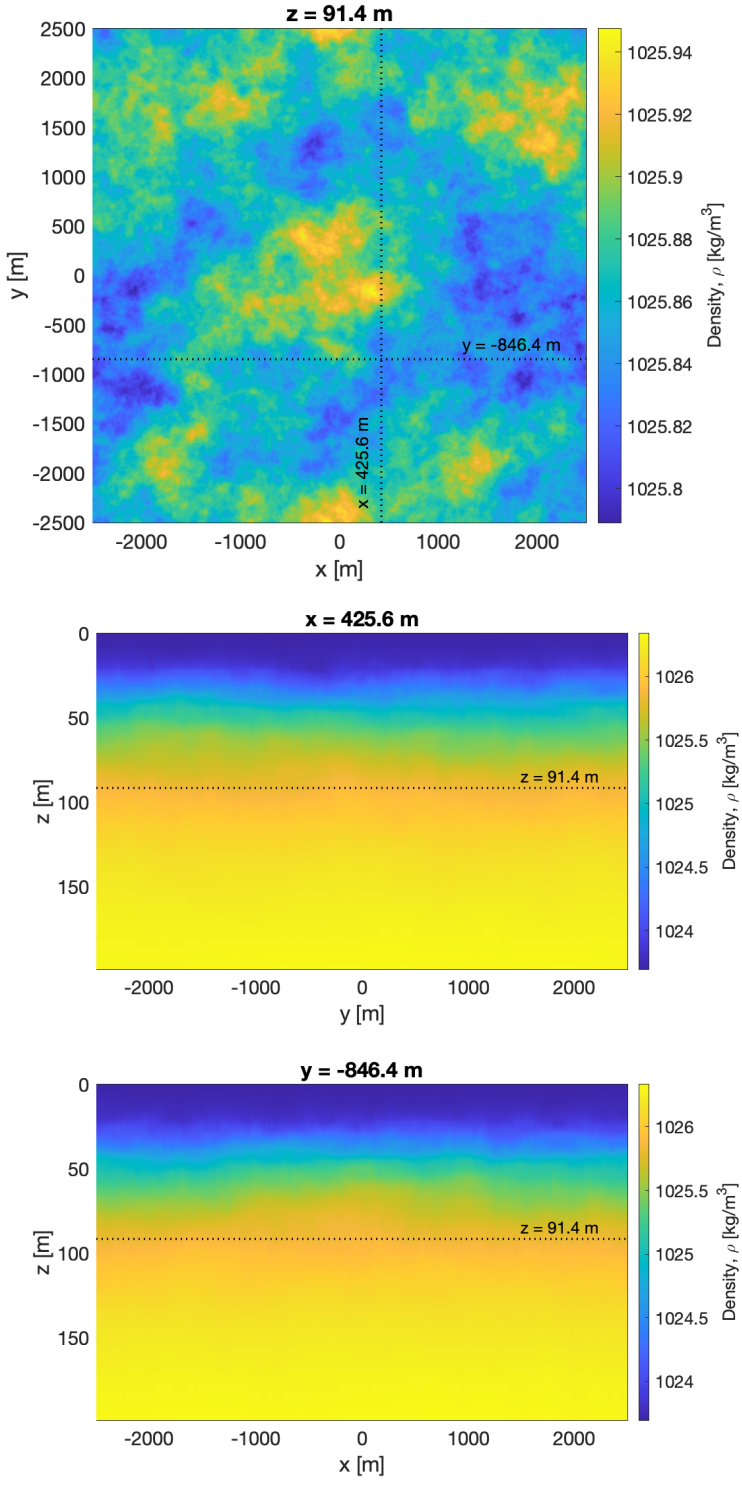

Figure 2.5: Cross sections of the density field generated via GMIW. Dotted lines show where planes intersect. Note axes are not to scale for the middle and bottom plots and the top color bar has different limits.

detail in Chapter 4). This process is outlined in Figure 2.2.

2.2 Minimal Multiscale Lagrangian Map +density (MMLM +density)

The Minimal Multiscale Lagrangian Map (MMLM) approach is a synthetic turbulence realization technique which generates isotropic non-Gaussian intermittent velocity fluctuations in 3D [17]. The simplest representation of homogeneous isotropic turbulence is via superposition of Fourier modes with random phases [17, 24]. The resulting amplitudes of the synthetic velocity field can then be modulated to match a prescribed kinetic energy spectrum. The main limitation of this approach is that the results of this simple realization will lack both turbulent spatial structure and nonlinear energy transfer [9, 17]. The MMLM approach overcomes this limitation by using a Lagrangian mapping technique to introduce intermittency and turbulence structure via a scale-by-scale construction to locally distort the structureless velocity field and mimic the cascading process with cumulative distortive action. These distortions are made via particle advection and grid rectification, then corrected to satisfy incompressibility [17].

The mechanics and statistics of scalar fluctuations have been shown to parallel those of turbulent velocity [25]. Additionally, the development of small scale turbulence is known to be governed by both background shear and buoyancy forces resulting from ambient density stratification [26].

Here, these important mechanisms are reflected by adding a density scalar field into the MMLM algorithm, to develop the MMLM+density approach. This new algorithm generates a scalar density field in parallel with the velocity fluctuation field, initialized as a Gaussian field via Fourier modes with random phases and a prescribed scalar energy spectrum. In this updated algorithm, the field distortion contains an additional term for gravitational forcing.

Figure 2.6 shows sample output from MMLM+density. The top graphic shows the velocity magnitude in meters per second (with zero mean background velocity) and the bottom graphic shows the density fluctuations in kilograms per meter cubed. The MMLM+density algorithm is discussed in detail in Chapter 3.

2.3 Production & Dissipation

While it is possible to model the production and dissipation of turbulence using direct numerical solutions (DNS) of the Navier-Stokes equations, the benefits of reduced computation discussed in Sections 2.1 and 2.2 would be negated. Therefore, the empirical relation between the gradient Richardson number and the kinetic energy dissipation rate [1, 12, 27, 28] is exploited to inject spatial variability that accounts for variable energy production and dissipation in the ocean. Implementation of this approximation is discussed in Chapter 4.

Further exploration of other turbulence models or trade-offs between models were deemed out of scope for this work.

2.4 Functional Flow

The functional flow map of the algorithm used in this work with the user inputs needed is shown in Figure 2.7 (this information is also shown at a high level in Figure 2.2).

The first step is to load the desired GMIW realization (Block 1 of Figure 2.7). The required input are the filename and file path, with the assumption that the GMIW realization has already been generated. Parameters are extracted from the GMIW realization (described in Chapter 4), including the BV frequency and kinetic energy dissipation rate. These parameters are automatically used to inform the MMLM+density tile generation (Block 2).

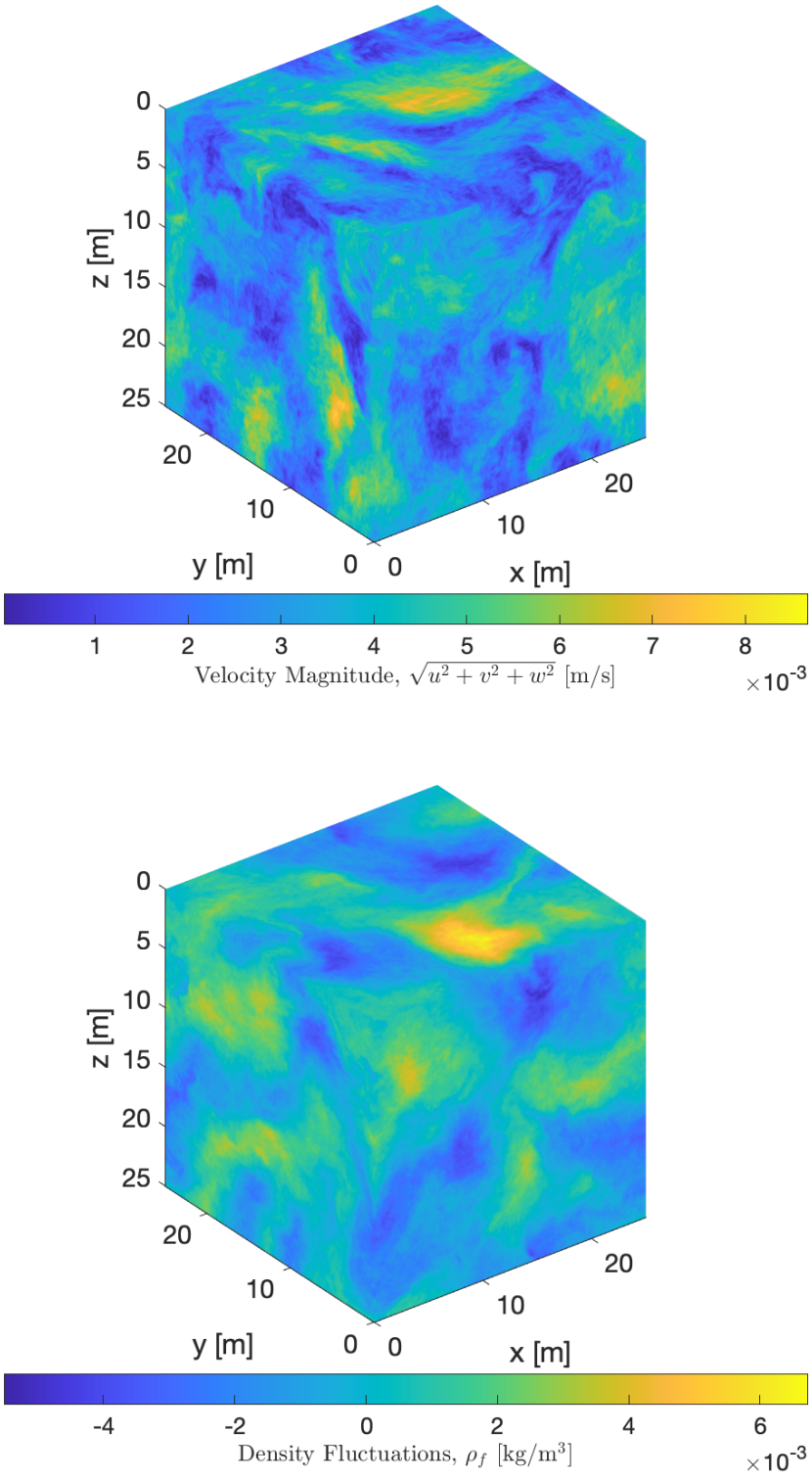

Figure 2.6: Sample results from MMLM+density (top) velocity magnitude in m/s with zero mean background velocity and (bottom) density fluctuations in kg/m^3.

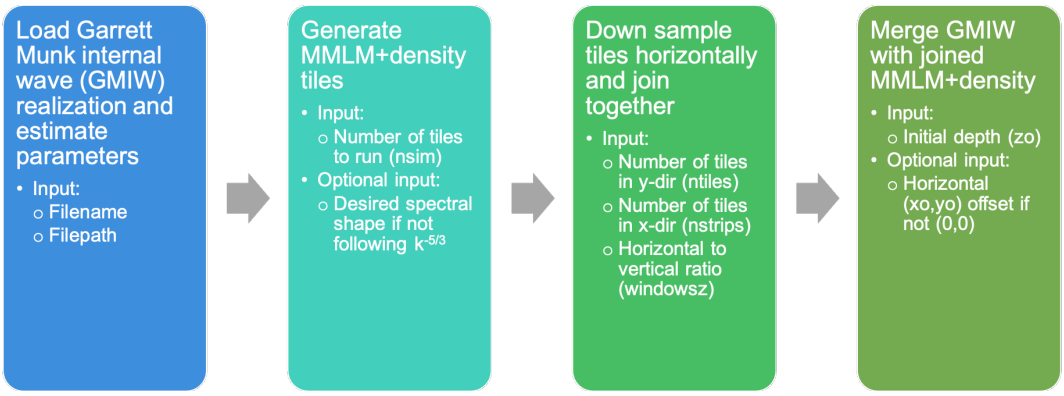

Figure 2.7: Functional flow of the synthetic turbulence realization.

The only user defined input required in Block 2 is the number of unique tiles to simulate. The default energy spectrum will follow the trend of $k^{-5/3}$; if an alternate spectrum is desired (i.e., k^{-1}), that would also need to be specified.

The next step (Figure 2.7, Block 3) down samples the MMLM+density tiles horizontally and merges them together into a larger field. The amount of down sampling and the size of the field, specified by the number of tiles in the x- and y- directions, are user defined variables. This process is described in Chapter 5.

The last step (Figure 2.7, Block 4) uses the GMIW realization loaded in Block 1 and merges it with the output of Block 3. The GMIW realization has a larger domain size than the MMLM+density domain size. For the examples shown, GMIW has a domain of 5000 m x 5000 m x 200 m while MMLM+density has a domain of 25 m x 25 m x 25 m and is tiled to cover 300 m x 300 m x 25 m. In order to align GMIW and the tiled MMLM+density fields, a depth band for the GMIW realization is required, specified by the minimum depth of the band, z_o. Horizontal offsets are optional inputs which may be desirable to use if multiple synthetic turbulence realizations are generated from the same GMIW simulation. If not specified, the horizontal alignment uses the center of the GMIW realization ($x_o = 0, y_o = 0$)

2.5 Data Comparison

Ocean temperature and velocity data from a towed sensor probe chain are used to compare against the synthetic turbulence realization results. The chain has 26 FP07 thermistors which are used to measure the ambient ocean temperature are derive the density, 3 electromagnetic based sensors which are used to measure the ambient ocean velocity fluctuations, and 4 pressure sensors which are used to measure the chain depth and infer the depth of each of the sensors. The BV frequency obtained during data collection is shown to match the input profile used for the GMIW realization and the subsequent MMLM+density realization. Details on the chain data and comparison results can be found in Chapter 7.

Intended to be blank.

Chapter 3

Minimal Multiscale Lagrangian Map +density

3.1 MMLM+density Overview

The MMLM+density approach to generate a synthetic turbulence realization results in the 3 component velocity fluctuation and density fluctuation fields which are shown to be non-Gaussian and intermittent.

The algorithm is initialized by imposing a specified velocity energy spectrum with random phase on a divergence-free velocity field and by imposing a specified correlated density energy spectrum with random phase on a scalar density field with a specified gradient [Brunt-Väisälä (BV) frequency, N] (Equation 2.1).

The Fourier modes are filtered with a spectrally sharp filter into equally spaced wavenumber bands (Figure 3.1). These wavebands correspond to increasingly smaller scales in physical space. At each of these band steps, a Lagrangian map in physical space shifts the computational grid, representing displacement of fluid particles. The shifted grid is interpolated back to a regularly spaced rectangular grid and any introduced divergence is removed (from the velocity field only via Projection space by projecting to a divergence-free set of basis functions). The band passed results are combined back with the full scale data, the energy is rescaled back to the imposed spectrum, and the process is repeated, nesting the coarse scales down to the smallest scales.

Figure 3.2 shows this process and it is described in detail in the subsequent text.

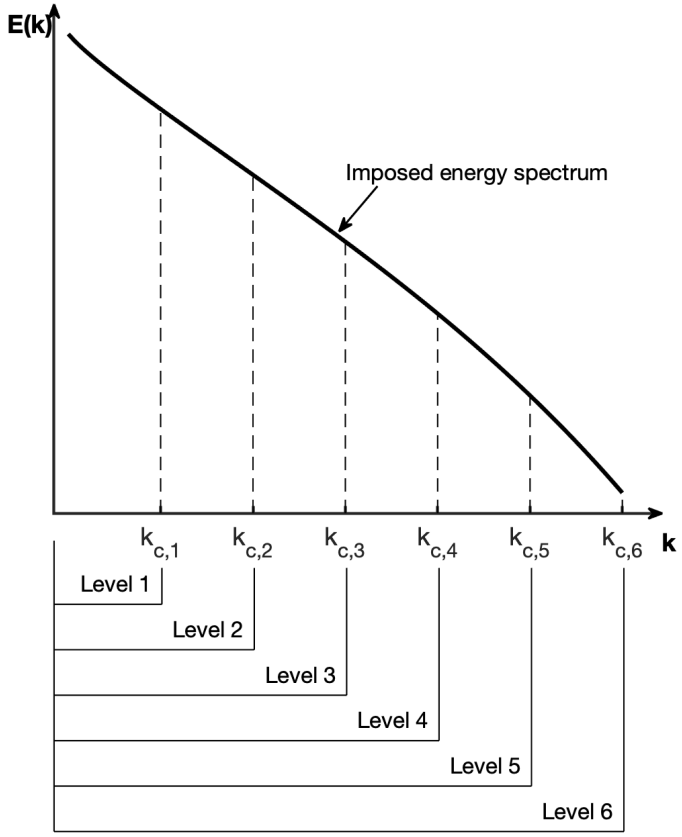

Figure 3.1: MMLM+density bands.

3.1.1 Initialization

MMLM+density is initialized by generating isotropic synthetic velocity and density fluctuations, as outlined in the top half of Figure 3.2. Density is modeled in MMLM+density as a function of position consisting of 3 elements: the reference density, ρ_o, the relative background density derived from the input BV frequency (discussed in Chapter 4), $\rho_z(\mathbf{x})$, and the density fluctuations, $\rho_f(\mathbf{x})$.

$$\rho(\mathbf{x}) = \rho_f(\mathbf{x}) + \rho_z(\mathbf{x}) + \rho_o \tag{3.1}$$

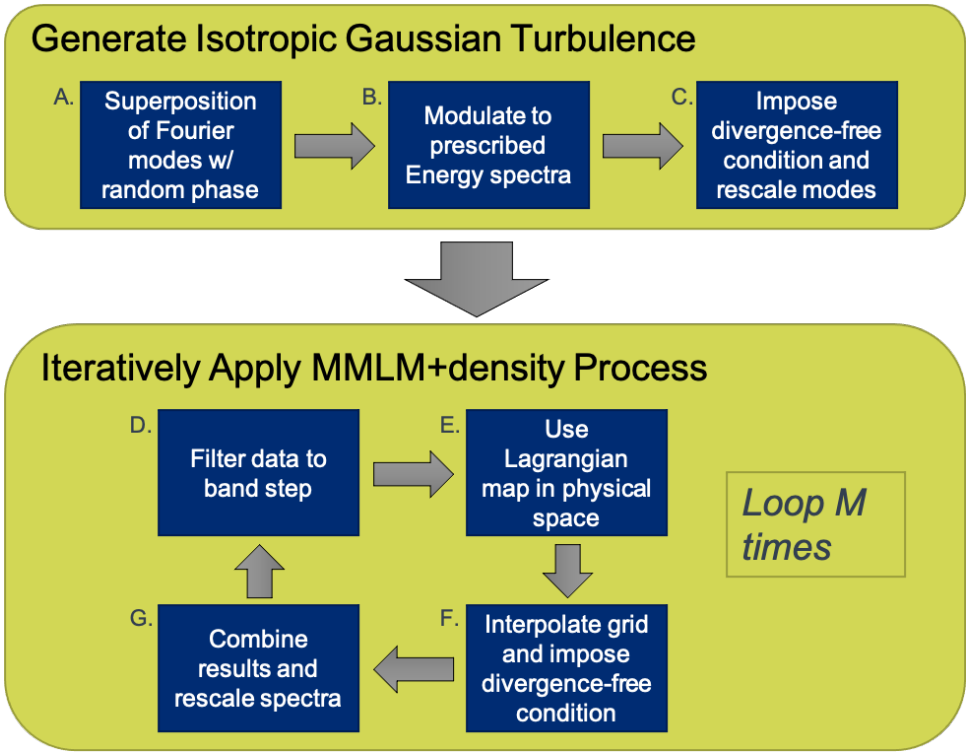

Figure 3.2: MMLM+density steps.

The velocity is broken down similarly to be a function of the velocity fluctuations $\mathbf{u}_f(\mathbf{x})$ and the mean background velocity, $\mathbf{u}_o(\mathbf{x})$

$$\mathbf{u}(\mathbf{x}) = \mathbf{u}_f(\mathbf{x}) + \mathbf{u}_o(\mathbf{x}) \tag{3.2}$$

The mean background velocity, $\mathbf{u}_o(\mathbf{x})$, is assumed to be zero for the purposes of generating the MMLM+density vector field and only the velocity fluctuations are considered. This simplifies the expression in Equation 3.2 to

$$\mathbf{u}(\mathbf{x}) = \mathbf{u}_f(\mathbf{x}) \tag{3.3}$$

The first step of MMLM+density is the superposition of Fourier modes with random phases, done for both the velocity fluctuation and density fluctuation fields (Figure 3.2, Block A). This is implemented by initializing a random field with a zero mean Gaussian distribution.

$$\mathbf{u}(x,y,z) \sim \mathcal{N}\left(\mu = 0, \sigma^2 = 1\right) \tag{3.4}$$

where **u** has three components (u, v, w). This initialization is repeated for the density fluctuation field. The initialized random Gaussian velocity field is shown in Figure 3.3. The Fourier modes of each field are computed by taking the fast Fourier transform (fft).

$$\mathbf{U}(k_x, k_y, k_z) = \mathbf{U}(\mathbf{k}) = \mathcal{F}\{\mathbf{u}(\mathbf{x})\} = \sum_{p=0}^{N-1} e^{-\frac{2\pi p k_x}{N}} \sum_{q=0}^{N-1} e^{-\frac{2\pi q k_y}{N}} \sum_{r=0}^{N-1} e^{-\frac{2\pi r k_z}{N}} u_{pqr} \tag{3.5}$$

where there are N points in each dimension of the synthetic realization. The density Fourier modes are similarly defined.

$$\mathcal{P}(\mathbf{k}) = \mathcal{F}\{\rho_f(\mathbf{x})\} \tag{3.6}$$

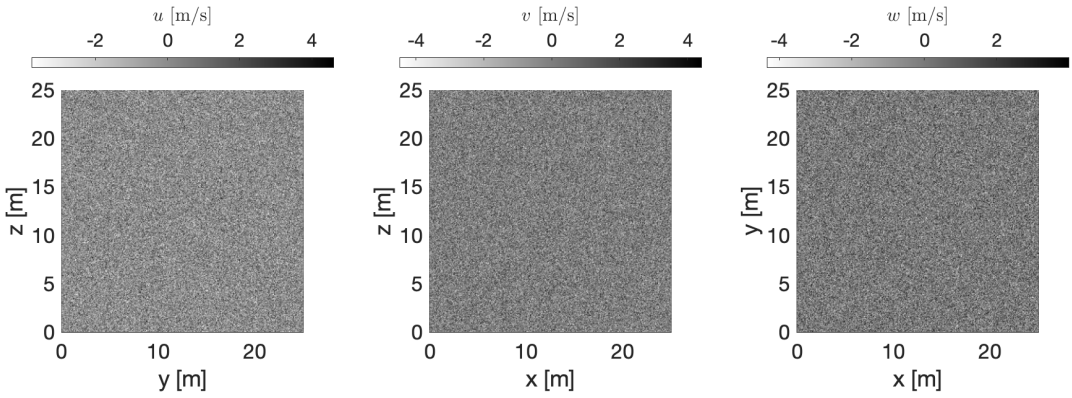

Figure 3.3: Initialized random zero mean Gaussian velocity field shown in m/s.

Next, the Fourier modes are modulated to match a prescribed kinetic energy spectrum (Figure 3.2, Block B). The velocity-spectrum tensor is defined as

$$\Phi_{ij}(\mathbf{k}) = \frac{E(k)}{4\pi k^2} P_{ij}(\mathbf{k}) = \frac{E(k)}{4\pi k^2} \left(\delta_{ij} - \frac{k_i k_j}{k^2}\right) \tag{3.7}$$

where $E(k)$ is the prescribed 3D radial energy spectrum and P_{ij} is the projection tensor [24]. From here, the kinetic energy of the Fourier modes can be defined by

$$E_{ii}(\mathbf{k}) = \langle U_i(\mathbf{k}), U_i(\mathbf{k}) \rangle = \iiint_{-\infty}^{\infty} \frac{1}{2} \Phi_{ii}(\mathbf{k}) \mathrm{d}\mathbf{k} = \Phi_{ii}(\mathbf{k}) * \left(\frac{2\pi N}{\mathrm{d}x}\right)^3 \tag{3.8}$$

where $\mathrm{d}x$ is the grid spacing of the synthetic realization. The energy spectrum

is imposed by multiplying the initialized random zero mean Gaussian field by the square root of the kinetic energy.

$$\mathbf{U}(\mathbf{k}) = \mathbf{U}(\mathbf{k})\sqrt{E_{ii}(\mathbf{k})} \tag{3.9}$$

For density, the projection tensor is dropped, which leads to

$$\mathcal{P}(\mathbf{k}) = \mathcal{P}(\mathbf{k})\sqrt{\frac{E_\rho(k)}{4\pi k^2}\left(\frac{2\pi N}{\mathrm{d}x}\right)^3}. \tag{3.10}$$

The model spectrum for velocity is

$$E(k) = C\epsilon^{2/3}k^{-5/3}f_\eta f_{\text{damp}} \tag{3.11}$$

where the dissipation shape function is defined as

$$f_\eta(k\eta) = e^{-\alpha_4 k\eta} \tag{3.12}$$

and the spectral dampening function is defined as

$$f_{\text{damp}}(k) = e^{-\left(\frac{k}{k_{\max}}\right)^4}. \tag{3.13}$$

This analysis omits the shape function for the energy containing range, which is given by

$$f_L(kL) = \left(\frac{kL}{[(kL)^{\alpha_2} + \alpha_1]^{1/\alpha_2}}\right)^{5/3+\alpha_3}, \tag{3.14}$$

since the GMIW realization will fill in this side of the spectrum. The density spectrum is defined as

$$E_\rho(k) = C_{oc}\epsilon^{-1/3}k^{-5/3}\chi f_\eta f_{\text{damp}} \tag{3.15}$$

where χ is the dissipation rate of density fluctuations. The constants used in Equations 3.11-3.15 are provided in Table 3.1 and $\nu = 1 \times 10^{-6}$ m^2/s is the kinematic viscosity of water. Figure 3.4 shows sample 3D energy spectra for both velocity and density.

The last initialization step is to impose the divergence-free condition on

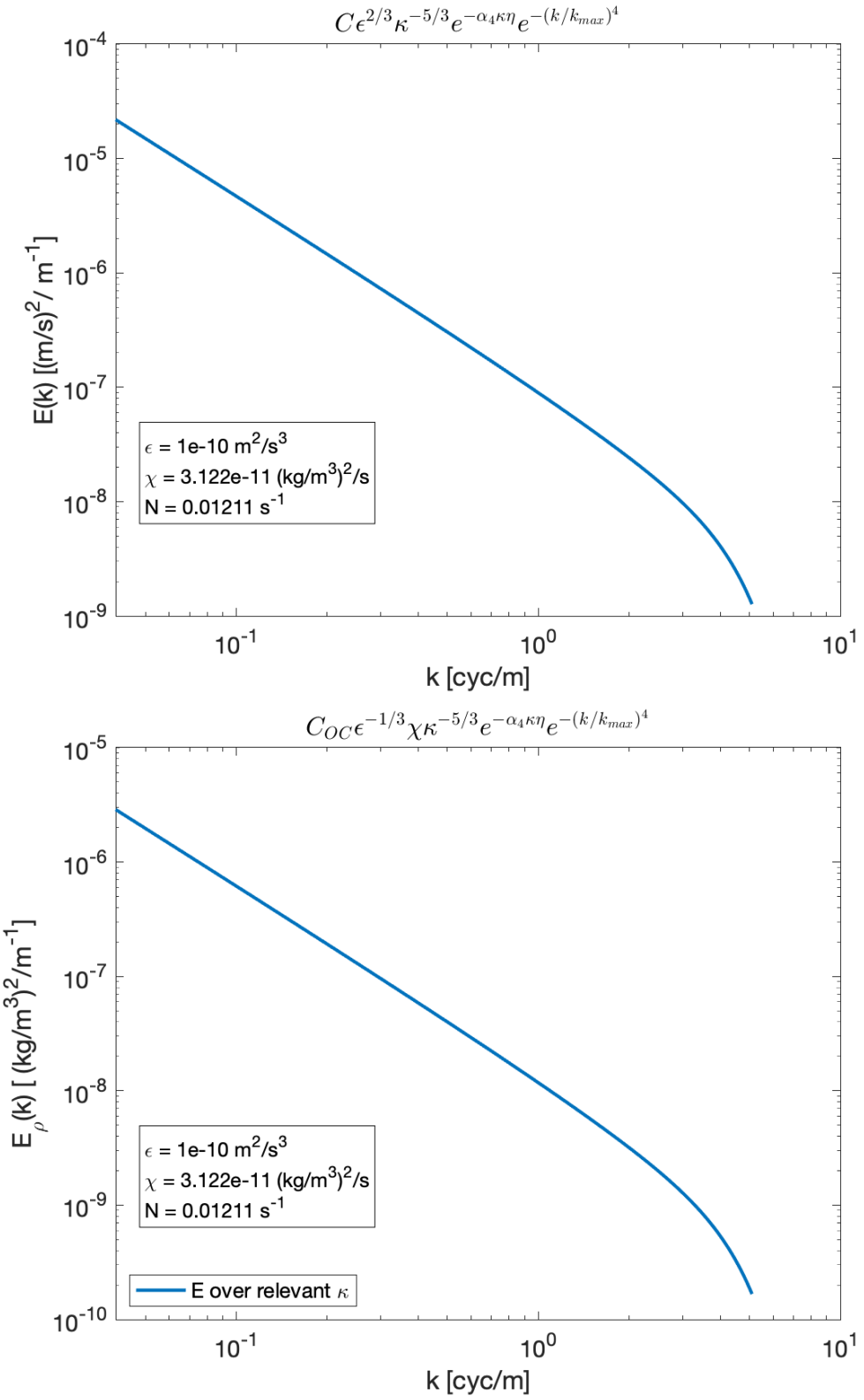

Figure 3.4: Velocity energy spectra (top) and density energy spectra (bottom)

Table 3.1: Energy spectra constants.

constant	value
C	1.613
C_{oc}	0.68
α_1	0.39
α_2	1.2
α_3	4.0
α_4	2.1

the velocity field by projecting to a divergence-free set of basis functions (Figure 3.2, Block C). This is only required for the velocity field as imposing a divergence-free condition is not applicable to a scalar field.

$$U_i(k) = P_{ij}(k)U_j(k) \tag{3.16}$$

The imposed energy spectrum is recovered by rescaling the Fourier modes for both the velocity and density fields

$$\mathbf{U}(\mathbf{k}) = \mathbf{U}(\mathbf{k})\sqrt{\frac{E(k)}{\sum_{|q|=k}\mathbf{U}(q)\cdot\mathbf{U}^*(q)}}. \tag{3.17}$$

Figure 3.5 shows the velocity fluctuation field along three orthogonal planes for each velocity component (u,v,w) after initialization is complete.

Figure 3.6 shows the starting density for two example cases where the top plot shows the starting density for the parameters derived from the GMIW realization (discussed in Chapter 4). The plot shows the relative background density derived from the input BV frequency, ρ_z, in a bold black line and the plot can be used to visualize the relative size of the fluctuations with respect to the relative background density. Note that ρ_z is purely a function of depth. The next line in the plot (red) shows a vertical slice through the initial density field $\rho_f + \rho_z$ such that the density fluctuations are observed as deviations from the black line. The next 6 lines show cuts through x- and y- for each of 3 depths, denoted on the plot by the dotted line and annotation. These lines intersect the vertical slices at the expected location. The bottom plot

of Figure 3.6 shows slightly different conditions, namely a lower mean BV frequency, N, and a higher kinetic energy dissipation rate, ϵ, resulting in a higher dissipation rate of density fluctuations, χ.

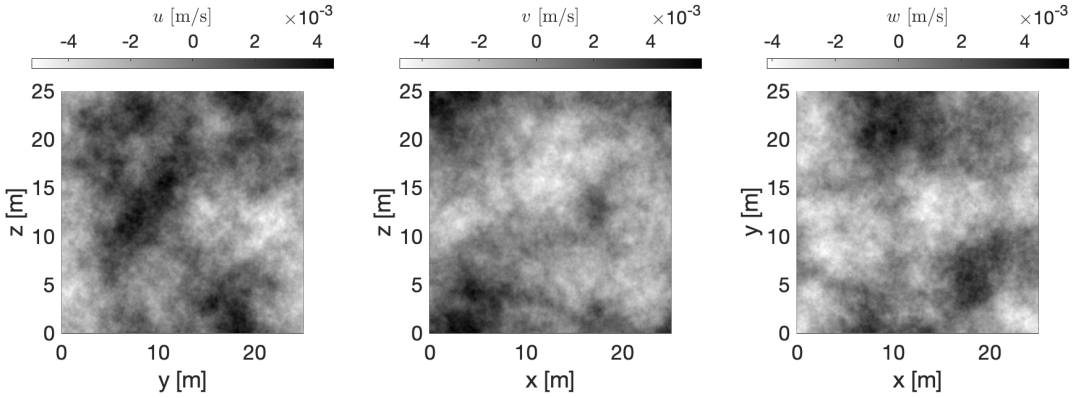

Figure 3.5: Initialized Gaussian velocity field after imposing the prescribed energy spectrum, shown in m/s.

3.1.2 Iteratively Apply MMLM+density Process

The key to the MMLM+density approach is the iterative process of filtering the velocity and density fields at multiple scales of increasing resolution. The Lagranian mapping is then done at each of these scales, with the results of the previous step affecting the next. In this way, the effective shrinking of the grid mimics the energy cascade and inherent multiscale properties of turbulence.

The number of points along each direction of the realization is N with length L along each side, such that the native resolution of the realization is $\mathrm{d}x = L/N$. The total number of band filters, or levels in the realization is M, with the given level n reducing the number of points by a factor of m such that

$$m = 2^{M-n} \tag{3.18}$$

and the resolution is reduced by octaves. The maximum wavenumber at

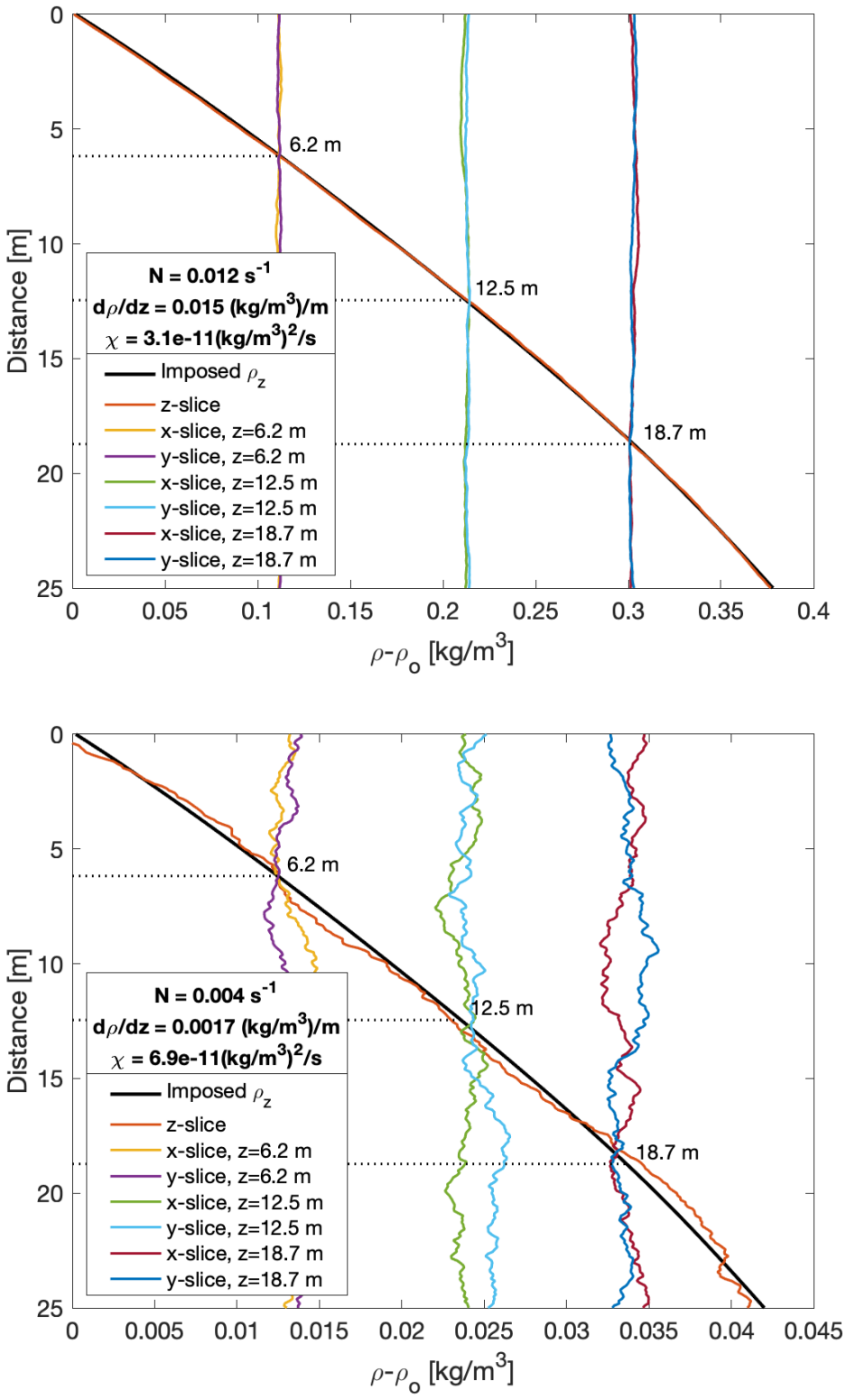

Figure 3.6: Density slices after initialization with (top) a low kinetic energy dissipation rate and (bottom) a high kinetic energy dissipation rate.

each octave is given by

$$k_{c,n} = \frac{k_{\max}}{m} = \frac{\pi N}{Lm} = \frac{\pi}{\mathrm{d}x_n\, m} \tag{3.19}$$

Table 3.2 summarizes these values for $N = 256$ points, $L = 25$ m, and $M = 6$. The level $n = 0$ is the resolution at initialization.

Table 3.2: Levels example for $N = 256$ points, $L = 25$ m, and $M = 6$.

Level, n	**Nodes Reduced, m**	**Points per Level, $\mathbf{N_n}$**	**$\mathbf{dx_n = L/N_n}$**	**$\mathbf{k_{c,n}}$**
0	-	256	0.098 m	32 rad/m
1	32	8	3.1 m	1.0 rad/m
2	16	16	1.6 m	2.0 rad/m
3	8	32	0.78 m	4.0 rad/m
4	4	64	0.39 m	8.0 rad/m
5	2	128	0.20 m	16 rad/m
6	1	256	0.098 m	32 rad/m

The first step in the iterative process for a given level n is to filter the data from the previous level $(n-1)$ in wavenumber space (Figure 3.2, Block D).

$$\mathbf{U}_n(\mathbf{k}) = \mathbf{U}_{n-1}(\mathbf{k}) G_n(\mathbf{k}) \tag{3.20}$$

where the subscript denotes the level and G_n is the transfer function for the spectrally sharp filter used to separate scales.

$$G_n(\mathbf{k}) = \begin{cases} 1; & |\mathbf{k}| \leq k_{c,n} \\ 0; & |\mathbf{k}| > k_{c,n}. \end{cases} \tag{3.21}$$

Figure 3.7 shows a sample filtered velocity field from level $n = 1$. The resolution is much coarser than the initialized velocity field, shown in Figure 3.5 and the velocity magnitudes are notedly different since the fields have not yet been renormalized.

The Lagrangian map is applied in physical space to shift the grid, representing displacement of fluid particles (Figure 3.2, Block E).

$$\mathbf{u}_n(\mathbf{x}_n) = \mathcal{F}^{-1}\{\mathbf{U}_n(\mathbf{k})\} \tag{3.22}$$

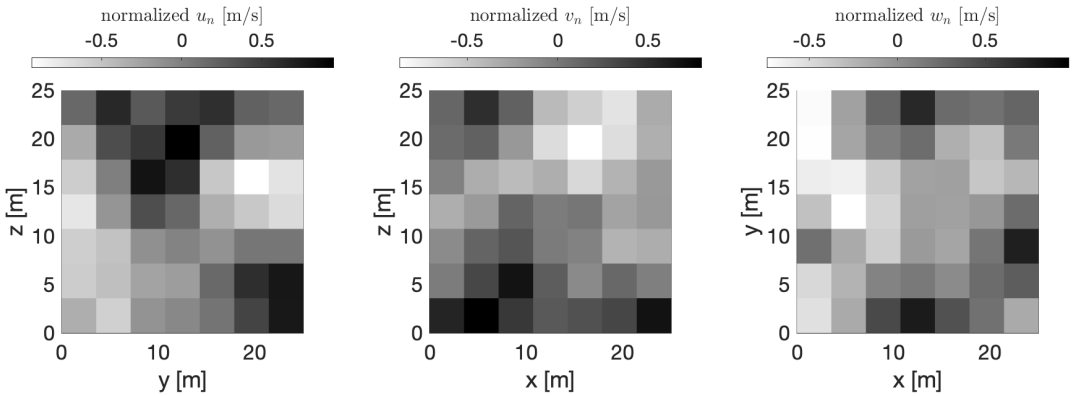

Figure 3.7: Level $n = 1$ filtered velocity field in m/s. The resolution is much coarser than the initialized velocity field and the velocity magnitudes are notedly different since the fields have not yet been renormalized.

The Lagrangian maps from each point in the grid $\mathbf{x}_n \mapsto \mathbf{r}_n$.

$$\mathbf{r}_n = \mathbf{x}_n + t_n \mathbf{u}_n - \frac{t_n^2}{2}\frac{\rho_n}{\rho_o}\mathbf{g} \tag{3.23}$$

The time step, t_n, is a parameter derived from the root mean square (rms) velocity such that the rms displacement is set approximately to one grid step size at resolution n

$$t_n = \frac{\mathrm{d}x_n}{u_{\mathrm{rms},n}} \tag{3.24}$$

where

$$u_{\mathrm{rms},n} = \left\langle \frac{m}{N} \sum_p \mathbf{u}_{n,p}^2 \right\rangle^{1/2} \tag{3.25}$$

and the velocity remains unchanged but is placed at the new displaced position $\mathbf{r}_n$, $\mathbf{u}_n(\mathbf{x}_n) \mapsto \mathbf{u}_n(\mathbf{r}_n)$. The density field is also mapped the same way. Figure 3.8 shows the velocity field from level $n = 1$ after the Lagrangian mapping. Areas with large velocities show more deformation while smaller velocities show less deformation.

The shifted irregular grid is interpolated back onto the rectangular grid (Figure 3.2, Block F).

$$\mathbf{u}_n(\mathbf{r}_n) \mapsto \mathbf{v}_n(\mathbf{x}_n) \tag{3.26}$$

This is accomplished using Delaunay triangulation with MATLAB's

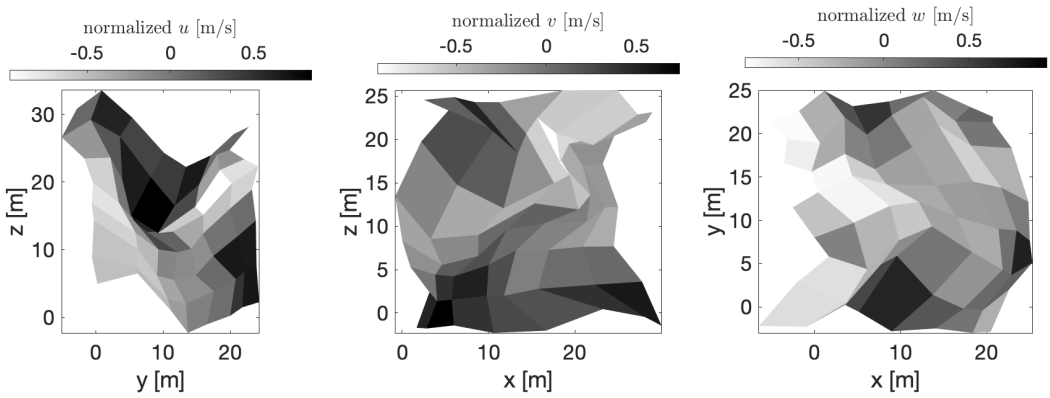

Figure 3.8: Level $n = 1$ velocity field after Lagrangian mapping in m/s.

`scatteredInterpolant`[1] function. The density field is also mapped according to the same process.

The new velocity, $\mathbf{v}_n(\mathbf{x}_n)$, is transformed back to Fourier space

$$\mathbf{V}_n(\mathbf{k}_n) = \mathcal{F}\{\mathbf{v}_n(\mathbf{x}_n)\} \tag{3.27}$$

and since the new field may not be solenoidal anymore, it is projected onto its divergence-free part by

$$V_i(k) = P_{ij}(k)V_j(k). \tag{3.28}$$

Figure 3.9 shows the velocity field from level $n = 1$ after the interpolation. This field can be compared with Figure 3.7 to see how the field has changed.

The interpolated fields are combined back with the full scale data (Figure 3.2, Block G) using the expression

$$\mathbf{U}(\mathbf{k}) = \mathbf{V}_n(\mathbf{k}_n) + (1 - G_n)\mathbf{U}(\mathbf{k}) \tag{3.29}$$

where $(1 - G_n)\mathbf{U}(\mathbf{k})$ represents the part of the field that was previously filtered at the start of the iteration and has as such remained unaltered at this level. The last step for the iteration level is to rescale the energy back to the

[1] A benefit of this interpolation method is that the values of the resulting interpolation object only needs to be created once per level. The interpolation object is easily updated for each subsequent velocity component and the density without needing to regenerate the triangulation.

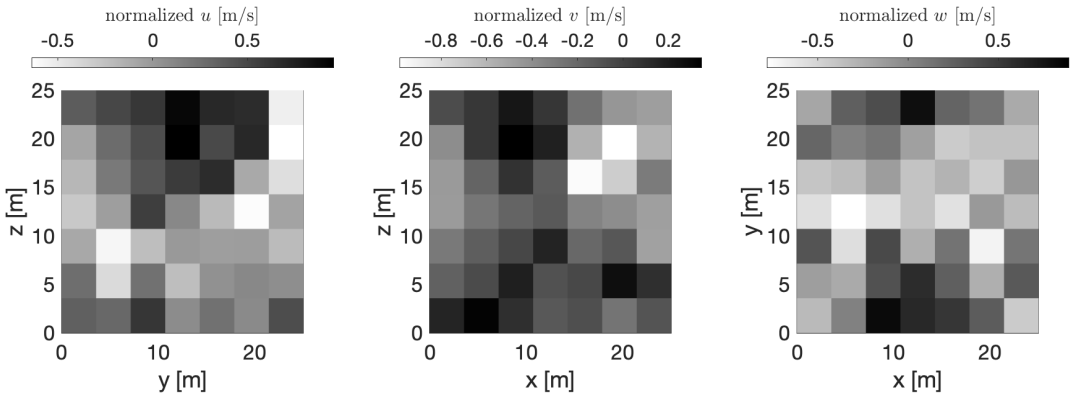

Figure 3.9: Level $n = 1$ velocity field after being interpolated back to a rectangular grid in m/s.

imposed spectra.

$$\mathbf{U}(\mathbf{k}) = \mathbf{U}(\mathbf{k})\sqrt{\frac{E(k)}{\sum_{|q|=k}\mathbf{U}(q)\cdot\mathbf{U}^*(q)}} \tag{3.30}$$

This is required because the energy spectrum is modified by the Lagrangian mapping. This step is also done for the density. Figure 3.10 (bottom) shows the full velocity field after one iteration through the MMLM+density process. The top graphic of the figure denotes which level the velocity field was produced from. Figures 3.11-3.15 continue to walk through the subsequent levels until $n = M = 6$. The top anchoring graphic of each figure also serves as a reminder for how the level is inclusive of previous bands while the bottom graphic shows how increased structure and complexity is introduced through this method.

3.1.3 Isotropy Assumption

The original MMLM approach generated isotropic turbulence. This assumption is reflected in a number of different steps in the algorithm, ranging from the calculation of the velocity-spectrum tensor Φ_{ij}

$$E(k) = \oint \frac{1}{2}\Phi_{ii}(\mathbf{k})\mathrm{d}\mathcal{S}(k) \tag{3.31}$$

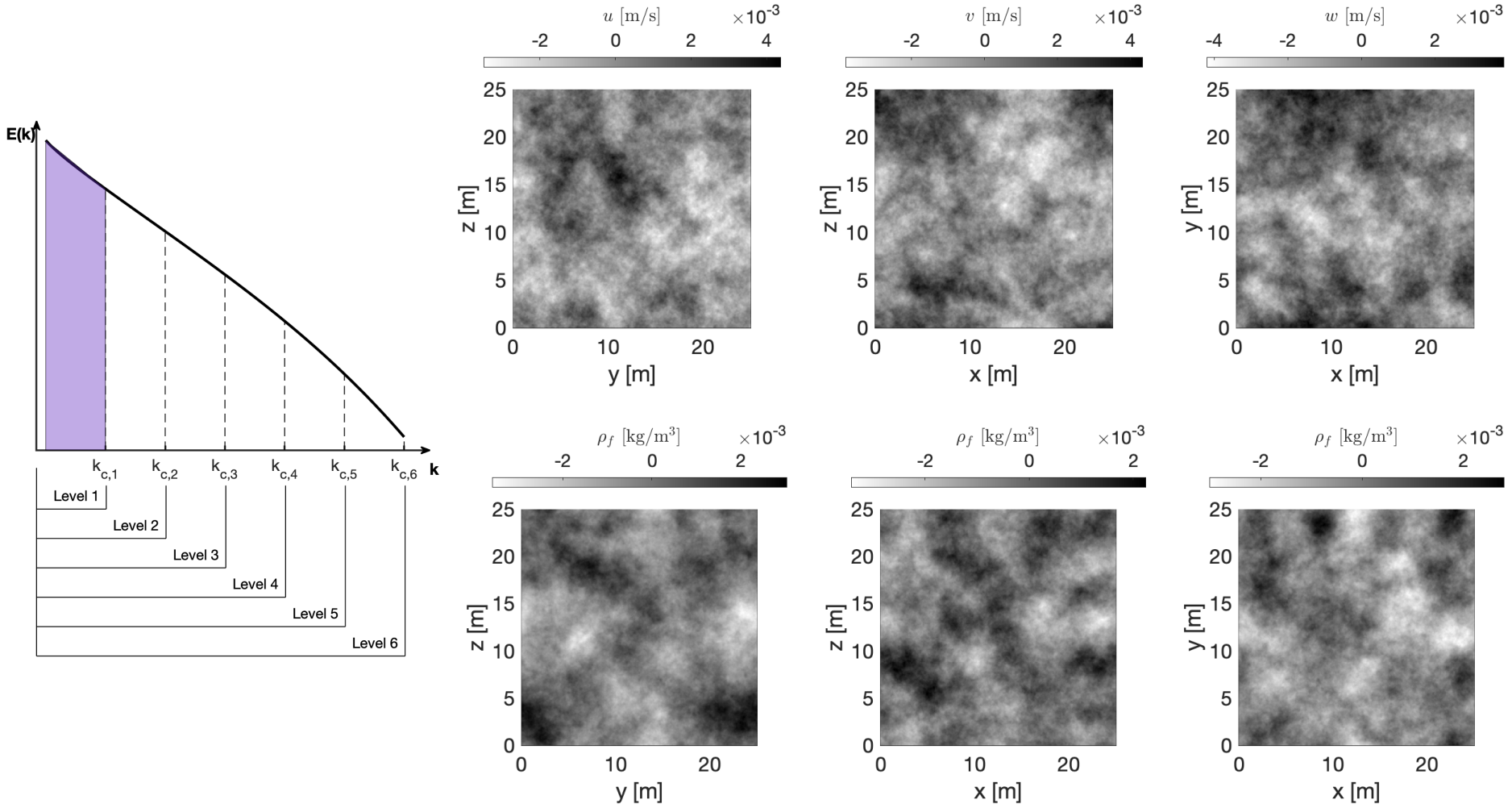

Figure 3.10: (Left) Schematic of the spectrum and different levels used for MMLM+density construction. Only $n = 1$ has been mapped, while the smaller scales (higher levels) are still Gaussian. Contour plot of resulting (right, top row) velocity and (right, bottom row) density fluctuations on 3 orthogonal planes.

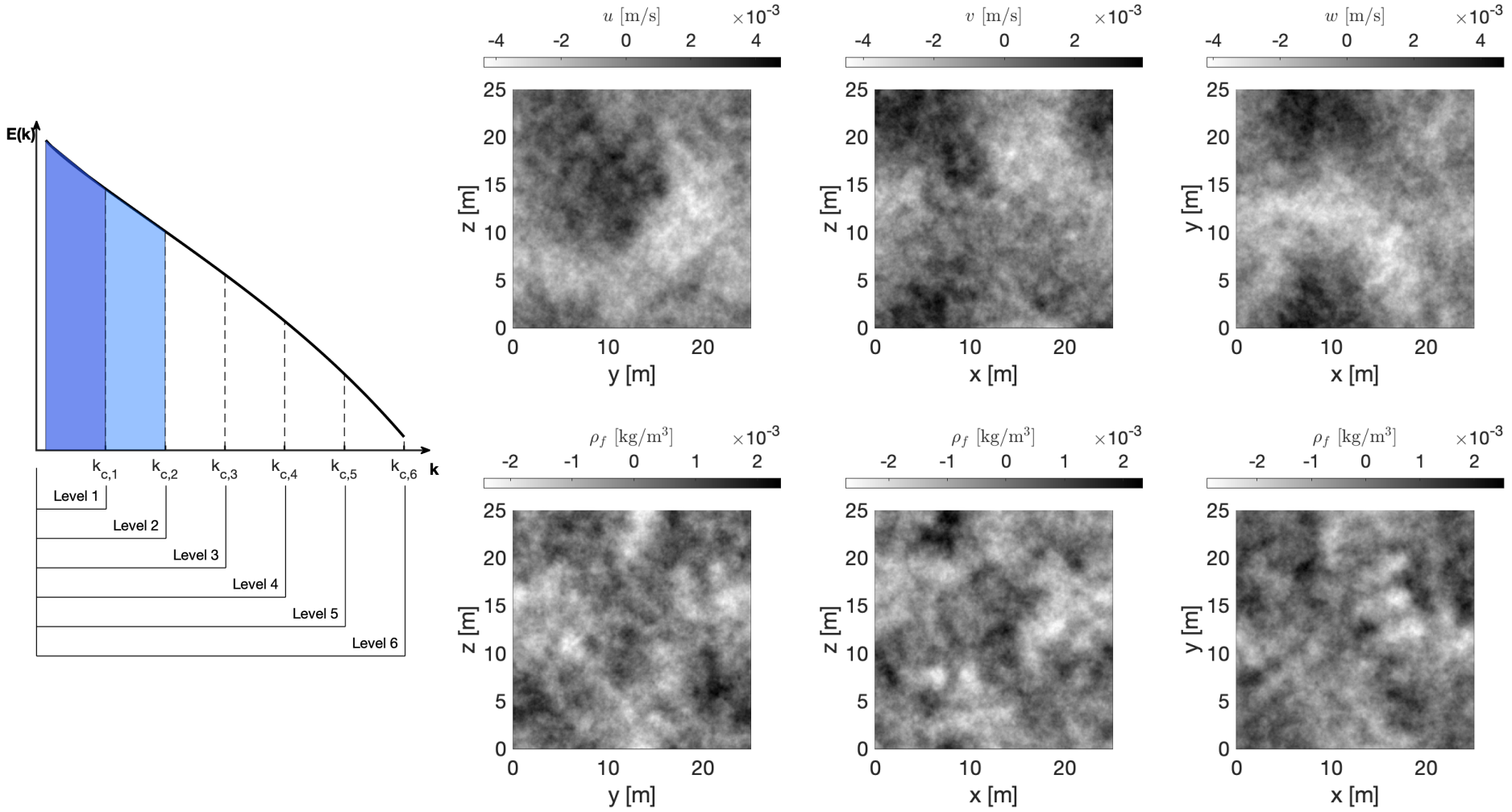

Figure 3.11: (Left) Schematic of the spectrum and different levels used for MMLM+density construction. Here $n = 1 - 2$ has been mapped, while the smaller scales (higher levels) are still Gaussian. Contour plot of resulting (right, top row) velocity and (right, bottom row) density fluctuations on 3 orthogonal planes.

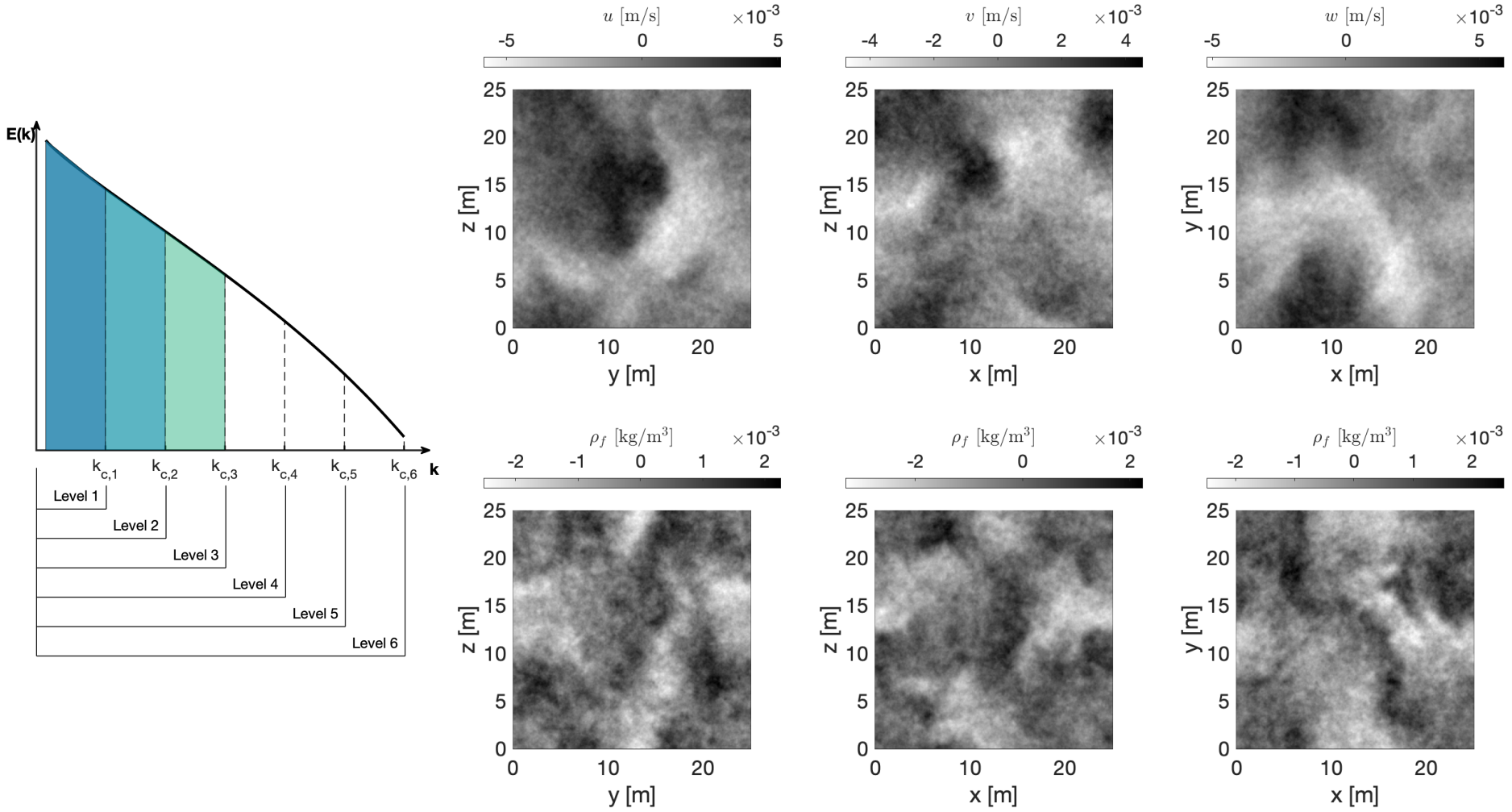

Figure 3.12: (Left) Schematic of the spectrum and different levels used for MMLM+density construction. Here $n = 1 - 3$ has been mapped, while the smaller scales (higher levels) are still Gaussian. Contour plot of resulting (right, top row) velocity and (right, bottom row) density fluctuations on 3 orthogonal planes.

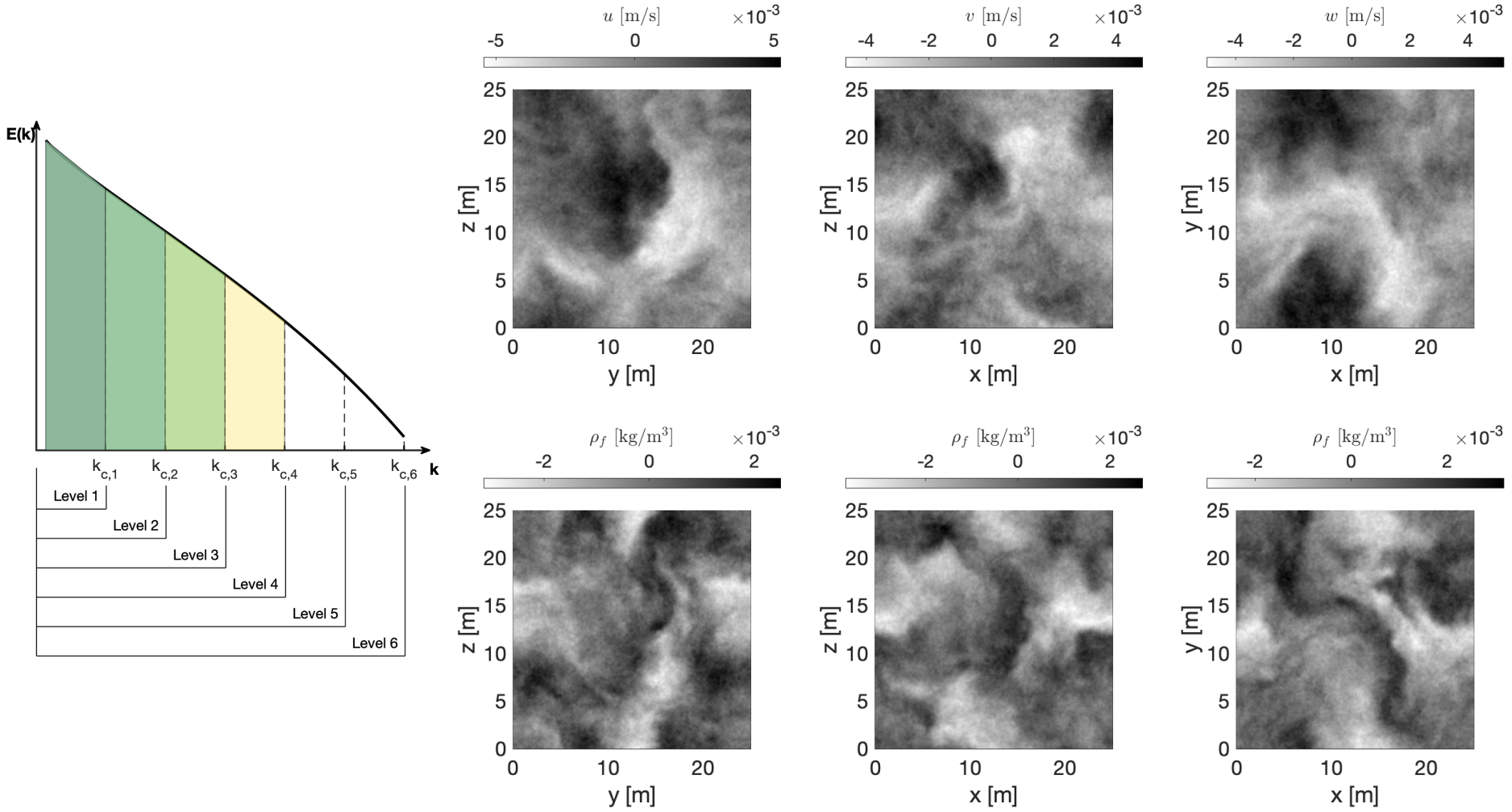

Figure 3.13: (Left) Schematic of the spectrum and different levels used for MMLM+density construction. Here $n = 1 - 4$ has been mapped, while the smaller scales (higher levels) are still Gaussian. Contour plot of resulting (right, top row) velocity and (right, bottom row) density fluctuations on 3 orthogonal planes.

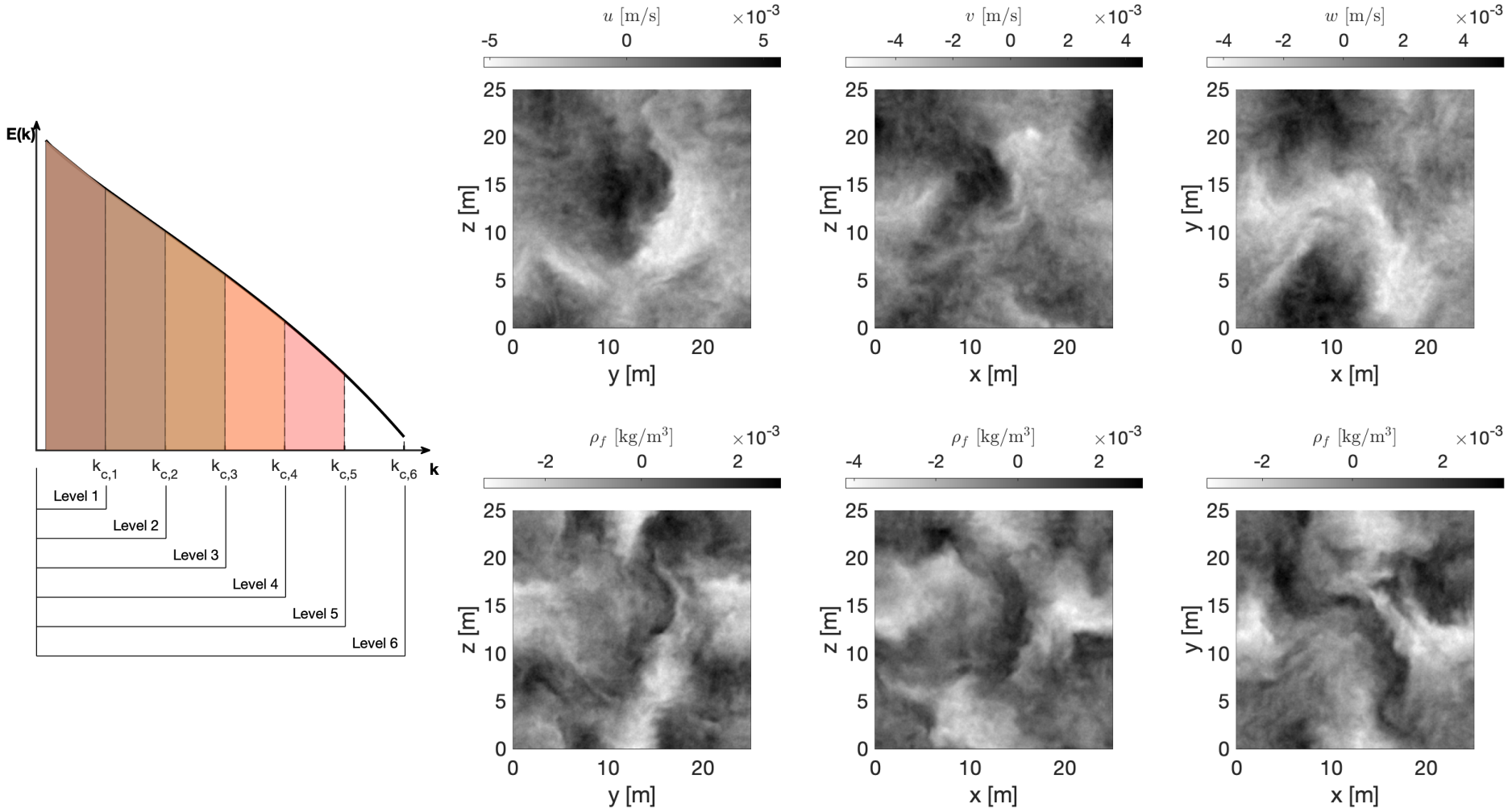

Figure 3.14: (Left) Schematic of the spectrum and different levels used for MMLM+density construction. Here $n = 1 - 5$ has been mapped, while the smaller scales (higher levels) are still Gaussian. Contour plot of resulting (right, top row) velocity and (right, bottom row) density fluctuations on 3 orthogonal planes.

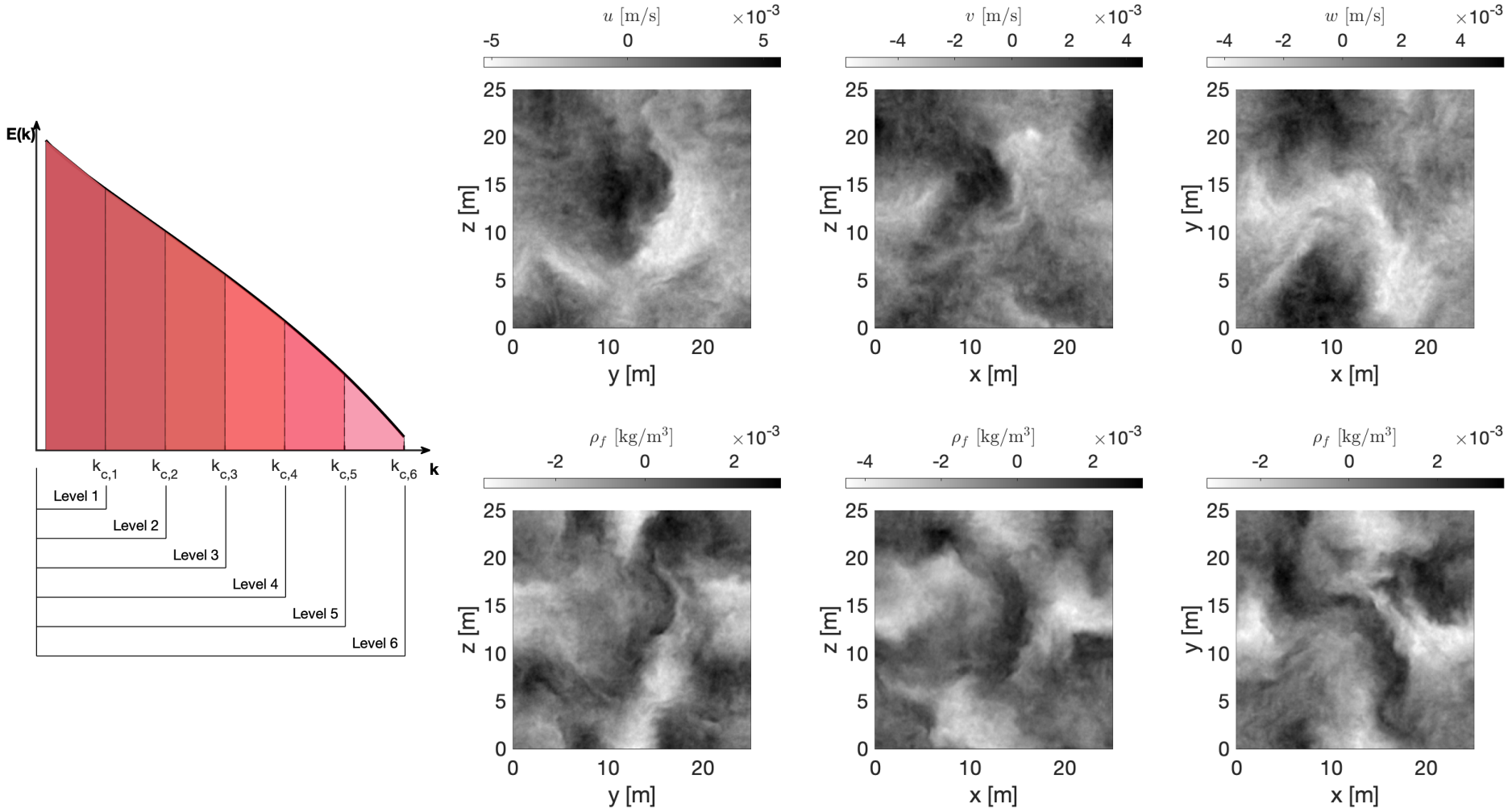

Figure 3.15: (Left) Schematic of the spectrum and different levels used for MMLM+density construction. Here $n = 1 - 6$ has been mapped. Contour plot of resulting (right, top row) velocity and (right, bottom row) density fluctuations on 3 orthogonal planes.

where

$$\oint \mathrm{d}\mathcal{S}(k) = 4\pi k^2 \tag{3.32}$$

such that

$$\Phi_{ij}(\mathbf{k}) = \frac{E(k)}{4\pi k^2}\left(\delta_{ij} - \frac{k_i k_j}{k^2}\right) = \frac{E(k)}{4\pi k^2} P_{ij}(\mathbf{k}) \tag{3.33}$$

to the calculation of the kinetic energy

$$\sum_{|q|=k} \mathbf{U}(q) \cdot \mathbf{U}^*(q) \tag{3.34}$$

which is used to rescale the velocity and density fields.

However, with the introduction of gravity in the updated MMLM+density approach, the turbulence is no longer purely isotropic. Despite this, the isotropic assumption continues to be used as an approximation since a more advanced version of MMLM, where non-isotropic spectra can be imposed, has not yet been developed. Also, the smallest scales of turbulence tend to be more isotropic, helping to justify these approximations. The comparisons with ocean probe data shown in Chapter 7 provide further support for the approach chosen in this work.

3.2 Results

Figure 3.16 shows the resulting velocity fluctuation magnitude in m/s. Figure 3.17 compares the vorticity in rad/s for the original Gaussian field in the top graphic and result of the MMLM+density approach in the bottom graphic. For the Gaussian field, the vorticity magnitude field is filled with blob-like structures while the non-Gaussian field produced by MMLM+density exhibits more intense vortex tubes, as expected for turbulent flows.

The resulting density field is shown in Figure 3.18 where the top graphic shows the relative density $\rho - \rho_o = \rho_f + \rho_z$ and the bottom graphic shows the density fluctuations ρ_f. The density fluctuations are small enough here that they are difficult to observe in the relative density plot.

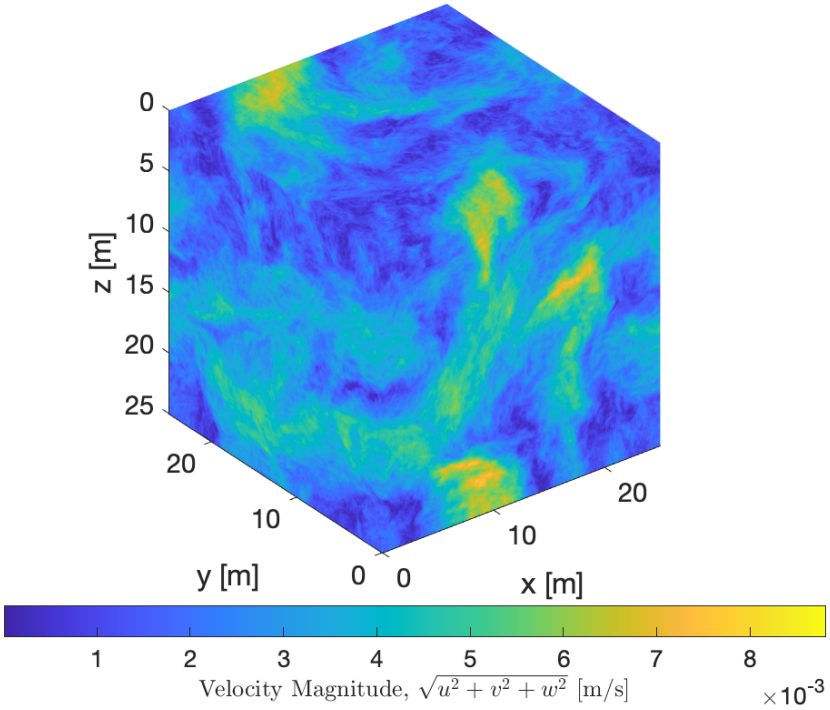

Figure 3.16: Resulting velocity fluctuation magnitude cube in m/s.

Figure 3.19 shows how the overall 3D velocity energy spectra (black line) matches the prescribed spectrum (dashed line), given by Equation 3.11. Each of the velocity components also match the spectrum with good agreement.

Figure 3.20 shows how each of the MMLM+density velocity components match the prescribed longitudinal energy spectrum.

$$E_{11}(k_1) = \int_{k_1}^{\infty} \frac{E(k)}{k} \left(1 - \frac{k_1^2}{k^2}\right) \mathrm{d}k. \tag{3.35}$$

Disagreement at large wavenumbers between the model and realization results are attributed to truncation of the integral for the realization at wavenumbers less than infinity.

Figures 3.21 and 3.22 demonstrate the non-Gaussian behavior of synthetic turbulence realizations generated by MMLM+density. Figure 3.21 shows the probability distribution function (PDF) for the normalized velocity gradient

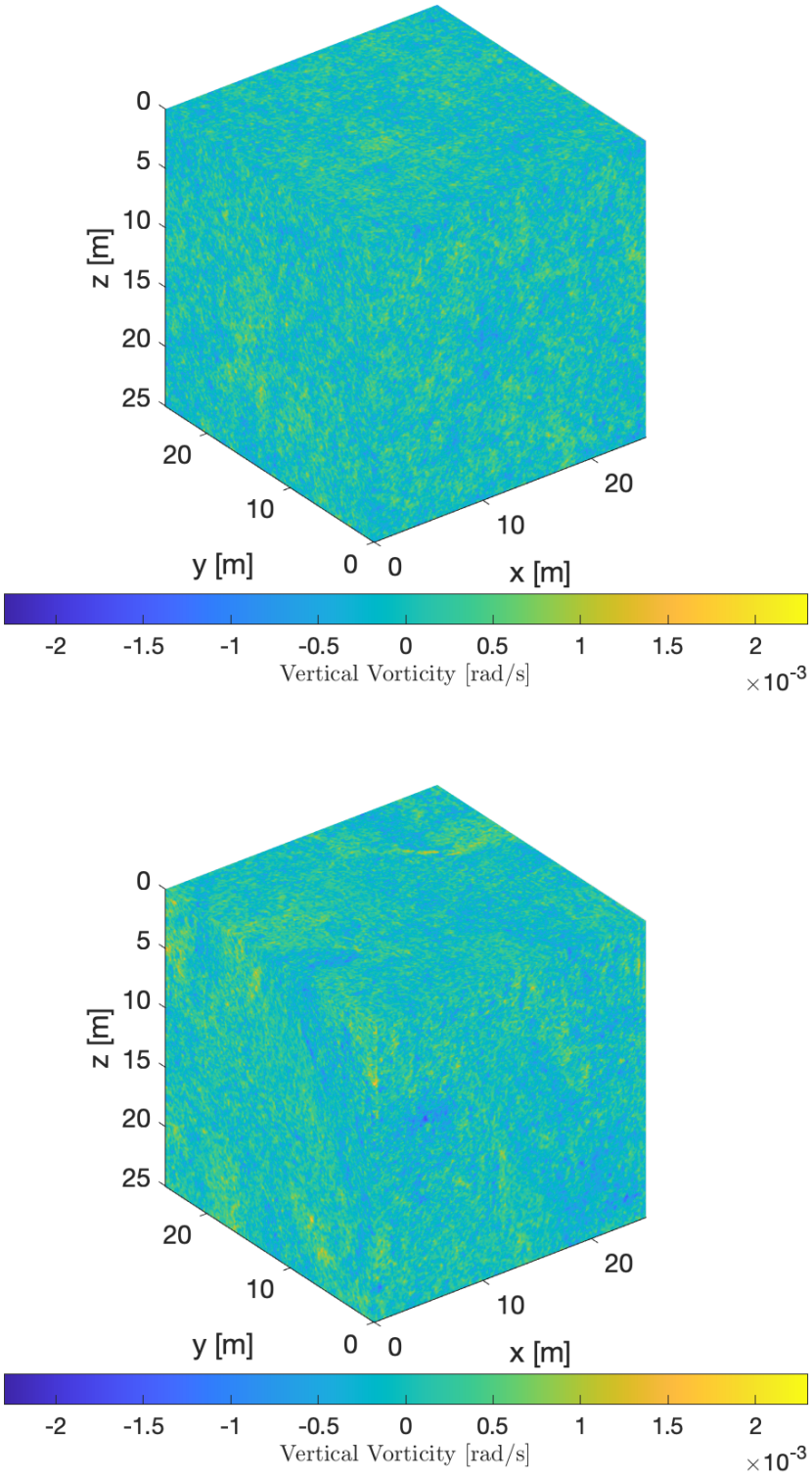

Figure 3.17: Vorticity cube in rad/s for (top) the original Gaussian field and (bottom) the MMLM+density generated field.

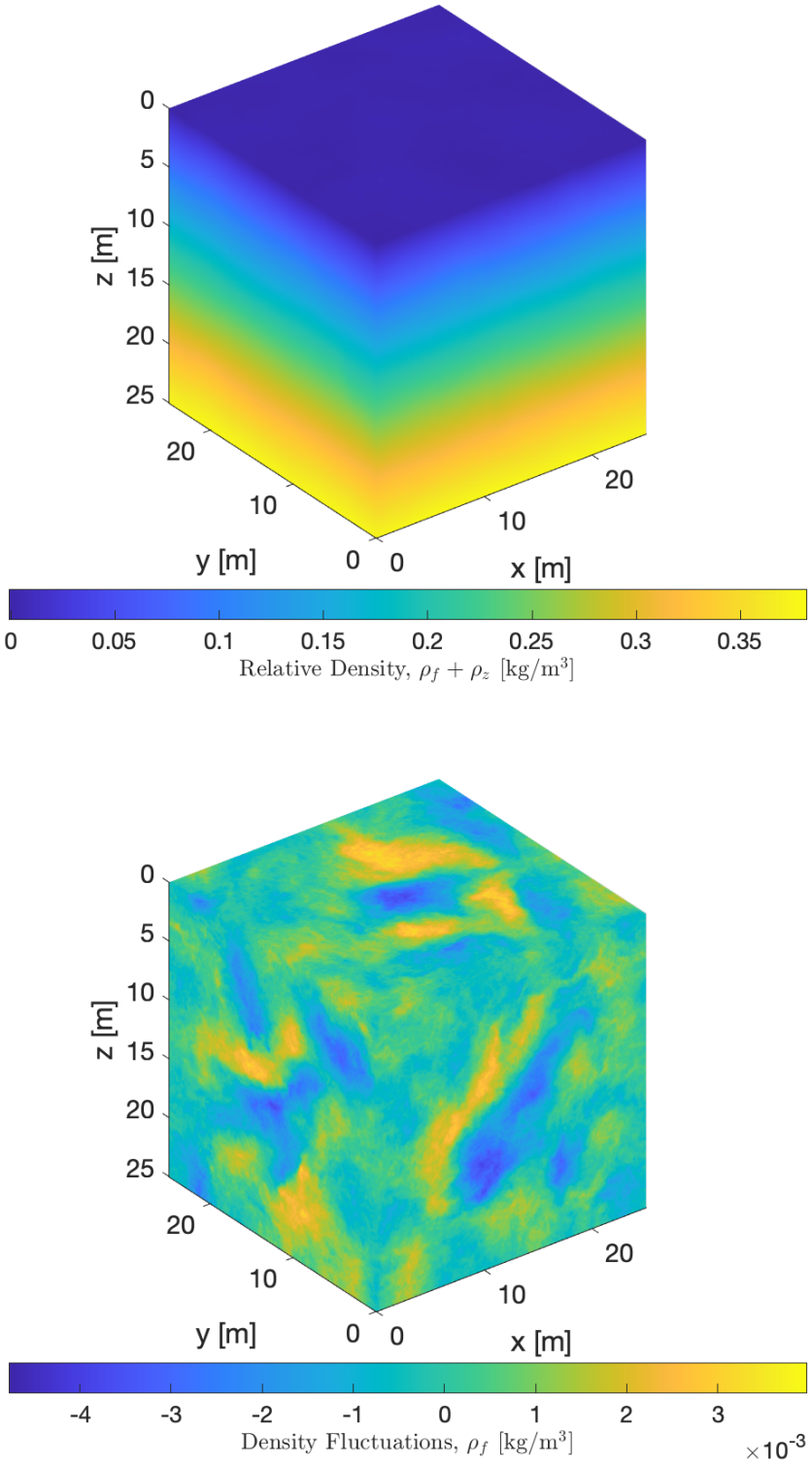

Figure 3.18: Resulting (top) density cube $\rho - \rho_o = \rho_f + \rho_z$ and (bottom) density fluctuations cube ρ_f.

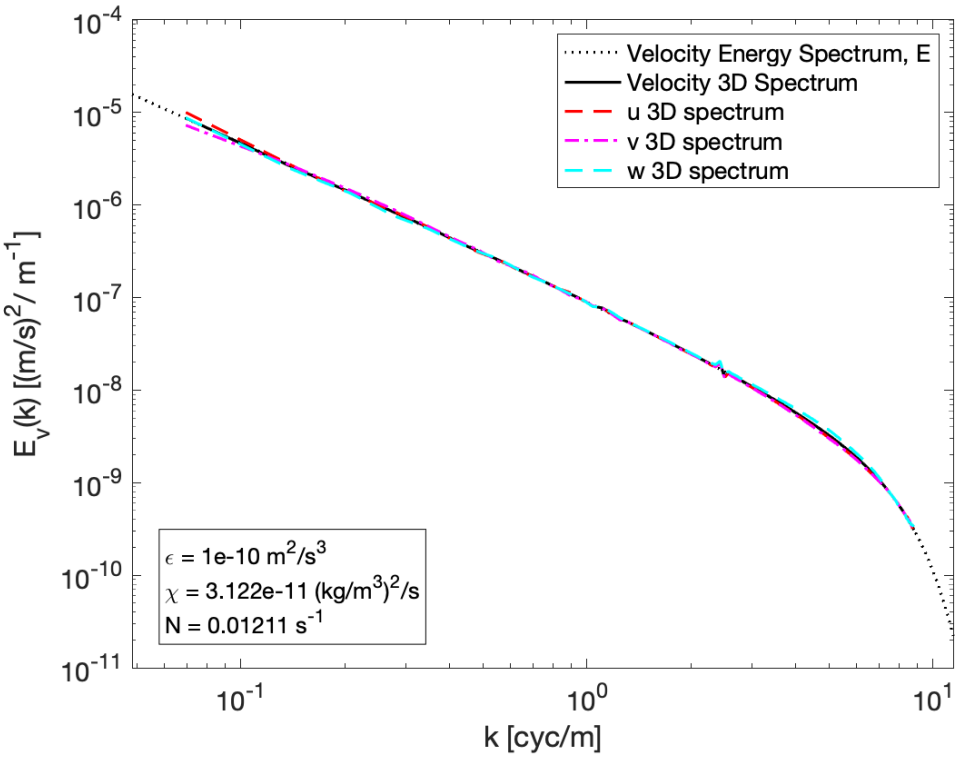

Figure 3.19: 3D velocity energy spectrum resulting from MMLM+density.

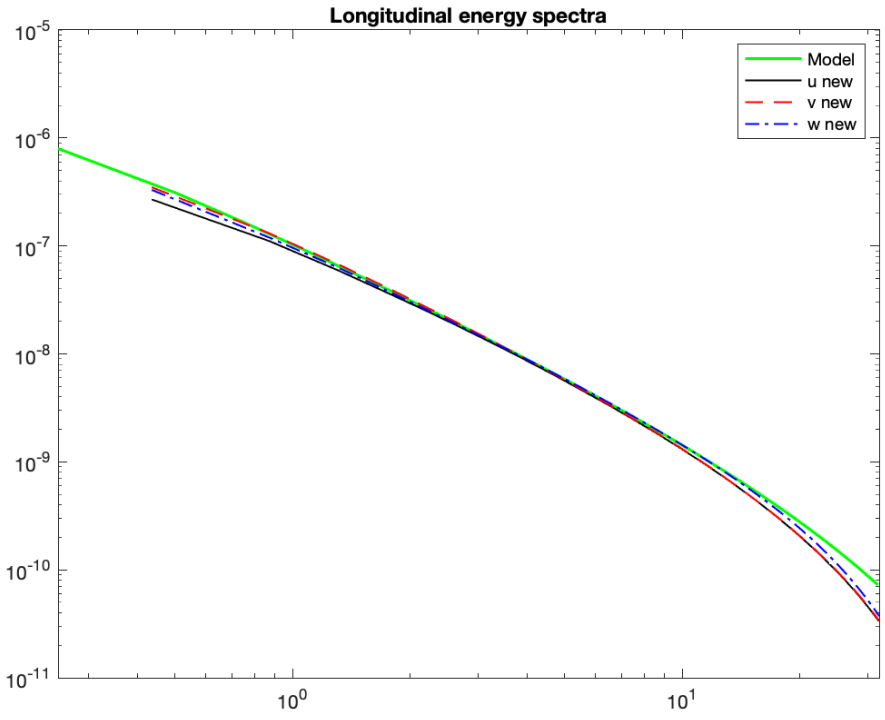

Figure 3.20: Longitudinal velocity energy spectrum.

tensor elements defined as

$$\frac{\partial_\beta u_\alpha}{\left\langle \left(\partial_\beta u_\alpha\right)^2 \right\rangle^{1/2}} \tag{3.36}$$

where $\beta = \alpha$ for the longitudinal gradient and $\beta \neq \alpha$ for the transverse gradient. Figure 3.21 shows the averages of the PDFs of the 3 longitudinal components and the 6 transverse ones. The PDF of the velocity gradients for the initial Gaussian velocity field is symmetric, and shows expected Gaussian behavior for both the longitudinal and transverse components. The non-Gaussian field produced by MMLM+density results in broader tails in the PDF, coinciding with more frequent occurrences of intense velocity gradients for both the horizontal and vertical derivatives. Also, the longitudinal gradient shows the well-known negatively skewed tail behavior.

The probability distribution function (PDF) for the density gradient is evaluated, where the density gradient is defined as

$$\frac{\partial_\beta \rho}{\left\langle \left(\partial_\beta \rho\right)^2 \right\rangle^{1/2}}. \tag{3.37}$$

In Equation 3.37 $\beta = \langle 1, 2 \rangle$ represents horizontal and $\beta = 3$ indicates vertical gradients. Behavior for the density gradients closely resembles the behavior seen for the velocity gradients. The PDF of the density gradients for the initial Gaussian velocity field also shows the expected Gaussian behavior for both the horizontal and vertical gradients. The non-Gaussian field produced by MMLM+density results in broader tails in the PDF, coinciding with more frequent occurrences of intense density gradients for both the horizontal and vertical derivatives.

Figure 3.23 shows the skewness $-S$ and Figure 3.24 shows the flatness F coefficients of the velocity increments for varying separation distances r/h

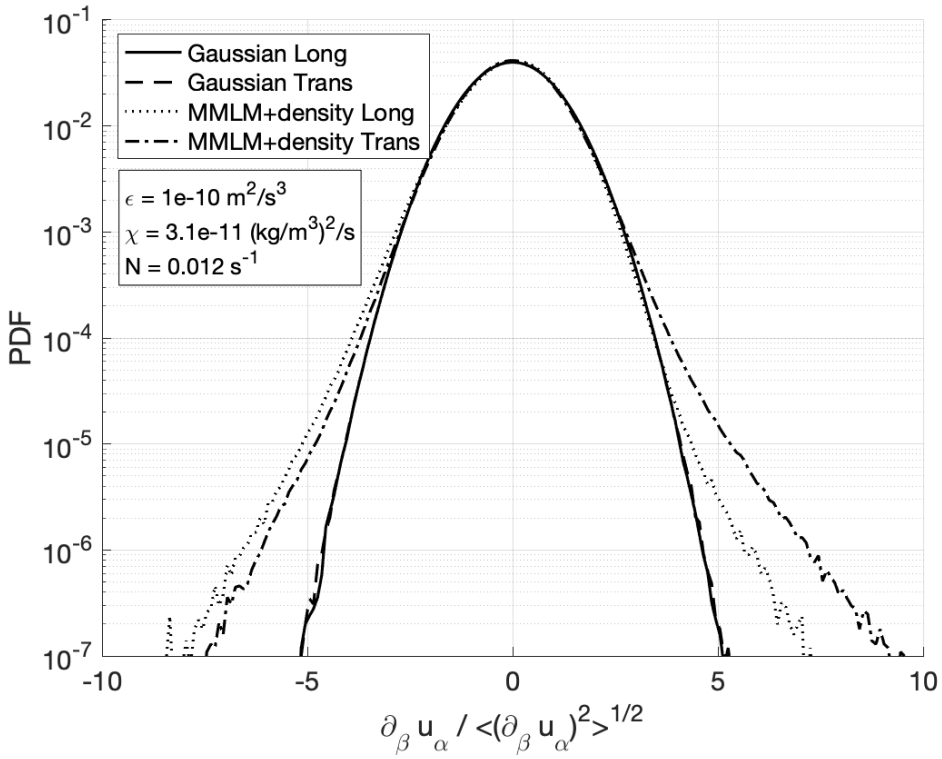

Figure 3.21: Velocity gradient.

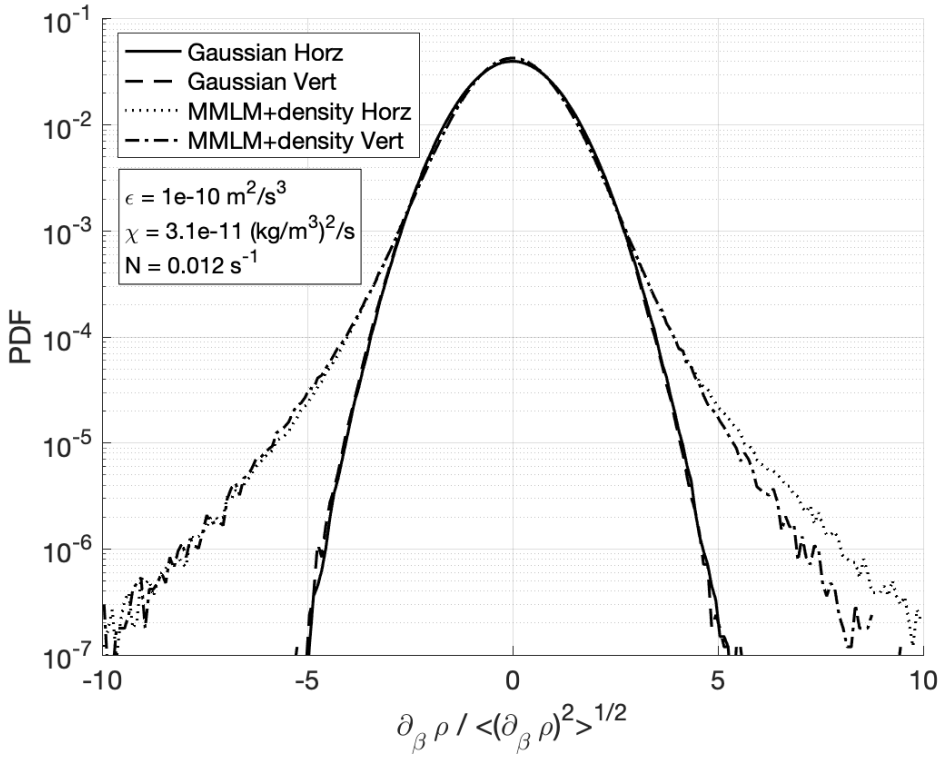

Figure 3.22: Density gradient.

where $h = \mathrm{d}x$. Skewness is defined as

$$S = \frac{\left(\Delta_\beta u_\alpha\right)^3}{\left\langle \left(\Delta_\beta u_\alpha\right)^2 \right\rangle^{3/2}} \tag{3.38}$$

and measures the asymmetry of a function with respect to its mean. When the PDF is symmetric, as with Gaussian data, the skewness is 0 [29]. Flatness is defined as

$$F = \frac{\left(\Delta_\beta u_\alpha\right)^4}{\left\langle \left(\Delta_\beta u_\alpha\right)^2 \right\rangle^2} \tag{3.39}$$

and measures how sharply peaked the values are, particularly when compared with Gaussian data which have a flatness equal to 3 [29, 30]. For both Equations 3.38 and 3.39, $\beta = \alpha$ for the longitudinal increment and $\beta \neq \alpha$ for the transverse increment. The difference operator is defined according to

$$\Delta_\beta u_\alpha = u_\alpha(\mathbf{x} + r\mathbf{e}_\beta) - u_\alpha(\mathbf{x}) \tag{3.40}$$

where $\mathbf{e}_\beta$ denotes a unit vector in the β direction.

Both the skewness and flatness peak near $r/h = 10$, exhibiting the most non-Gaussian behavior in that regime and increments become closer to Gaussian again as the scale increases. The non-Gaussian statistics observed as the result of MMLM+density are consistent with results expected from homogeneous turbulent flows [30].

3.3 Summary

In summary, the MMLM approach developed by Rosales and Meneveau which generates a non-Gaussian intermittent velocity fluctuation field is expanded to include a density scalar field, called MMLM+density. In this updated approach, the Lagrangian field distortion contains an additional term for gravitational forcing. This is done to match observed small scale turbulence behavior in the ocean which is known to be governed by both

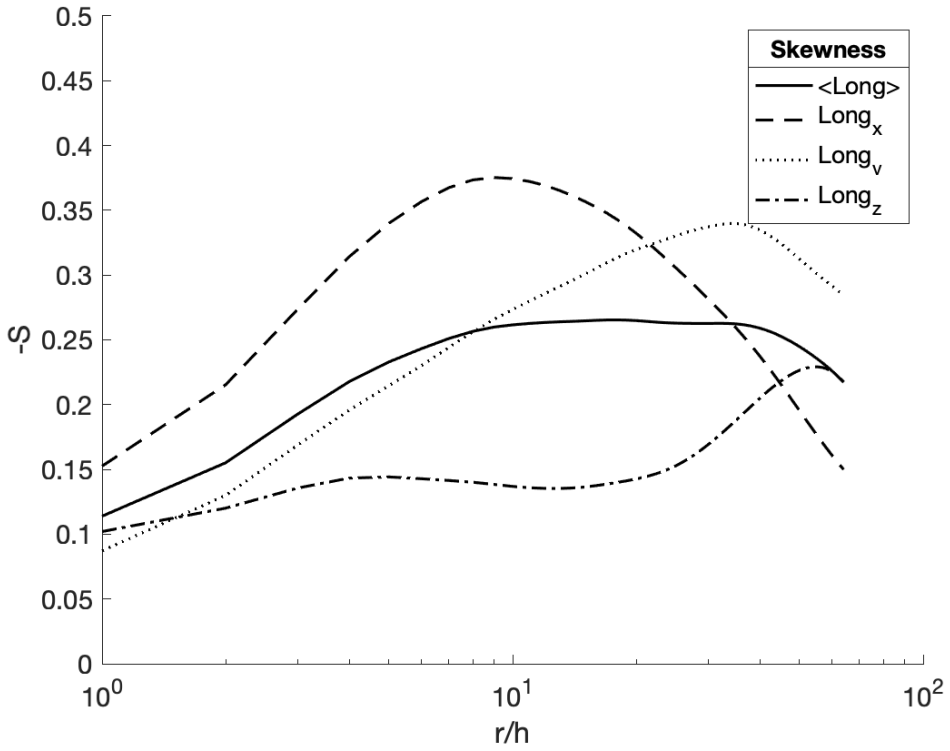

Figure 3.23: Negative of skewness factor of various longitudinal velocity increments as function of separation distances.

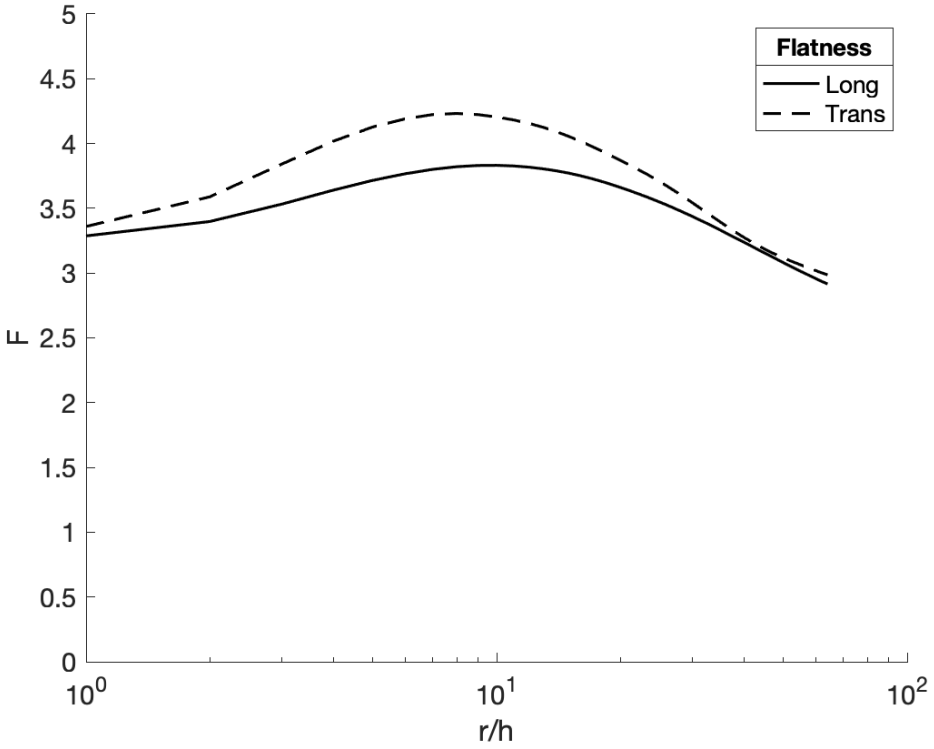

Figure 3.24: Flatness factor of various longitudinal and transverse velocity increments as function of separation distances.

background shear and buoyancy forces resulting from ambient density stratification [26].

The results of MMLM+density are shown to exhibit properties of non-Gaussian turbulence while matching the prescribed energy spectra, in contrast to the original Gaussian field before the MMLM+density algorithm is applied. The realization runs in approximately 25-30 minutes on a single processor. In comparison, a single time step of a Large Eddy Simulation (LES) code on a single processor takes 1.3 minutes. However, convergence typically takes 5000-10000 time steps such that a realization on a single processor could take 4.5-9 days for a comparable output. MMLM+density therefore represents a time savings factor of 300-600.

Intended to be blank.

Chapter 4

Parameter Estimation

4.1 Parameter Estimation Process

The synthetic turbulence realization has required parameters. While the parameters could be independently defined, these values are often coupled in the ocean environment [31–33]. Therefore, it makes sense to derive them from the existing Garret-Munk internal wave (GMIW) realization and minimize the number of inputs required to run the simulation.

The vertical structure of GMIW is defined by a Brunt-Väisälä (BV) or buoyancy frequency profile where the BV frequency, N, is defined as

$$N = \sqrt{-\frac{g}{\rho_o}\frac{\partial \rho(z)}{\partial z}} \tag{4.1}$$

and where $g = 9.8\ \mathrm{m/s^2}$ is the gravitational acceleration, ρ_o is the potential density, and $\rho(z)$ is the water density as a function of depth, z.

MMLM+density requires a background density profile, ρ_z, which is derived from the BV frequency profile used by GMIW. The MMLM+density 3D velocity spectrum, defined in Equation 3.11, and 3D density spectrum, defined in Equation 3.15 also require the kinetic energy dissipation rate, ϵ, and the dissipation rate of density fluctuations, χ, to generate the imposed velocity and density energy spectra.

Section 4.2 discusses how the the background density profile is generated, Section 4.3 discusses how the kinetic energy dissipation rate is found, and

Section 4.4 discusses the dissipation rate of density fluctuations.

4.2 Background Density Profile

Density is modeled in MMLM+density as a function of position and has 3 elements: the reference density, set to the density of fresh water, $\rho_o = 1000$ kg/m^3, the relative background density derived from the input BV frequency, ρ_z, and the density fluctuations, ρ_f.

$$\rho(\mathbf{x}) = \rho_f(\mathbf{x}) + \rho_z(\mathbf{x}) + \rho_o \tag{4.2}$$

This section discusses the relative background density, ρ_z.

A sample BV profile used in GMIW is shown in Figure 4.1. The region corresponding to a 60 m run depth (spanning from 60 m to 85 m with a length, $L = 25$ m) is highlighted in red. The portion in red is extracted and used to generate the background density profile such that

$$\rho_z(z) = \sum_{j=0}^{z} \frac{\rho_o N(j)^2 \mathrm{d}z}{g} \tag{4.3}$$

where N is the BV frequency in s^{-1}, z is the vertical coordinate in meters, and dz is the vertical step size in meters. This expression comes from integrating numerically the definition of $N(z)$ (Equation 4.1). Figure 4.2 shows the extracted BV profile in blue and the corresponding derived relative background density in red for three depths: (top) 20 m, (middle) 60 m, and (bottom) 100 m. The depth plotted here is z_{rel} used in MMLM+density.

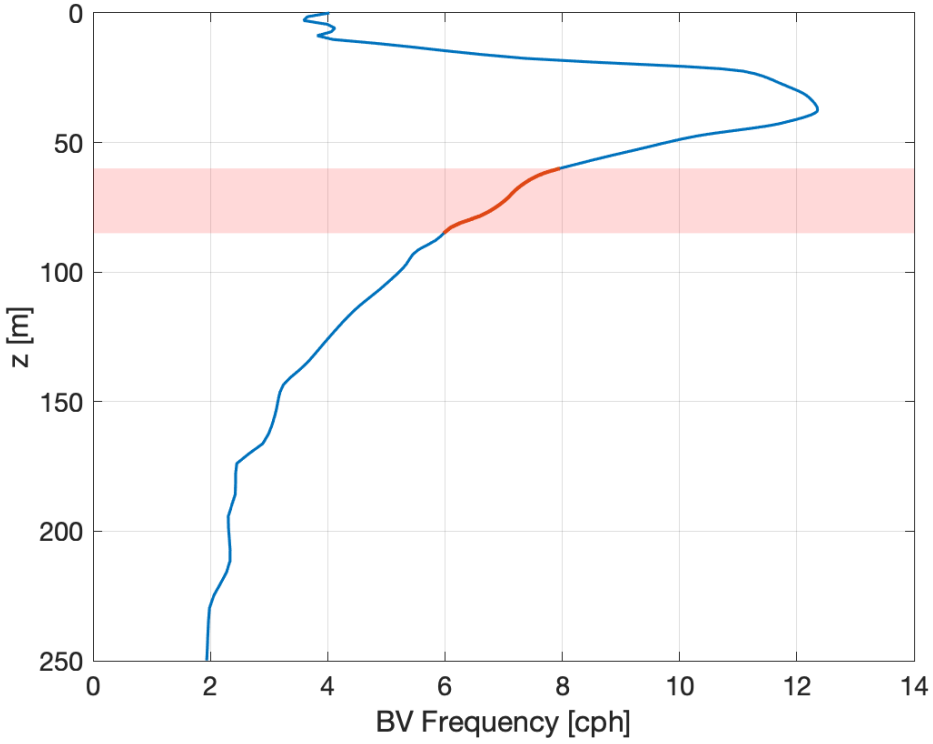

Figure 4.1: Full BV frequency profile used in GMIW. Highlighted portion of the profile corresponds to the 60 m run depth.

4.3 Use of Richardson Number to Find Kinetic Energy Dissipation Rate

The kinetic energy dissipation rate is calculated from the GMIW by first calculating the Gradient Richardson number, Ri, defined as

$$\mathrm{Ri} = \frac{N^2}{\left(\frac{\mathrm{d}u}{\mathrm{d}z}\right)^2} \tag{4.4}$$

where u is the horizontal velocity. The criterion for the flow to become unstable is $\mathrm{Ri} < \mathrm{Ri}_c$ where the critical Richardson number $\mathrm{Ri}_c \approx \frac{1}{4}$. Measurements in various ocean layers have shown that Ri is highly variable and scale dependent [11]. Figure 4.3 shows the Richardson number calculated from the GMIW velocity field and BV frequency using Equation 4.4. The horizontal gradient is averaged over x- and y- directions. This approach used 1 vertical pixel depth and averaged across 2 horizontal pixels (both x- and y- for a 4

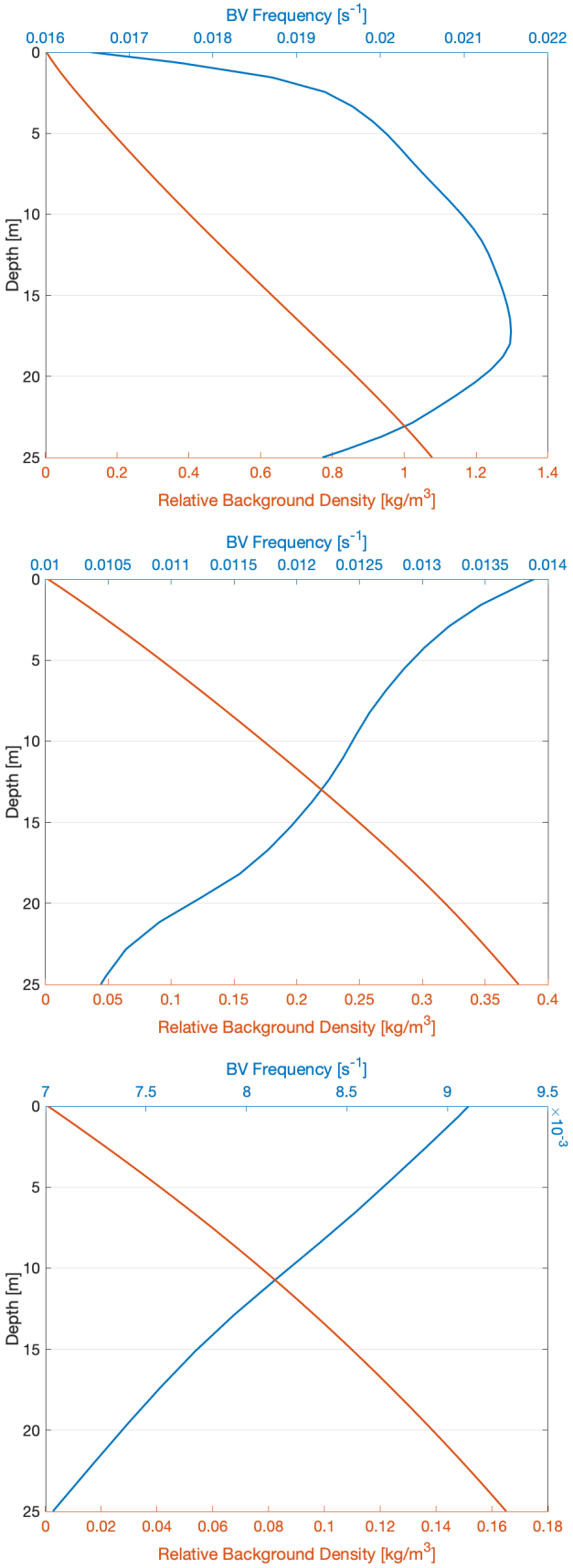

Figure 4.2: BV frequency shown in blue (top axis) at (top) 20 m, (middle) 60 m, and (bottom) 100 m. Derived relative background density shown in red (bottom axes).

pixel average). For this data, the horizontal grid size $\mathrm{d}x = 9.8$ m, and the vertical grid size is non-uniform in the range of $\mathrm{d}z = [0.8 - 0.9]$ m. The top plot of Figure 4.3 shows the full field, although the axes have a skewed aspect ratio. The bottom plot is the zoomed in region from the magenta box of the full field, shown to scale.

Kunze, Williams III, and Briscoe (1990) derived an empirical relation for the kinetic energy dissipation rate, ϵ, by evaluating the shear with stable and unstable conditions [27]. Polzin (1996) adapted the expression from [27] to a relationship between the observed frequency and intensity of low Ri events and the rate of dissipation of turbulent kinetic energy rate, such that

$$\epsilon = \frac{fr(\Delta z)^2}{96} \left\langle N^3 (\mathrm{Ri}^{-1} - \mathrm{Ri}_c^{-1})(\mathrm{Ri}^{-1/2} - \mathrm{Ri}_c^{-1/2}) \right\rangle \tag{4.5}$$

where fr is the fraction of the water column that is unstable to shear instability, Δz is the vertical depth interval over which shear and the BV frequency are calculated, and Ri_c is the critical Ri value at which mixing ceases [28]. The angled bracket $<>$ averages are over the low Ri regions. Equation 4.5 was shown to be correct to a factor of 2 for measured oceanic data by Thorpe and Jiang (1998) [12].

Any values of the kinetic energy dissipation rate calculated from Equation 4.5 less than 1×10^{-10} $\mathrm{m}^2/\mathrm{s}^3$ are set to 1×10^{-10} $\mathrm{m}^2/\mathrm{s}^3$ to more closely match the expected lower bounds on sensor measurements and facilitate comparison to ocean data. Figure 4.4 shows the results of the kinetic energy dissipation rate over the full GMIW field (with a skewed aspect ratio) in the top graphic. The bottom plot is the zoomed in region from the magenta box of the full field, plotted with a realistic aspect ratio.

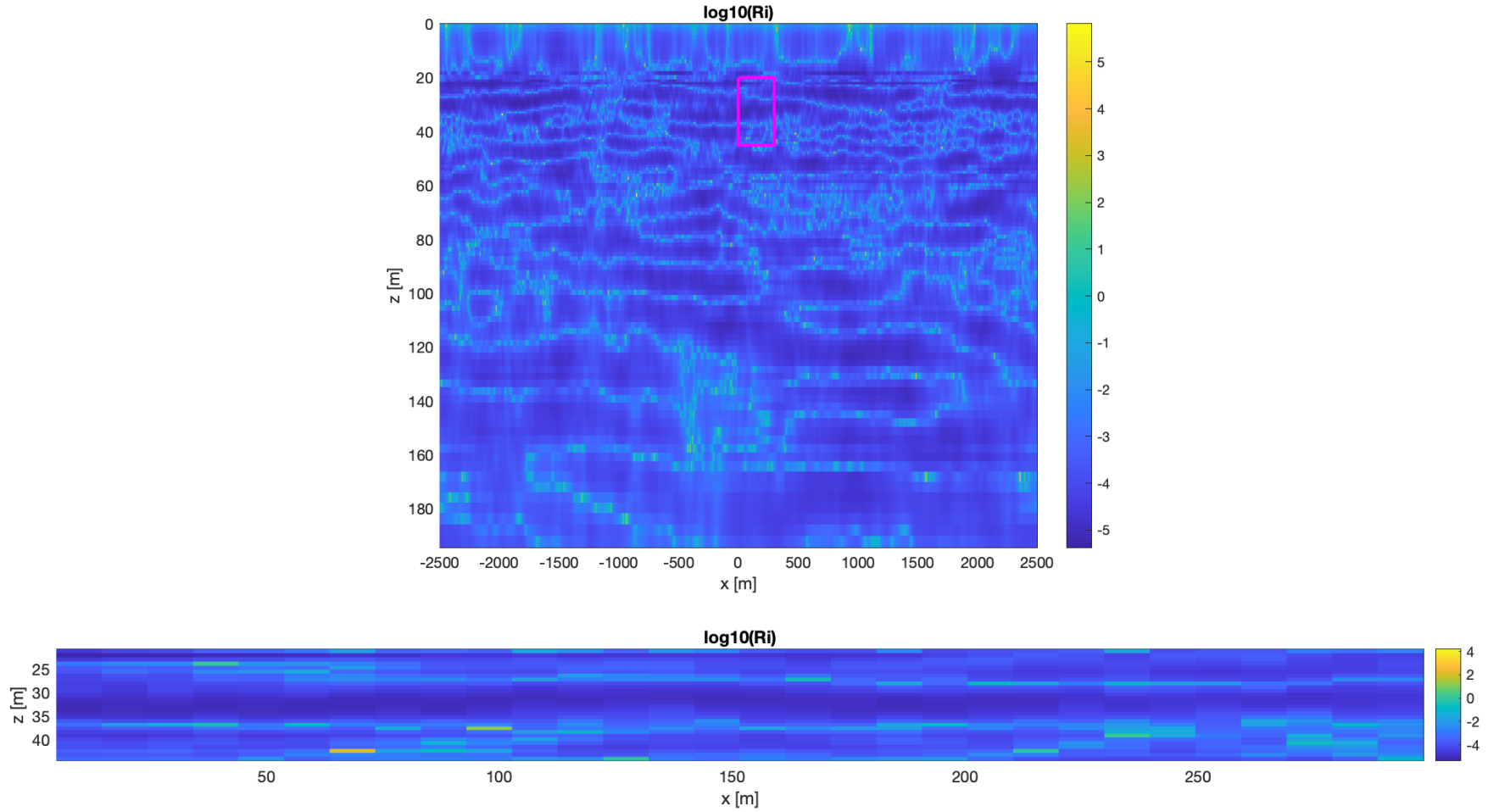

Figure 4.3: Gradient Richardson number calculated from the GMIW velocity field and BV frequency (top) full field with skewed aspect ratio and (bottom) zoomed in region with realistic aspect ratio.

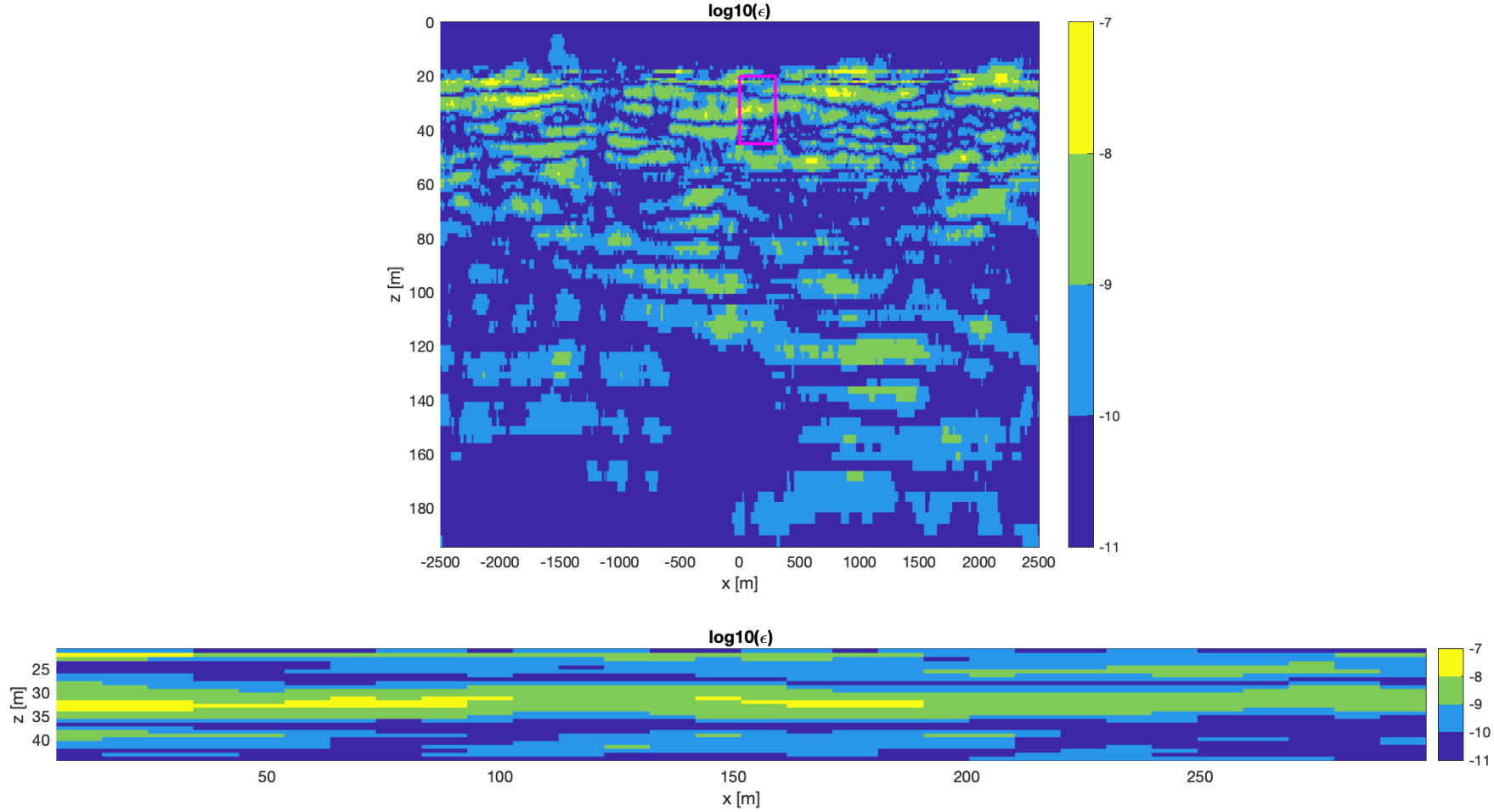

Figure 4.4: Epsilon calculated from the Richardson number (top) full field with skewed aspect ratio and (bottom) zoomed in region with realistic aspect ratio.

4.3.1 Implementing Spatially Variable Kinetic Energy Dissipation Rate into MMLM+density

Theoretical predictions show that the height dependent characteristic velocity scale, $\mathbf{u}(z)$ can be expressed as a function of the depth and kinetic energy dissipation rate, ϵ [34, 35].

$$\mathbf{u}(z) = \left(\frac{4}{5}\epsilon z\right)^{1/3} \tag{4.6}$$

This expression is obtained from the Kolmogorov '4/5' law for locally homogeneous and isotropic turbulence [30].

This prediction was tested by running MMLM+density with 5 different kinetic energy dissipation rates $\{10^{-11}, 10^{-10}, 10^{-9}, 10^{-8}, 10^{-7}\}$ $\mathrm{m}^2/\mathrm{s}^3$ while leaving all other parameters equal ($z_o = 100$ m here). Figure 4.5 plots the standard deviation for the horizontal velocities (u, v), the vertical velocity w, and the density ρ as a function of the kinetic energy dissipation rate resulting from the 5 simulations with solid lines. The figure shows scaled values for each of the standard deviations with dashed lines by using the relation

$$u_{\text{scaled}} = u_o \left(\frac{\epsilon_{\text{desired}}}{\epsilon_o}\right)^{1/3} \tag{4.7}$$

where the subscript 'o' denotes the original value from the realization and u can represent (u, v, w, ρ). The top graphic uses $\epsilon_{\text{desired}} = 10^{-9}$ $\mathrm{m}^2/\mathrm{s}^3$ while the bottom graphic uses $\epsilon_{\text{desired}} = 10^{-8}$ $\mathrm{m}^2/\mathrm{s}^3$. As expected, the standard deviation is a relatively flat line across the kinetic energy dissipation rate when applying this scaling. The red stars show the intersection of the scaled data with the original data.

The relation in Equation 4.7 is exploited during the model merging discussed in Chapter 6. MMLM+density is run using the median value of ϵ found via Equation 4.5 from the GMIW realization over the region of interest (Figure 4.4, bottom) and then velocity fluctuations are scaled using the scale factor in Equation 4.7 (the ratio of $\epsilon_{\text{desired}}$ to ϵ_o) using the height-dependent

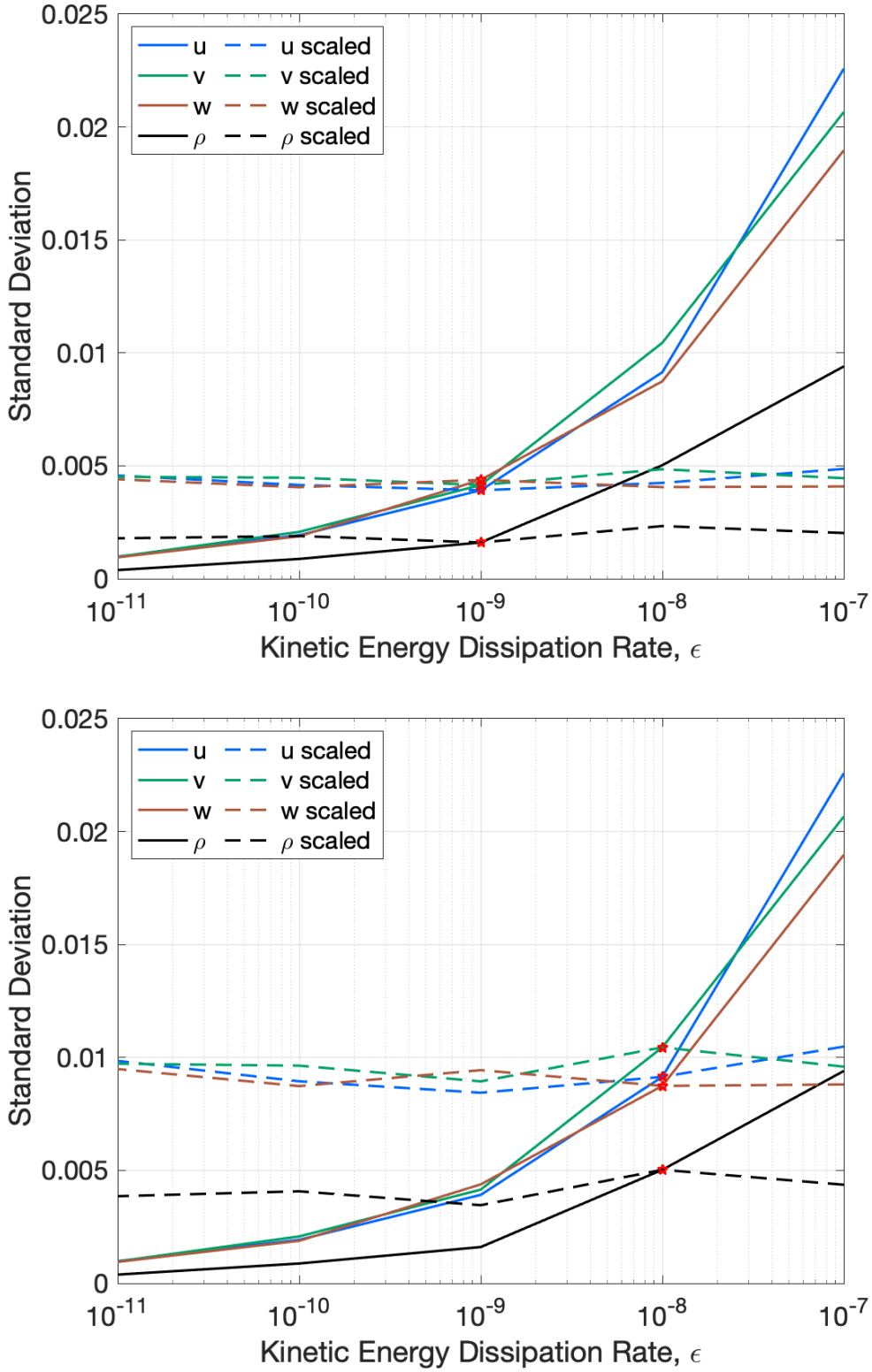

Figure 4.5: Synthetic turbulence realizations generated with one value of ϵ can be scaled to approximate another value of ϵ (top) $\epsilon_{\text{desired}} = 10^{-9}$ m^2/s^3 (bottom) $\epsilon_{\text{desired}} = 10^{-8}$ m^2/s^3.

kinetic energy dissipation rate before the models are combined.

4.4 Dissipation Rate of Density Fluctuations

The spectrum of density fluctuations is defined in Equation 3.15 as

$$E_\rho(k) = C_{oc}\epsilon^{-1/3}k^p\chi f_\eta f_{\text{damp}}$$

where χ is the dissipation rate of density fluctuations.

More commonly, χ is defined as the dissipation rate of temperature fluctuations, expressed as

$$\chi = 6\kappa_T \left\langle \left(\frac{\partial T'}{\partial z}\right)^2 \right\rangle \tag{4.8}$$

where $\left(\frac{\partial T'}{\partial z}\right)^2$ is the small scale temperature gradient, $\kappa_T \approx 1.4 \times 10^{-7}\text{m}^2/\text{s}$ is the molecular thermal diffusivity, and the angled brackets indicate averaging [19, 36, 37]. This expression for χ corresponds to the rate of decrease of variance of temperature fluctuations due to diffusion of heat in a relatively isotropic environment [36].

In order to simplify the analysis, the number of free parameters are minimized by making the following assumptions. In a thermally driven environment, the density is primarily a function of temperature. For fluctuations of the density field treated as a transported scalar, the equivalent definition of a scalar variance dissipation rate (for the density variance dissipation) reads

$$\chi = 6\kappa_\rho \left\langle \left(\frac{\partial \rho}{\partial z}\right)^2 \right\rangle \tag{4.9}$$

where $\frac{\mathrm{d}\rho}{\mathrm{d}z}$ is the density gradient, related to the BV frequency according to Section 4.2. Known from turbulence theory, the rate of dissipation can also be evaluated using the mean density gradient and eddy-diffusivity coefficient, i.e.,

$$\chi = K_\rho \left\langle \left(\frac{\partial \rho}{\partial z}\right)^2 \right\rangle. \tag{4.10}$$

The eddy-diffusivity coefficient, K_ρ can be evaluated based on the BV frequency and the dissipation rate according to [33]

$$K_\rho = \frac{\Gamma \epsilon}{N^2} \tag{4.11}$$

where $\Gamma = 0.2$ is a known coefficient efficiency factor [33]. From Equations 2.1, 4.10, and 4.11, the dissipation rate of density fluctuations is defined as

$$\chi = \frac{\Gamma \rho_o^2 \epsilon}{g^2 N^2} \left\langle N^4 \right\rangle . \tag{4.12}$$

4.5 Parameter Estimation Summary

The methods described in this chapter to estimate parameters represent one way to couple the required parameters between the two synthetic turbulence realizations used in this work (GMIW and MMLM+density). The comparison of the results with ocean data are shown to be favorable (see Chapter 7) which supports the methodology chosen here.

Intended to be blank.

Chapter 5

MMLM+density Tiling

5.1 Domain Expansion through Tiling

The end realization is desired to have a horizontal grid resolution of nominally 1 m with approximately 10 cm vertical resolution and cover a large horizontal domain (300 m x 300 m). The output of the MMLM+density realization, discussed in Chapter 3 is shown with a uniform grid resolution of 9.8 cm but extends only 25 m in all directions.

The conjecture is made that the MMLM+density realizations, referred to as tiles, could be repeated and reused. A fixed number of tiles are thus merged together horizontally to create a larger domain without the need to generate a large number of individual tiles and incur the associated computational expense.

Additionally, with a required non-uniform grid, consideration is needed as to whether the scales resolved vertically and horizontally are within the same turbulence regime. The use of grids that resolve the buoyancy scale, L_b, in the vertical but not the horizontal may filter near-isotropic motions on small scales where the buoyancy scale is defined as $L_b \equiv 2\pi u_{\text{rms}}/N$, N is the BV frequency, and u_{rms} is the root mean square velocity [38]. By using the tile and down sample approach, the effective grid resolutions are resolved to the desired scales but without the complication of having to consider the downscale cascade of stratified turbulence at multiple scales.

The larger field is generated with an overlap-add method which is implemented using a Hann window with 50% overlap to first tile in one horizontal direction (e.g., x-dir) to create strips, then by overlapping the strips to tile in the other horizontal direction (e.g., y-dir) (Figure 5.1). This approach has been used by various communities to reduce edge effects in imagery and sound [39–41]. The Hann window is defined as

$$w(n) = 0.5\left[1 - \cos\left(2\pi\frac{n}{N}\right)\right] \tag{5.1}$$

where N is the number of points in the window and $0 < n \leq N$. The Hann window is repeated in the non-overlapping direction, as shown in the central part of Figure 5.1. The first and last tile in the series only taper on one side such that the first tile follows

$$w_{\text{first}}(n) = \begin{cases} 1; & 0 < n \leq \frac{N}{2} \\ 0.5\left[1 - \cos\left(2\pi\frac{n}{N}\right)\right]; & \frac{N}{2} < n \leq N \end{cases} \tag{5.2}$$

and similarly, the last tile follows the form

$$w_{\text{last}}(n) = \begin{cases} 0.5\left[1 - \cos\left(2\pi\frac{n}{N}\right)\right]; & 0 < n \leq \frac{N}{2} \\ 1; & \frac{N}{2} < n \leq N \end{cases} \tag{5.3}$$

The overlap-add and window tapering removes any edge effects that could be induced from tiling and keeps the relative magnitude of the resulting field equal. Considering two adjoining tiles which overlap over the second half of the first tile and the first half of the second tile, the sum of $w(n_1)$ from $\frac{N}{2} < n_1 \leq N$ plus $w(n_2)$ from $0 < n_2 \leq \frac{N}{2}$ is unity throughout the overlapped domain. This means that the first tile dominates close to $n_1 = \frac{N}{2}$ while the second tile has minimal effect. Towards the end of the overlap region, the second tile dominates while the first tile tapers off.

Figure 5.1 shows the overlap-add method using 5 cartoon realizations, each of a different color. While no tapering is used in the cartoon in Figure 5.1 and edges are therefore largely visible, more than just 5 colors can be observed in the subsequent steps of the overlap-add cartoon.

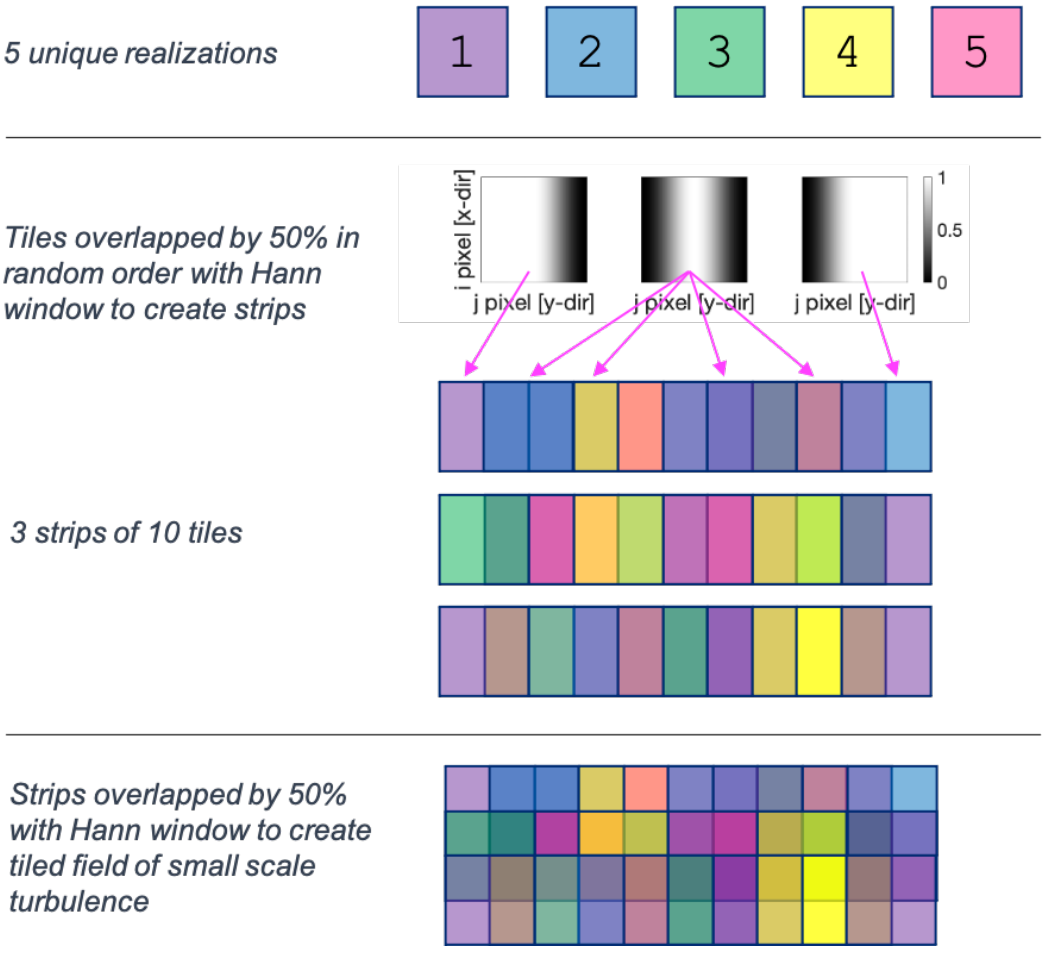

Figure 5.1: Tiling overview.

5.2 Tile Reuse

Despite the lack of edge effects, using a small number of tiles (say, 5) will create periodic features which can be easily identified and associated with the tile positions. An example is shown in Figure 5.2 with 5 unique tiles overlaid to generate a merged field with 22 x 10 tiles according to the procedure in Section 5.1. The top portion of the figure shows the horizontal velocity while the bottom shows the horizontal velocity overlaid with the tile number.

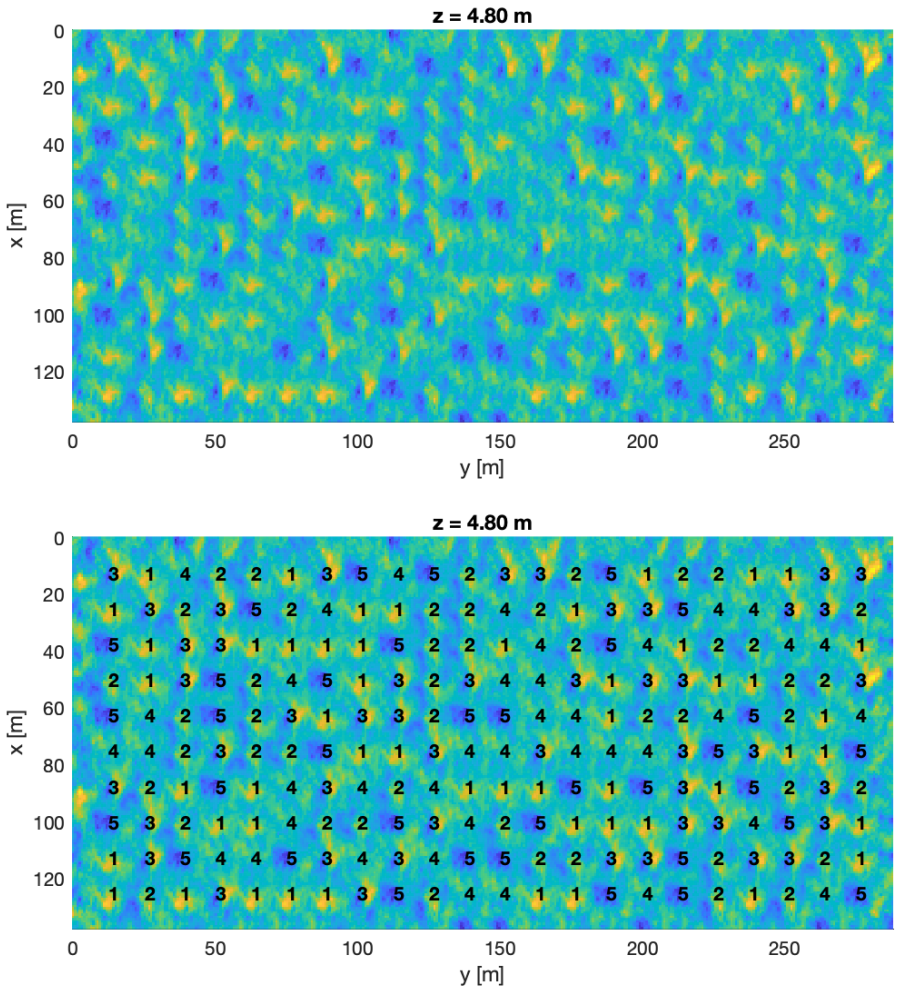

Figure 5.2: Tiling reuse with overlap only (top) shows horizontal velocity while (bottom) overlays the tile number.

To reduce the effects of repeatable features, the periodic boundary conditions of the MMLM+density results is leveraged. The tiles are shifted by a random amount in 3 dimensions before tiling, allowing a single simulation

to go farther. Figure 5.3 demonstrates how a single tile can be shifted in each dimension to generate an effectively new tile. In the figure, the horizontal velocity is plotted for 4 different cases: (a) the original tile realization as output from MMLM+density, (b) the tile shifted in the x dimension by $N/2$, (c) the tile shifted in the y dimension by $N/2$, and (d) a random shift in each of the 3 dimensions (x by 230, y by 27, and z by 224).

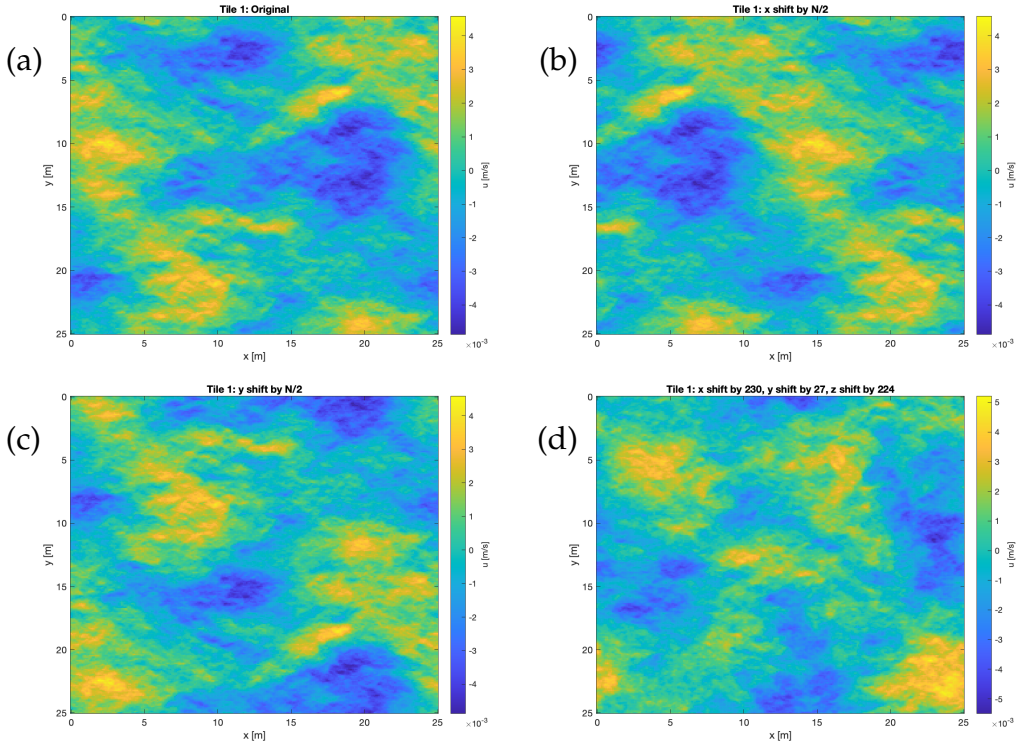

Figure 5.3: Tiling reuse demonstration where (a) shows the original tile (b) shows the tile shifted in the x dimension by N/2 (c) shows the tile shifted in the y dimension by N/2 and (d) shows a random shift in each of the 3 dimensions.

While there are some similarities between the shifted tiles shown in Figure 5.3, particularly between (a), (b), and (c), which are in the same z-plane, the tiles look overall unique. Repeating the tiling procedure with the tile shift step, Figure 5.4 shows the updated merged results where the top graphic shows the horizontal velocity and the bottom graphic overlays the tile number. The magenta box highlights a region which utilizes the same original tile and emphasizes the lack of periodic features that was previously observed in Figure 5.2.

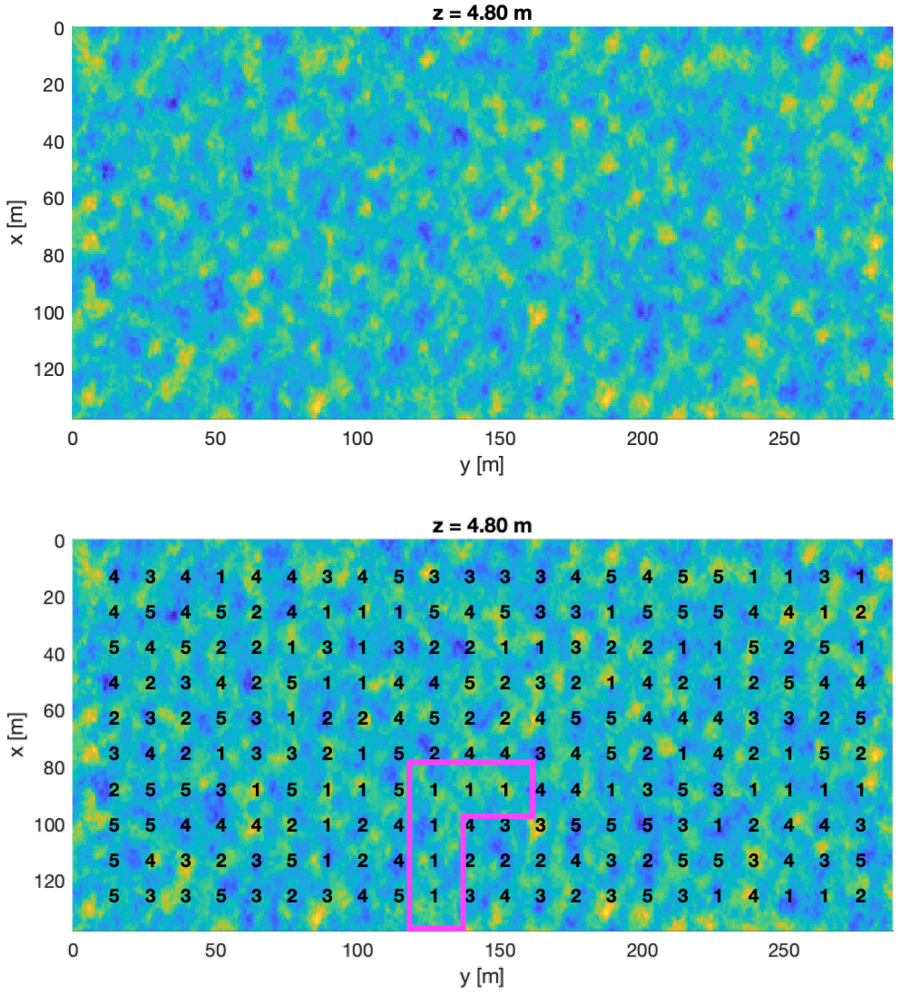

Figure 5.4: Tiling reuse with overlap and tile shifting (top) shows horizontal velocity while (bottom) overlays the tile number. The magenta box highlights a region with the same original tile and emphasizes the lack of periodic features.

5.3 Single Tile Horizontal Down Sampling

The desired realization has a horizontal grid resolution of nominally 1 m and 10 cm vertical resolution. Using purely tiling (overlap and shift), the resolution for both horizontal and vertical would both be 10 cm with $N = 256$ and $L = 25$ m. Depending how many overlapping tiles are used, this field can get unwieldy if maintaining the native horizontal resolution. Therefore, the tiles are down sampled horizontally by a factor, f_w, before tiling takes place.

Before down sampling, filtering is used to avoid aliasing errors. The down sampling procedure convolves the original tile with a rectangular window sized to f_w x f_w x 1 pixels and is normalized by the number of points in the window, f_w^2. Only the central part of the convolution is maintained and this field is then sub-sampled by f_w pixels in each of the horizontal dimensions to result in a horizontally down selected tile. Figure 5.5 shows an example with the original horizontal velocity in the top graphic and the output from the down select process in the bottom graphic for $f_w = 8$. Note that this window size results in a horizontal resolution of 0.78 m, slightly finer than the minimum resolution desired.

5.4 Tiled Spectra

The 1D velocity spectrum of the merged tile is shown in Figure 5.6 by the blue line. Also plotted is the prescribed 3D energy spectrum for velocity in green used in MMLM+density (Equation 3.11) scaled by 18/55 to approximate a 1D spectrum. The resulting spectrum from a MMLM+density tile is shown in magenta and the corresponding tile's down selected spectrum is shown in cyan.

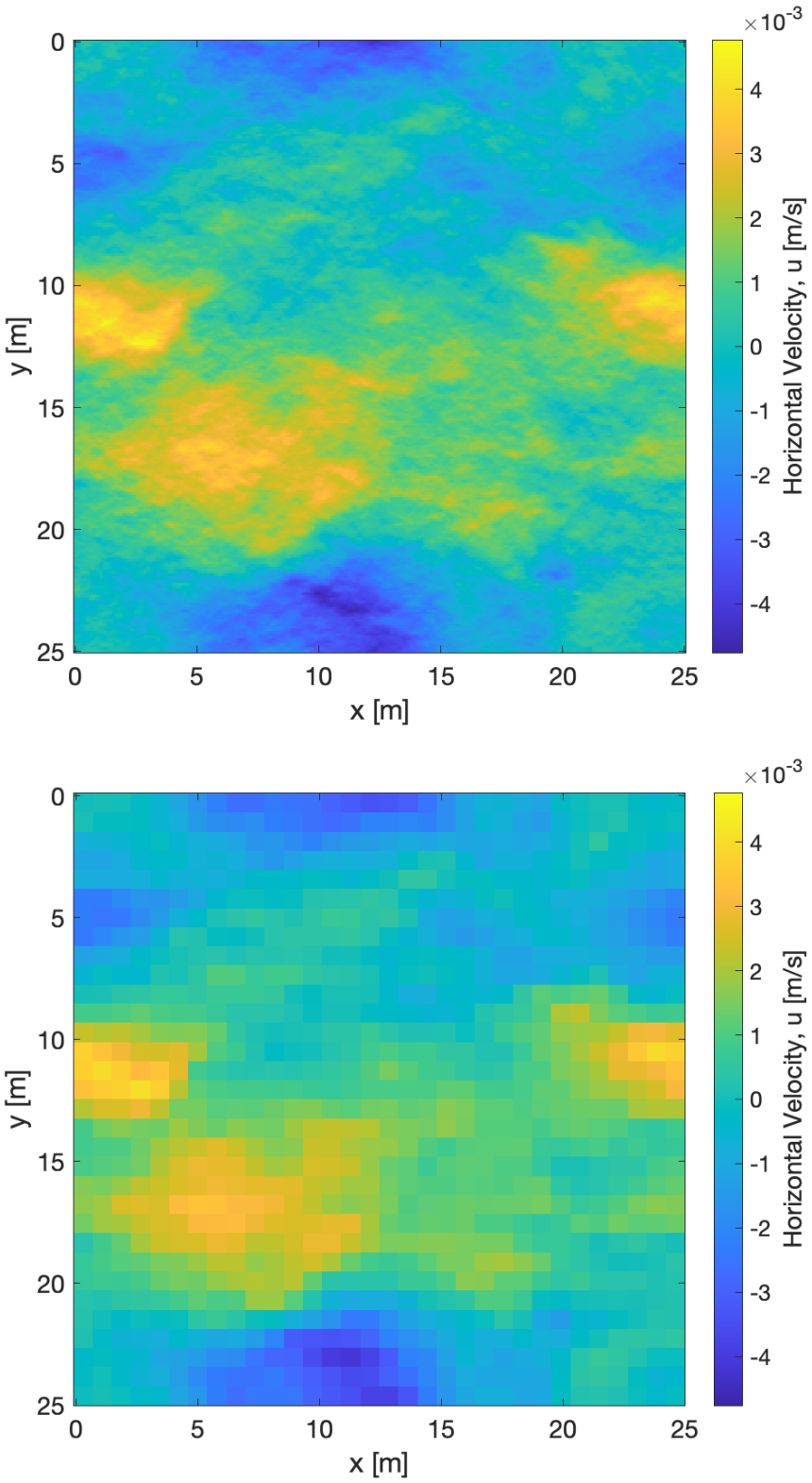

Figure 5.5: Tile down sampling example where (top) shows the original tile and (bottom) shows post down sampling for a single horizontal slice for $f_w = 8$.

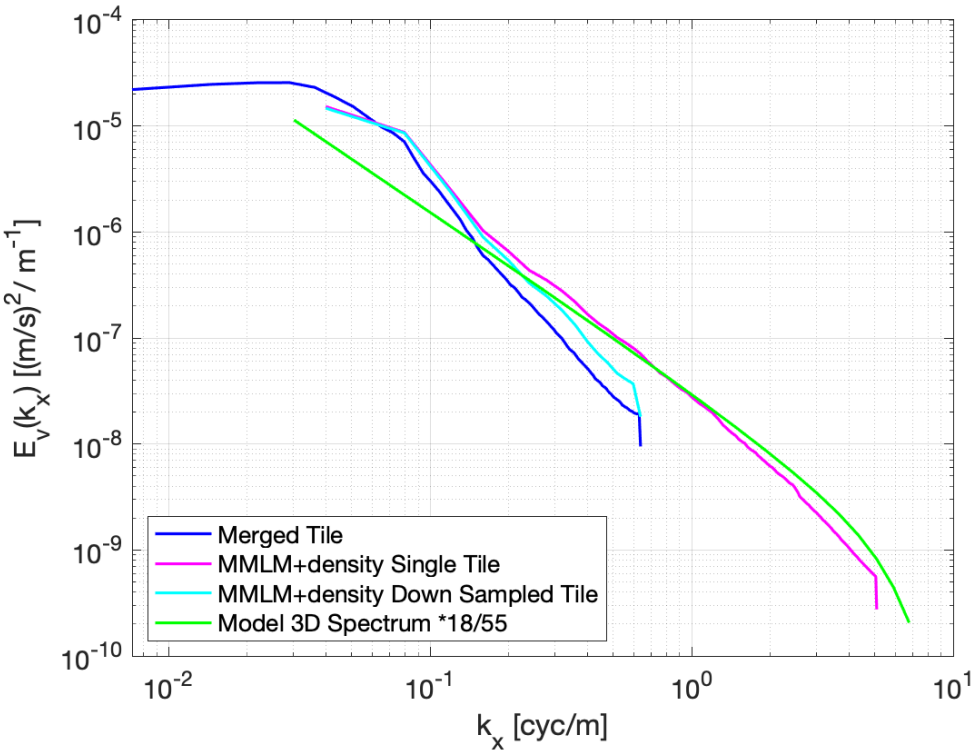

Figure 5.6: Tiled spectra comparison.

Intended to be blank.

Chapter 6

Model Merging

6.1 Merging Procedure

Once the MMLM+density fields have been tiled, the data is ready to be scaled by the kinetic energy dissipation rate, as discussed in Chapter 4 and merged with the GMIW realization.

The first step in the process is to extract a subsection of the GMIW field which corresponds to the depth used for the MMLM+density realization, z_o and desired horizontal offset (x_o, y_o), the default value set to the center of the GMIW realization, $(0, 0)$. The size of the GMIW field used here spans 5000 m in x, 5000 m in y, and approximately 200 m in z. The subset of GMIW covers the same domain as the desired output, so 300 m in x, 300 m in y, and 25 m in z.

The extracted GMIW data includes the kinetic energy dissipation rate estimation at each GMIW grid point. The data is linearly interpolated to the scale of the tiled MMLM+density grid.

The relation from Chapter 4 on how to scale the output field to a desired kinetic energy dissipation rate, ϵ, (Equation 4.7) is used to scale the MMLM+density fields (velocity components and density) to a spatially dependent value of the kinetic energy dissipation rate. The output fields are

then calculated by

$$u(\mathbf{x}) = u_{\text{GMIW}}(\mathbf{x}) + u_{\text{Md}}(\mathbf{x}) \left(\frac{\epsilon_{\text{desired}}(\mathbf{x})}{\epsilon_{\text{Md}}} \right)^{1/3} \tag{6.1}$$

where u can represent (u, v, w, ρ) and the subscript 'Md' denotes the values used in the MMLM+density realization.

Figures 6.1 and 6.2 show the desired kinetic energy dissipation rate, $\epsilon_{\text{desired}}$, for an example horizontal and vertical slice, respectively. The black box outlines the region over which the full realization is calculated. Inside the black box, $\epsilon_{\text{desired}}$ is shown with the linearly interpolated resolution while outside the box, the native GMIW resolution is shown. Both Figures 6.1 and 6.2 have regions of high and low kinetic energy dissipation rate with the horizontal slice having a higher rate in the upper right of the figure and the vertical slice having a higher rate in a patch along the top of the frame, higher closer to $y = 0$.

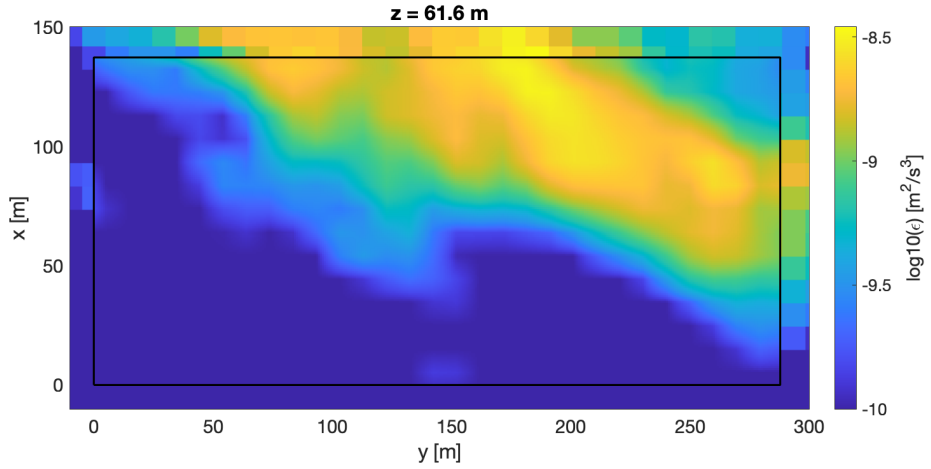

Figure 6.1: Horizontal slice of the kinetic energy dissipation rate, ϵ_{Md}.

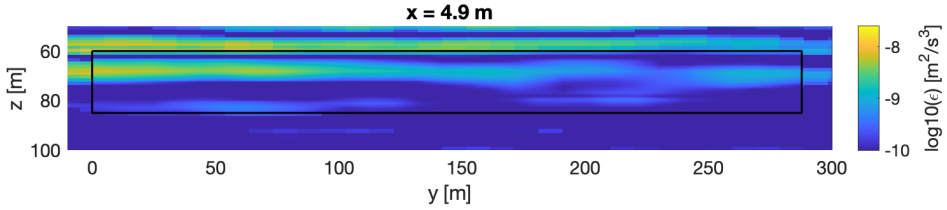

Figure 6.2: Vertical slice of the kinetic energy dissipation rate, ϵ_{Md}.

Figures 6.3 and 6.4 show the horizontal velocity for the same horizontal

and vertical slices shown in Figures 6.1 and 6.2. The top graphic of Figures 6.3 and 6.4 show the original GMIW realization and the bottom shows the results after model merging. Figures 6.5 and 6.6 show the vertical velocity and 6.7 and 6.8 show the density.

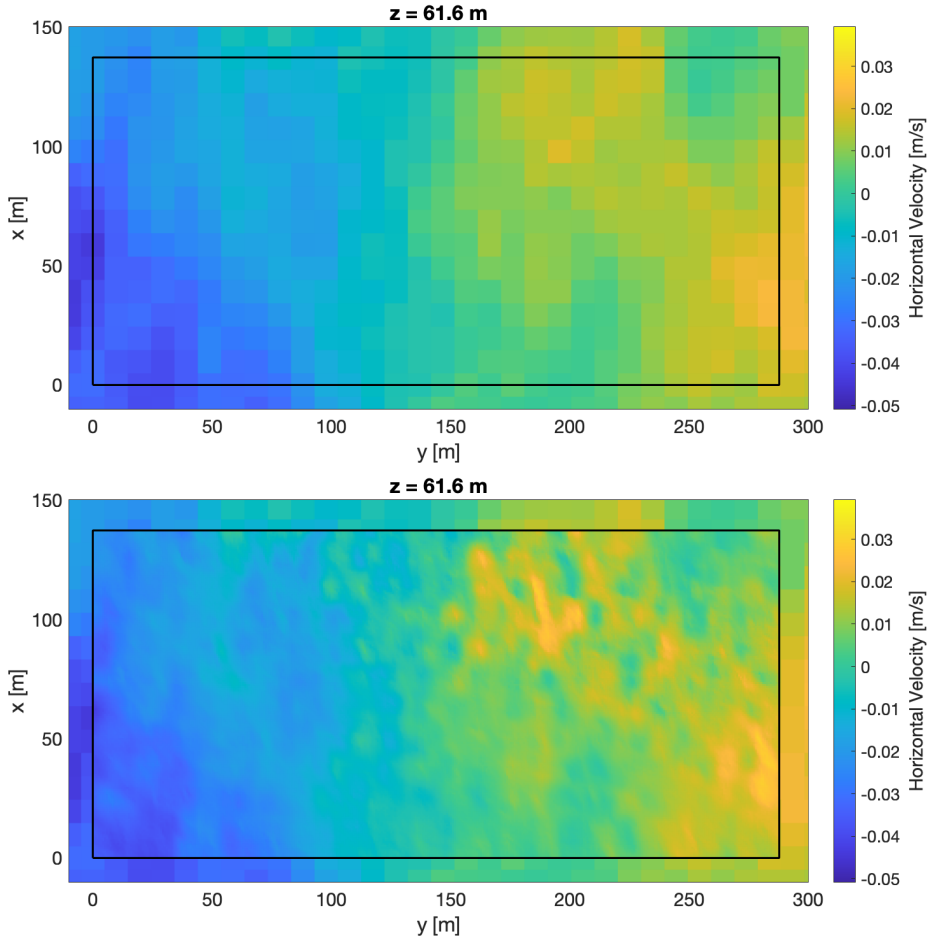

Figure 6.3: Horizontal slice of horizontal velocity (top) GMIW realization (bottom) after model merging.

6.2 Joined Spectra

Figure 6.9 shows the velocity spectrum after model merging (black line) and all of the interim spectra from each step. The interim spectra include the full GMIW spectrum (red line), the GMIW spectrum over the region of interest (brown line), the spectrum from the interpolated GMIW data (cyan line). Also shown is the model 3D spectrum from MMLM+density scaled by 18/55 (green line), the resulting spectrum from a single MMLM+density tile

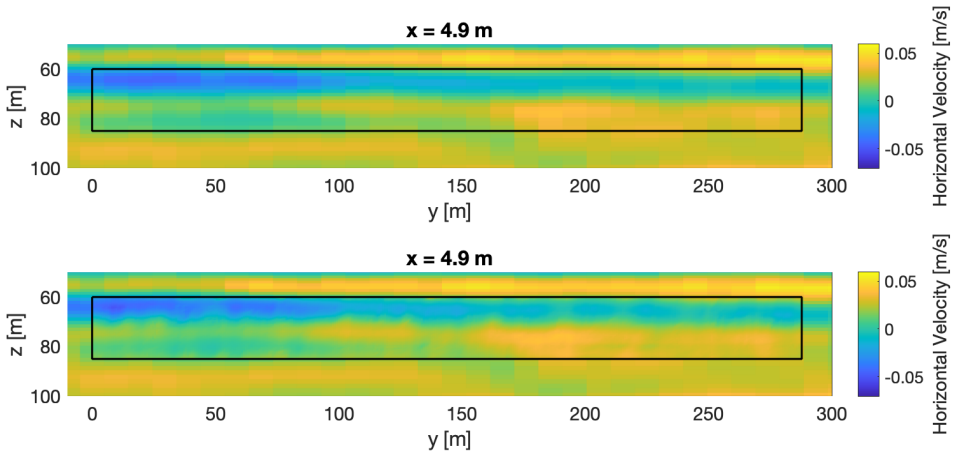

Figure 6.4: Vertical slice of horizontal velocity (top) GMIW realization (bottom) after model merging.

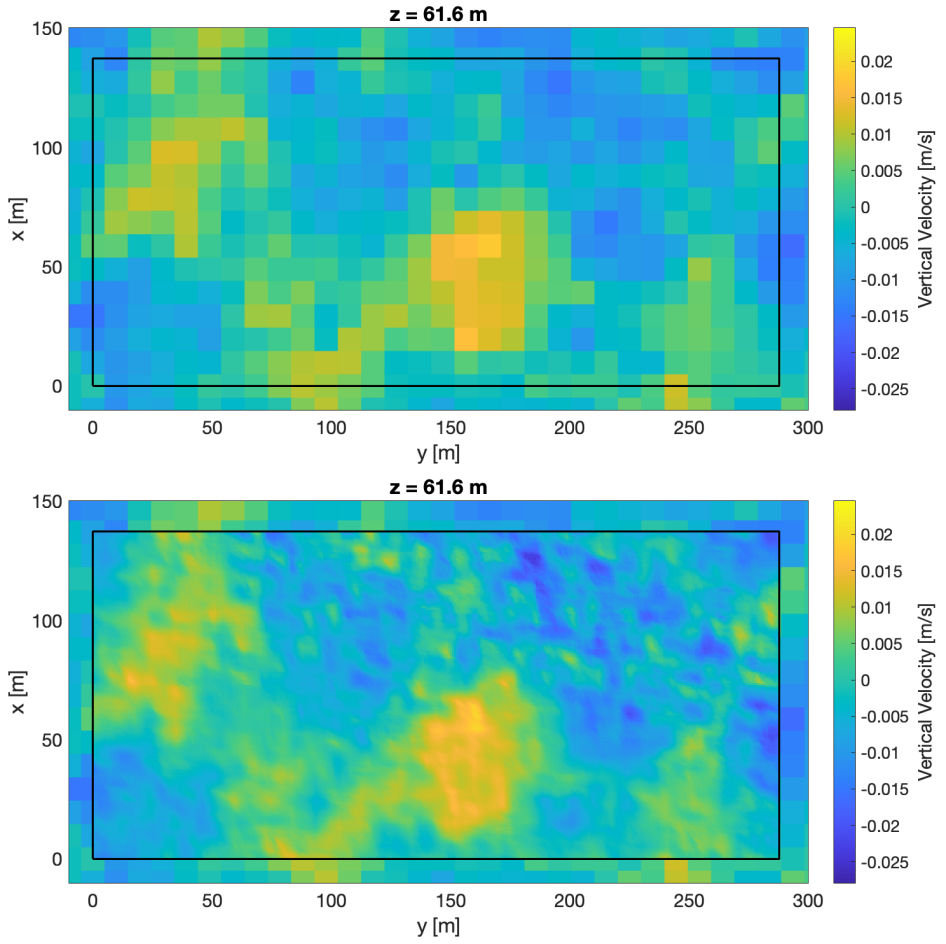

Figure 6.5: Horizontal slice of vertical velocity (top) GMIW realization (bottom) after model merging.

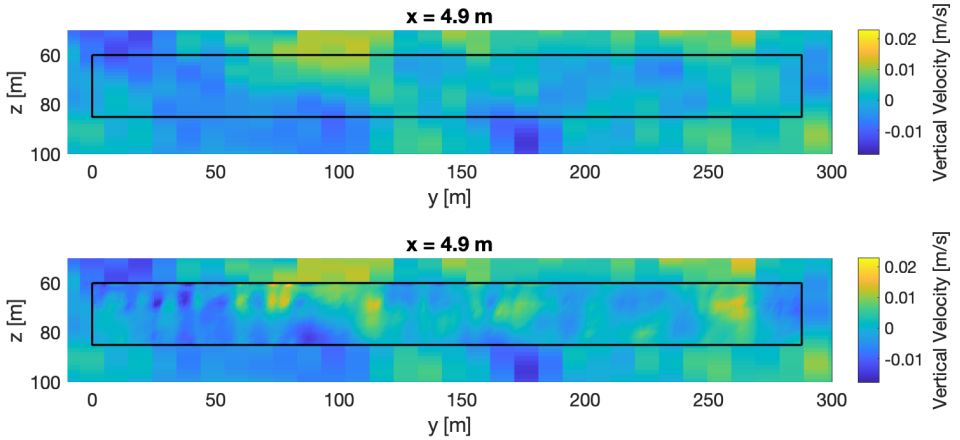

Figure 6.6: Vertical slice of vertical velocity (top) GMIW realization (bottom) after model merging.

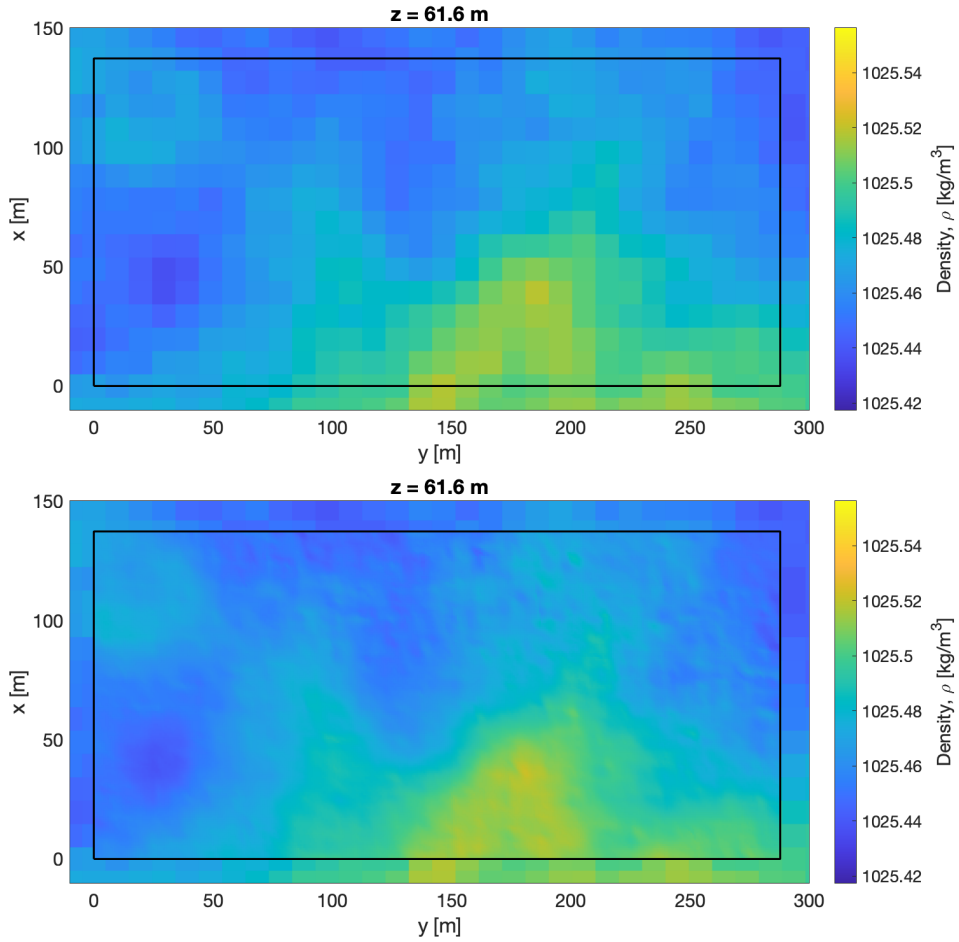

Figure 6.7: Horizontal slice of the density (top) GMIW realization (bottom) after model merging.

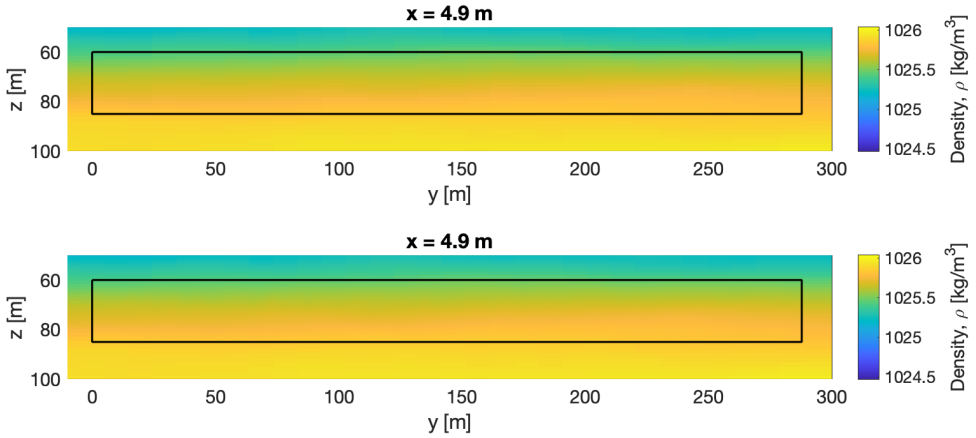

Figure 6.8: Vertical slice of the density (top) GMIW realization (bottom) after model merging.

(magenta line), and the MMLM+density tiled spectrum (blue line). Figure 6.10 shows the corresponding plot for the density spectra.

6.3 Run Time

The synthetic turbulence realization runs from start to finish in approximately 2.7 hours on a single processor. In comparison, a single time step of a Large Eddy Simulation (LES) code on a single processor takes 1.3 minutes for a 25 m x 25 m x 25 m grid. However, convergence typically takes 5000-10000 time steps such that a realization could take 4.5-9 days for a comparable output. The turbulence realization generated by this work therefore has a significantly reduced computational cost (40-80x reduction) over a larger grid (300 m x 300 m x 25 m) when compared with more traditional Large Eddy Simulation (LES) modeling techniques.

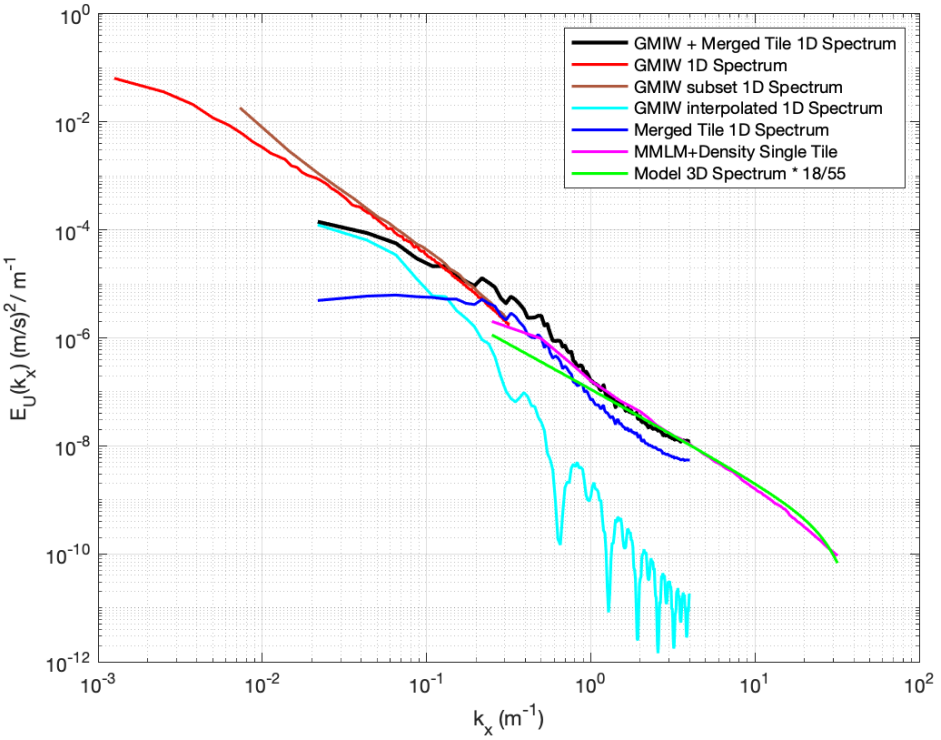

Figure 6.9: Vertical slice of the density (top) GMIW realization (bottom) after model merging.

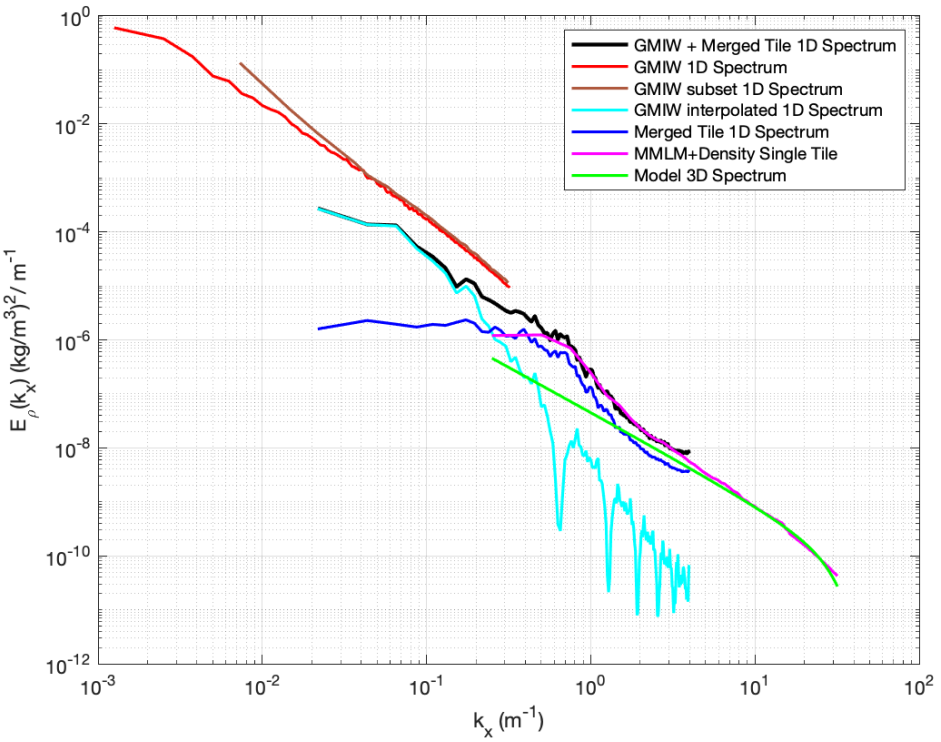

Figure 6.10: Vertical slice of the density (top) GMIW realization (bottom) after model merging.

Intended to be blank.

Chapter 7

Data Comparison

7.1 Overview

Data from a probe chain is used to compare against the synthetic turbulence realization results. Measurements were made in July in the North Sargasso Sea. The chain has 26 FP07 thermistors which are used to measure the ambient ocean temperature, 3 electromagnetic based sensors which are used to measure the ambient ocean velocity fluctuations, and 4 pressure sensors which are used to measure the chain depth and infer the depth of each of the sensors. These sensors cover a span of 25 m ranging from approximately 60 m to 85 m. The probe data are down-sampled to 5 Hz which is consistent with the synthetic turbulence realization spacing (based on the tow speed of the chain). Figure 7.1 shows an example chain track colored by time.

An expendable conductivity, depth, temperature (XCTD) probe was cast during the probe chain data acquisition from which a BV frequency profile can be calculated, where the BV frequency, N, is defined according to Equation 4.1. The in-situ BV frequency profile is compared to the BV frequency profile used in the GMIW realization from which the synthetic turbulence realization parameters are derived (Figure 7.2). The pink shaded region of Figure 7.2 highlights the depth band used in the synthetic turbulence realization and demonstrates that the modeled profile has good agreement with the profile used for comparison, particularly in the depth band of interest.

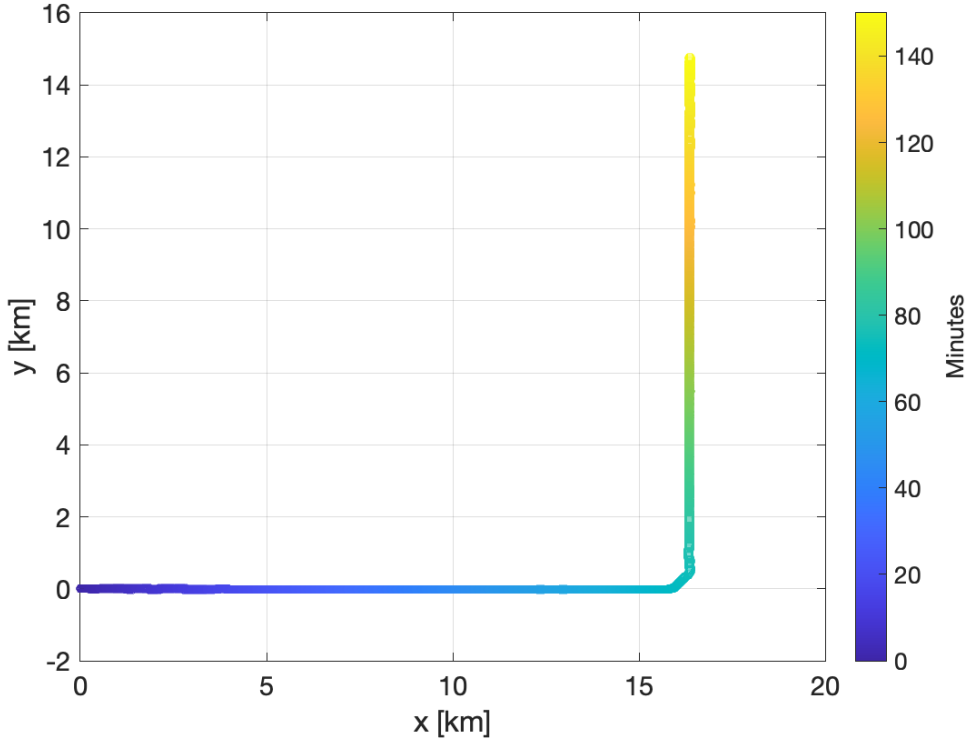

Figure 7.1: Chain track colored as a function of time.

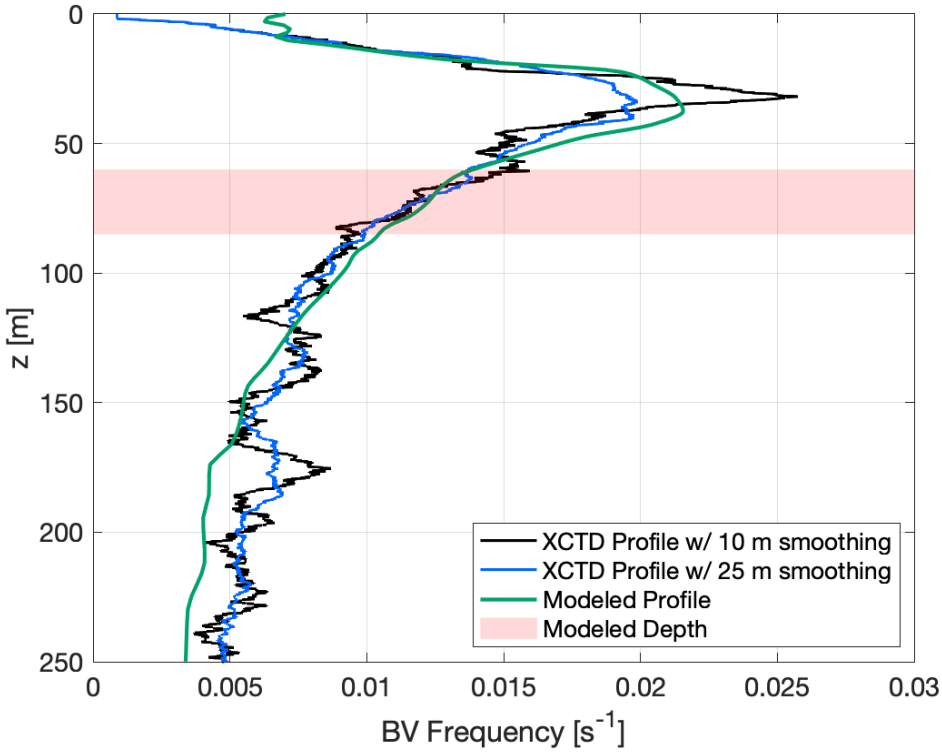

Figure 7.2: In-situ BV profile compared to BV frequency profile used in GMIW realization.

7.1.1 FP07 Thermistors

FP07 thermistors are a common type of fast response precision thermistor. A thermistor is a resistor whose resistance is dependent on the temperature, often made from a metal oxide pressed into a bead and encapsulated with an impermeable material [42]. The thermistors used here are potted in epoxy.

The FP07s used on the probe chain are Negative Temperature Coefficient (NTC) thermistors, meaning when the temperature increases, resistance decreases and vice versa. In contrast, a Positive Temperature Coefficient (PTC) thermistor measures an increase in resistance with an increase in temperature. [42]

The resistance (raw units) measured by an FP07 is converted into a temperature (engineering units) through a calibration equation.

7.1.2 Electromagnetic Sensors

Electromagnetic velocity probes measure the three components of ocean velocity fluctuations (u_f, v_f, and w_f), based on the principle of electromagnetic induction. Four magnets are located symmetrically on the electromagnetic velocity probe tip which generate a magnetic field. Interaction between the flow of conductive salt water and the magnetic field induces an electric field which is measured by four electrodes placed in the spaces between the four tip magnets. The potentials measured by the electrodes are then proportional to the different components of the fluctuating velocity field. [43, 44]

The potentials (raw units) measured by the electromagnetic velocity probes are converted to velocity (engineering units) through a calibration equation with laboratory measured coefficients. However, the orientation of the velocity sensors due to the catenary and rotation of the chain makes rectifying the measured velocities difficult. Velocity data comparison is therefore limited to looking at the summation of the spectra of each of the three components and the average gradients, as discussed in Section 7.3.2.

The electromagnetic sensors are paired with vibrational acceleration sensors, used for coherent motion removal. Discussion of the coherent motion removal is beyond the scope of this document.

7.1.3 Pressure Sensors

Depth measurements are derived from measurement of hydrostatic pressure via a pressure transducer. A pressure transducer is a type of strain gauge where the electrical resistance varies with changes in strain. Strain is defined as the deformation or displacement of material resulting from an applied pressure.

7.1.4 Density Calculation

The density of water is known to be a function of temperature, salinity, and pressure. It is assumed that the probe data were acquired in a thermally driven environment in which the salinity is effectively constant, set to 35 psu. The SEAWATER MATLAB toolbox is used to calculate the density [45]. Figure 7.3 shows the density field (bottom) which is calculated from the temperature field (top).

7.2 Data Preparation

7.2.1 Application of Taylor's Hypothesis of Frozen Turbulence

The probe data is acquired with a constant sampling rate. Data are converted from a function of time to a function of distance by using Taylor's hypothesis of frozen turbulence which allows for the conversion of time lags into spatial displacements [24, 46]. Figure 7.4 shows a sample data segment over 40 minutes. The speed is near constant over this time with minor fluctuations.

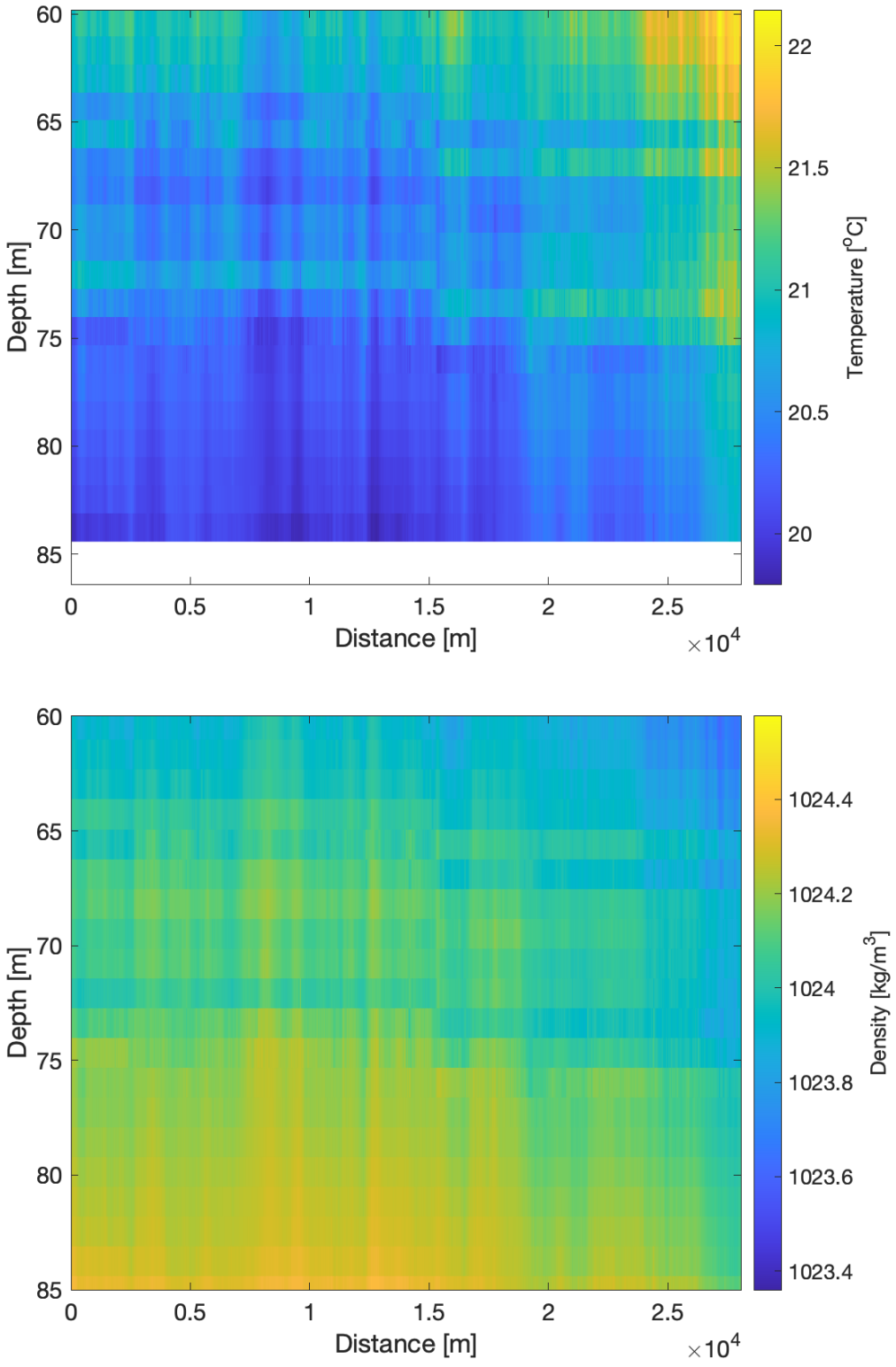

Figure 7.3: (Top) Temperature field and (bottom) density field.

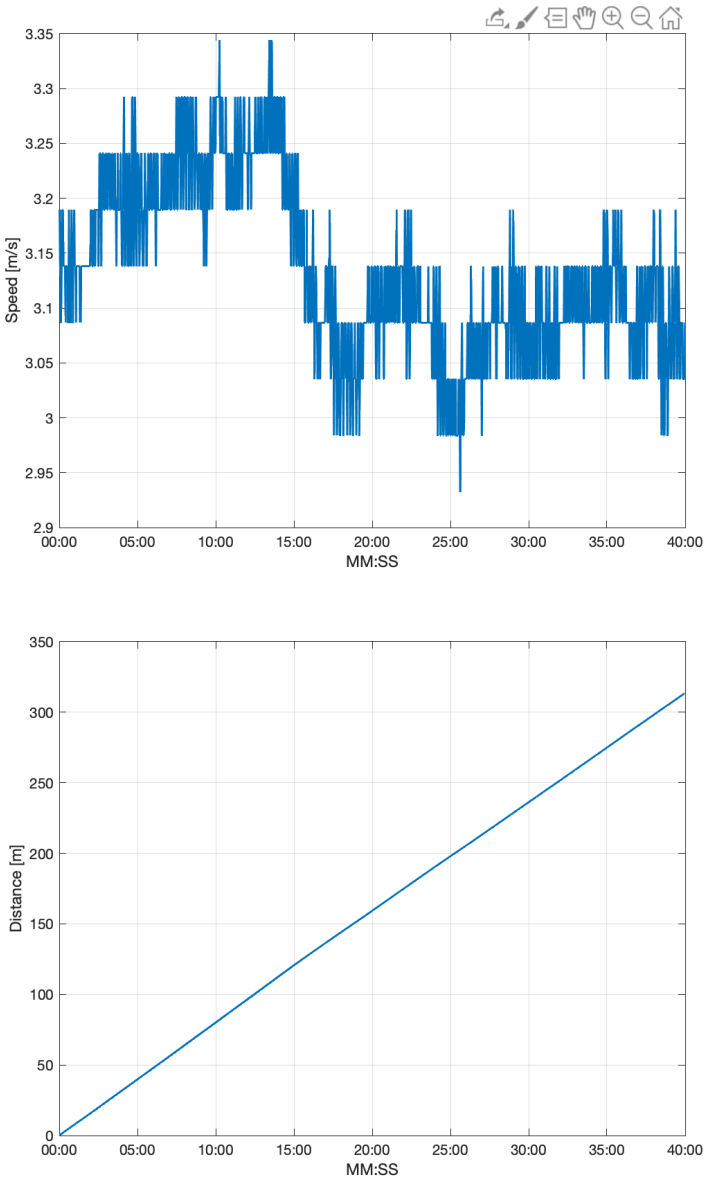

Figure 7.4: (Left) Speed of advance of the towed probes can be used to (right) convert from time to distance via Taylor's hypothesis of frozen turbulence.

7.2.2 Catenary Calculation

The probe chain has a natural catenary shape and does not hang straight down. Catenary is the curve formed by a rope, chain, or wire hanging freely from two points and has the form

$$z = a \cosh\left(\frac{x}{a}\right). \tag{7.1}$$

However, the catenary of the probe chain is due to the upward buoyancy of the chain as opposed to a downward gravitational force as observed in architecture and suspension bridges. Figure 7.5 shows a diagram of the chain's catenary reproduced from Linklater (2005) [47]. The chain's catenary shape is a function of the drag along the chain, the instantaneous tow speed, the mass distribution of the chain, the downward lift force of the depressor, and deployment depth and ocean current.

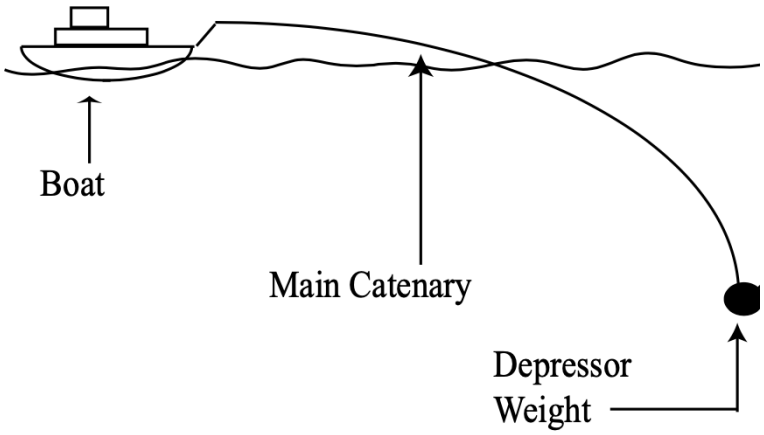

Figure 7.5: The probe chain has a natural catenary shape. Reproduced from Linklater (2005) [47].

The depth measurements (pressure probes) are used to calculate the catenary of the chain using a least squares fit method and a quadratic approximation. Wade (2010) shows how a quadratic approximation is a very good fit for the St. Louis Arch (a natural catenary shape) [48]. Hatibovic, Kádár, and Morva (2020) demonstrate how a parabola with inclined spans can approximate catenary curves, as applicable to powerlines [49].

The least squares parabolic fits are constructed from the depth sensor data, as a function of sensor position (arc length) along the chain and time. The position of the temperature sensors as a function of time then are obtained from the fit. The results indicate that depth versus sensor position is only slightly non-linear, and therefore a quadratic fit is a reasonable functional form. Once the depths are obtained for the temperature sensors, they are interpolated to a regularly spaced grid. Figure 7.6 shows example temperature probe data where the top graphic shows the measured temperature as a function of raw probe index and time, the middle graphic shows the same data with the depth values calculated from the catenary, and the bottom graphic shows the data interpolated on a regular grid of horizontal distance and depth.

7.2.3 Detrending

Trends in data can distort spectral analysis. Removing low frequency fluctuations which are unrelated to the desired signal and below the first frequency of the power spectral density calculation is a critical step for spectral analysis. If left in the data, trends and non-zero means could cause spectral leakage and affect the calculated spectrum [50]. Spectral leakage refers to when energy from one wavenumber is observed in other wavenumbers [51, 52]. This phenomenon is caused by windowing, and influenced by the sampling period [51]. A discussion on windowing follows in Section 7.2.4.

The density spectra are calculated horizontally with detrended data by removing the mean (constant detrend) and a linear detrend for each depth slice. When referring to detrending, the entire time series is detrended vice each segment. Figures 7.7 and 7.8 demonstrate why both are necessary by looking at the effects on the temperature timeseries data. In Figure 7.7, the original temperature data after interpolation is shown in (a), the data with constant detrend only are shown in (b), the data with only a linear detrend are shown in (c) and the data with both constant and linear detrends are shown

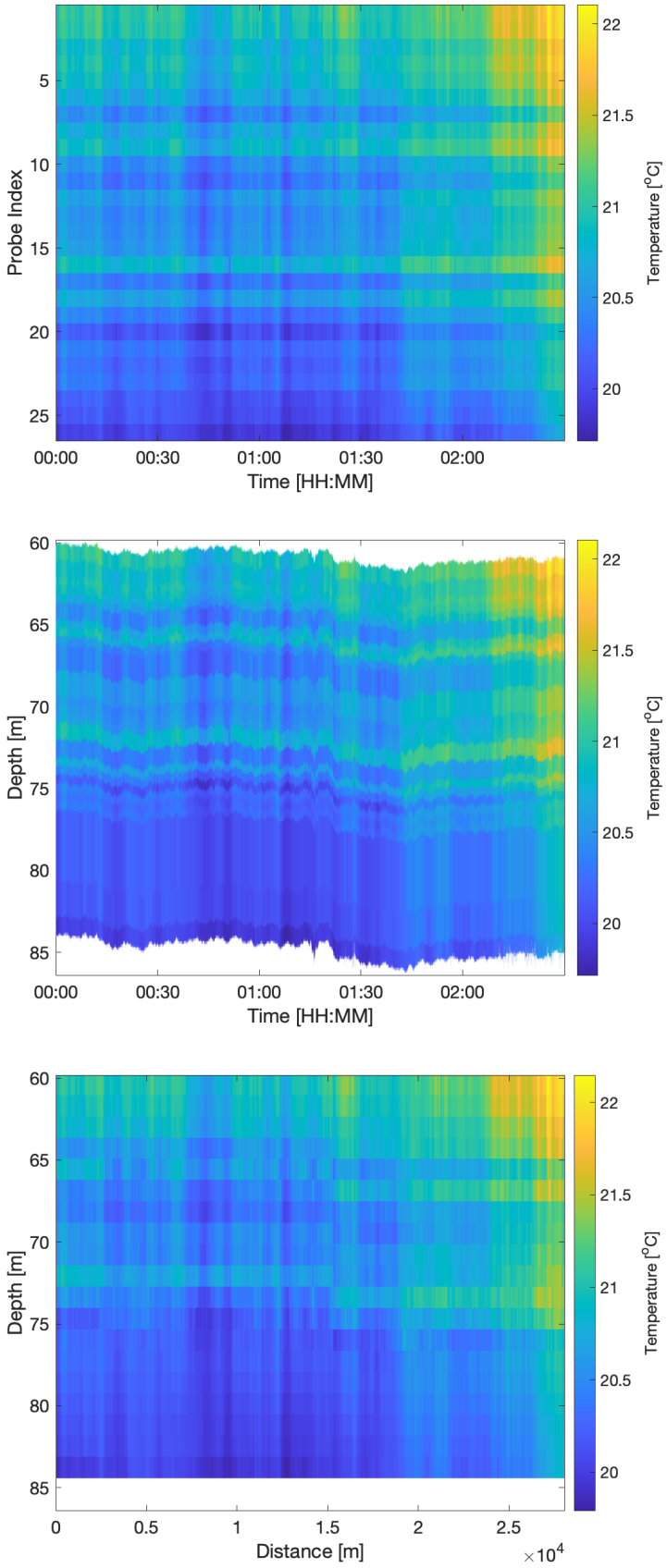

Figure 7.6: Example temperature probe data (top) shows the measured temperature as a function of raw probe index and time, (middle) shows the same data with the depth values calculated from the catenary, and (bottom) shows the interpolated data as a function of distance.

in (d). The constant detrend flattens the data over depth, but a horizontal trend can still be observed (Figure 7.7b). The linear detrend flattens each depth horizontally, but vertical gradation is still evident (Figure 7.7c). Doing both the constant and linear detrend is successful at removing any trends both horizontally and vertically in the data (Figure 7.7c). The same can be observed in Figure 7.8 which examines only one depth.

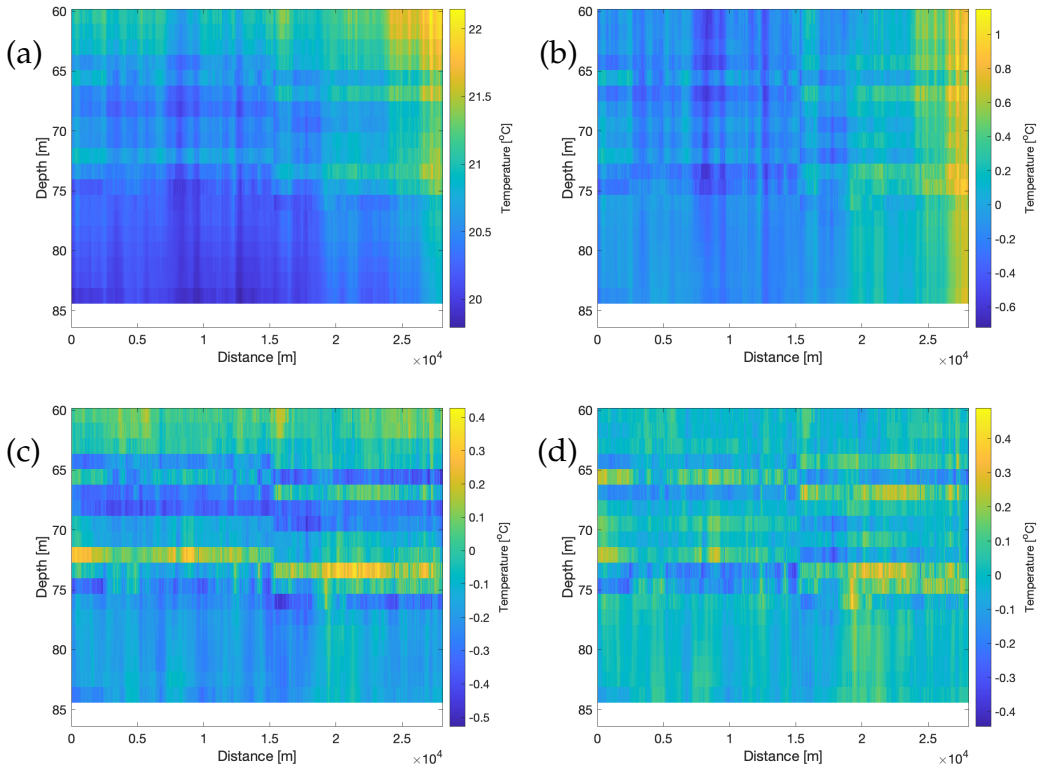

Figure 7.7: Detrend example (a) shows the original temperature data after interpolation (b) shows the data with constant detrend (c) shows the data with linear detrend and (d) shows the data with both constant and linear detrends.

7.2.4 Windowing

A window function is a weighted mathematical function with finite duration that usually tapers smoothly to zero at the boundaries, has a maximum value in the middle, and is symmetric [51]. The window and the fast Fourier transform (FFT) are applied to overlapping segments, typically overlapped 50% – 75%, to avoid loss of data as a result of the window tapering at the boundaries [51].

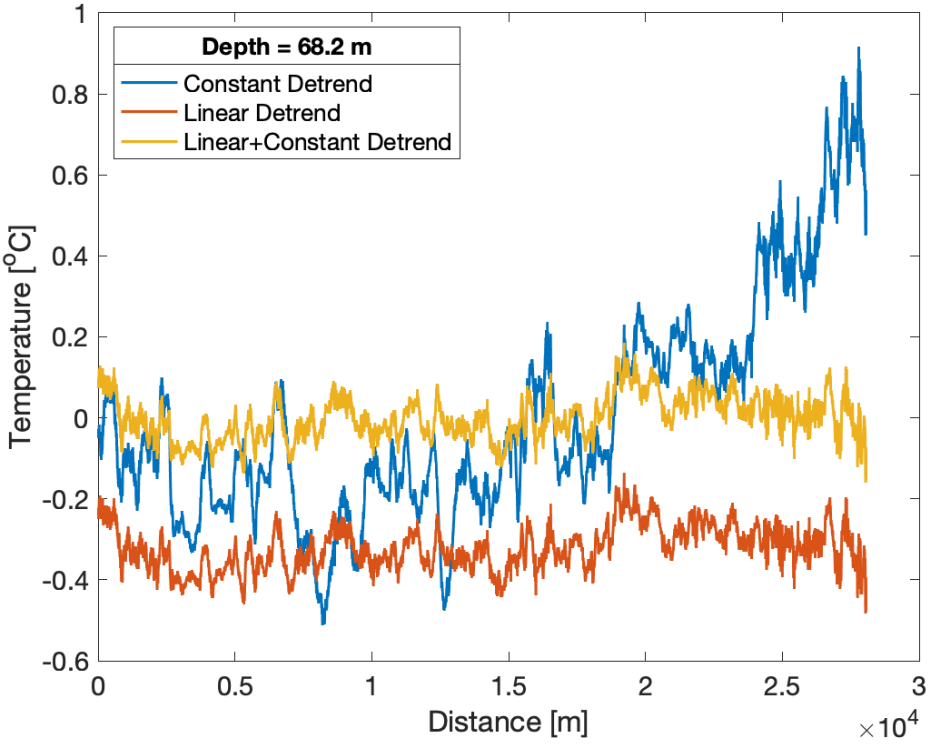

Figure 7.8: Detrend example for a single depth showing the difference between constant detrend (blue), linear detrend (red), and both a constant and linear detrend (yellow).

There are many commonly used windows. Two which are used in this analysis are the rectangular window (also sometimes called a Boxcar, constant, uniform, or Dirichlet window), and the Hann window (also sometimes called a Hanning window). Specialized window design (filter design) is also possible, although was not explored here.

Spectral leakage is caused by segmenting and windowing non-infinite data and can lead to biases in the calculated spectrum. Spectral leakage can be reduced by using windows with low-amplitude sidelobes as compared to the main lobe [51]. Window functions distribute the spectral leakage in different ways, such that window selection is dependent on the particular application and data analyzed [52].

Table 7.1 compares statistics for rectangular and Hann windows provided by Harris (1978) [51]. The table shows the rectangular window has a narrower main lobe (3.0-dB Bandwidth, 6.0-dB Bandwidth), although the highest

sidelobe is lower with the Hann window and falls off more quickly than for the rectangular window.

Table 7.1: Window function characteristics for the rectangular and Hann windows, as defined by Harris (1978) [51].

Window	Highest Sidelobe Level [dB]	Sidelobe Fall Off [dB/octave]	3.0-dB Bandwidth [bins]	6.0-dB Bandwidth [bins]	Equivalent Noise Bandwidth [bins]	Coherent Gain	Scallop Loss [dB]	Worst Case Process Loss [dB]	75% Overlap Correlation [percent]	50% Overlap Correlation [percent]
Rectangular	-13	-6	0.89	1.21	1.00	1.00	3.92	3.92	75.0	50.0
Hann	-32	-18	1.44	2.00	1.50	0.50	1.42	3.18	65.9	16.7

The equivalent noise bandwidth is a measure of the accumulated noise in the spectrum as a result of using the window of interest as compared to the results of a rectangular window (by definition, this value is 1 for the rectangular window) [51].

The coherent gain (also referred to as processing gain) is the summation of the window elements divided by the number of points in the window, M

$$\frac{1}{M}\sum_{m}^{M} w(m) \tag{7.2}$$

such that the rectangular window has a value of 1 and the Hann window has a lower coherent gain due to the tapering near the boundaries [51]. Note that a large equivalent noise bandwidth indicates a reduced coherent gain.

Scalloping loss represents the maximum reduction in coherent gain due to the signal frequency and the worst case processing loss is the reduction of signal to noise as a function of the window and signal frequency. According

to Harris (1978), the worst case processing loss is always between 3.0 and 4.3 dB and windows with worse case processing loss over 3.8 dB should not be used [51]. Based on this guidances, the rectangular window is not considered a good window (with a worst case process loss of 3.93 dB), largely resulting from the lack of tapering at the boundaries.

The correlation of successive transforms when using either 75% or 50% overlap is also listed in Table 7.1. The rectangular and Hann windows are nearly identical when using 75% overlap, but the Hann window has somewhat lower correlation at 50% overlap [51].

The rectangular window has high resolution (narrowest main lobe) and works well if the signal spectrum is flat or broadband in frequency content [53]. The Hann window is one of the most commonly used windows and can reduce the effect of spectral leakage [52, 53]. The velocity data spectra are calculated with a Hann window while the density data are calculated with a rectangular window.

7.3 Results

7.3.1 Comparison of Density Statistics

Figure 7.9 shows the probe density spectrum mean calculated over the entire depth (plotted as a thick black line) and averaged over 5 m depth bands for 15 minutes worth of data. The depth bands show there is no clear-cut trend in the energy based on depth (different color lines).

Figure 7.10 shows the comparison of the mean probe spectrum from Figure 7.9 and the synthetic turbulence realization output spectrum when $p = -\frac{5}{3}$, where p is the slope of the wavenumber in the prescribed energy spectrum used in MMLM+density. Agreement of the data and synthetic data is quite good.

Figure 7.11 shows the probability distribution function (PDF) for the

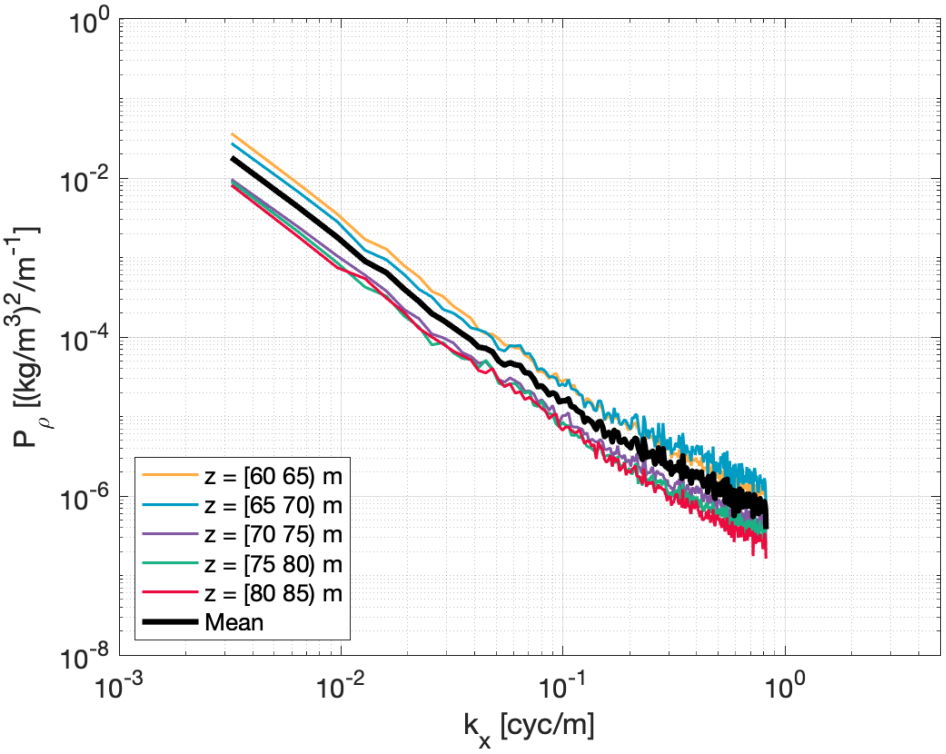

Figure 7.9: Probe density spectrum is calculated over the entire depth (mean) and over 5 m depth bands.

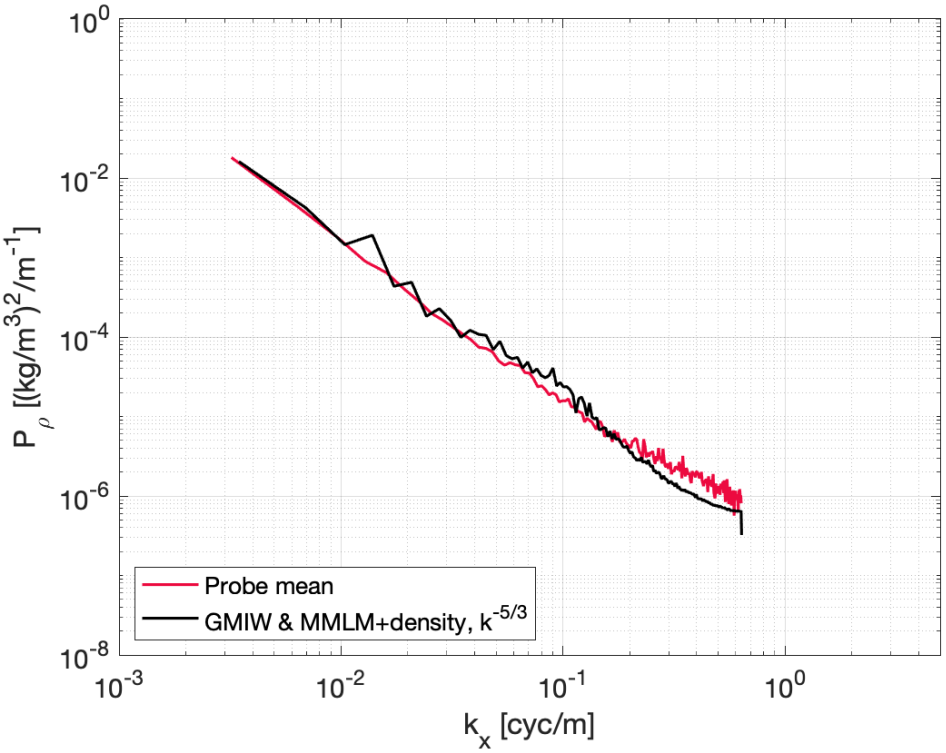

Figure 7.10: Density spectra for the probe data (red) compared with the synthetic realization (black).

density gradient according to Equation 3.37

$$\frac{\partial_\beta \rho}{\left\langle \left(\partial_\beta \rho\right)^2 \right\rangle^{1/2}}$$

where $\beta = \langle 1, 2 \rangle$ for horizontal and $\beta = 3$ for vertical gradients. The PDF of the density gradient for the initial Gaussian density field used in a single tile MMLM+density is shown for reference. The probe data and synthetic realization results show non-Gaussian behavior with broad, non-symmetric tails in the PDF, coinciding with more frequent occurrences of intense density gradients for both the horizontal and vertical derivatives.

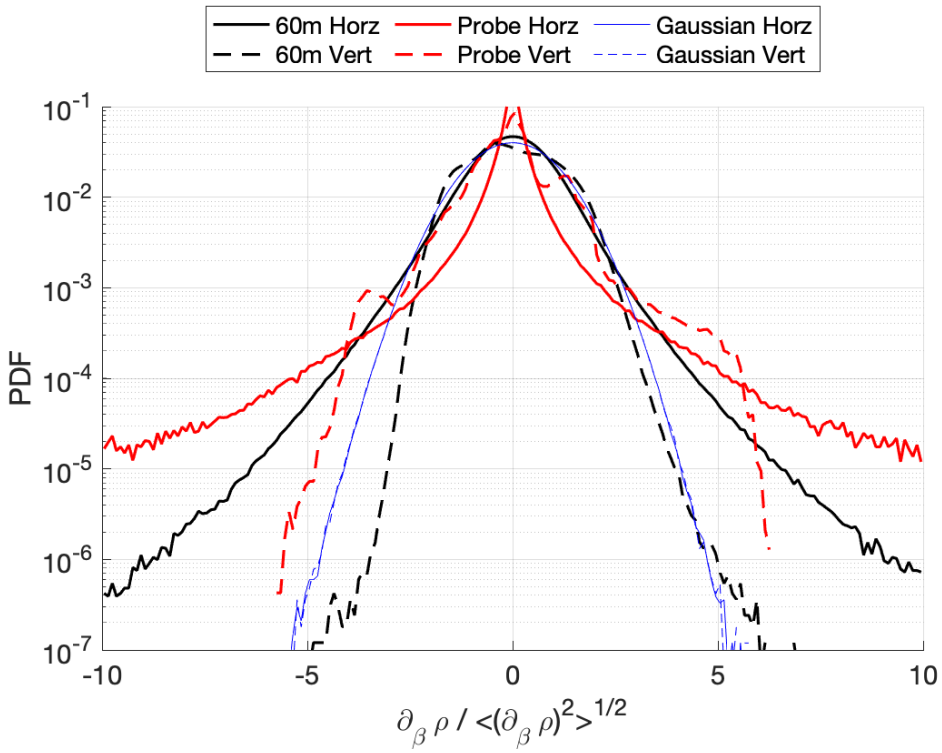

Figure 7.11: Density gradient.

7.3.2 Comparison of Velocity Statistics

Figure 7.12 shows the probe velocity spectrum after coherent motion removal and the synthetic turbulence realization output spectrum when $p = -\frac{5}{3}$. The sum of energy spectra in all three directions is plotted because the orientation of the velocity sensors are unknown both in relation to the xyz plane and to

each other.

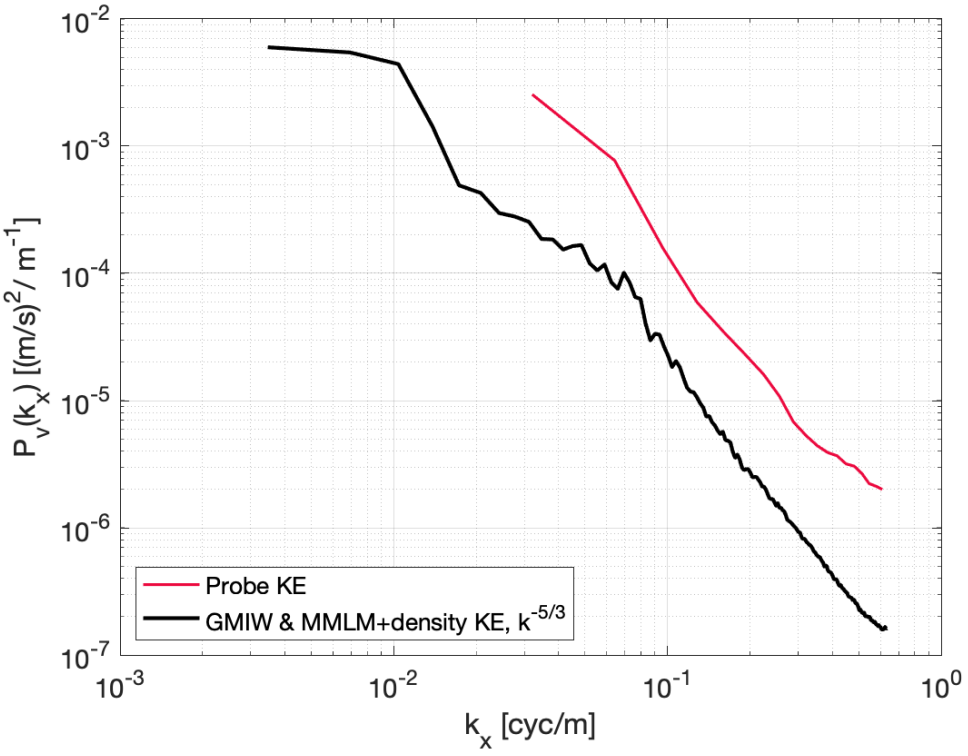

Figure 7.12: Velocity spectra for the probe data (red) compared with the synthetic realization (black).

Figure 7.13 shows the average of the 9 PDFs of the velocity gradient tensor for the synthetic realization data in black, calculated via Equation 3.36

$$\frac{\partial_\beta u_\alpha}{\left\langle \left(\partial_\beta u_\alpha\right)^2 \right\rangle^{1/2}}.$$

The probe data gradient PDF is calculated as the average of the 9 PDFs of the velocity gradients: 3 velocity sensors, each with 3 components. Because of the sensor orientation ambiguity, only the average PDF is considered here vice separating for horizontal and vertical or longitudinal and transverse PDFs. Additionally, the coherent motion removal is calculated on the spectrum and the velocity data used here includes ship motion, wave slap, and other vibrational effects. The PDF of the average velocity gradient for the initial Gaussian density field used in a single tile MMLM+density is shown for reference (averaged over the 9 PDFs of the velocity gradient tensor). The

velocity probe data in Figure 7.13 looks more symmetric and has lower tails than the density data, although that may be an artifact of the coherent motions and not the ambient ocean velocities.

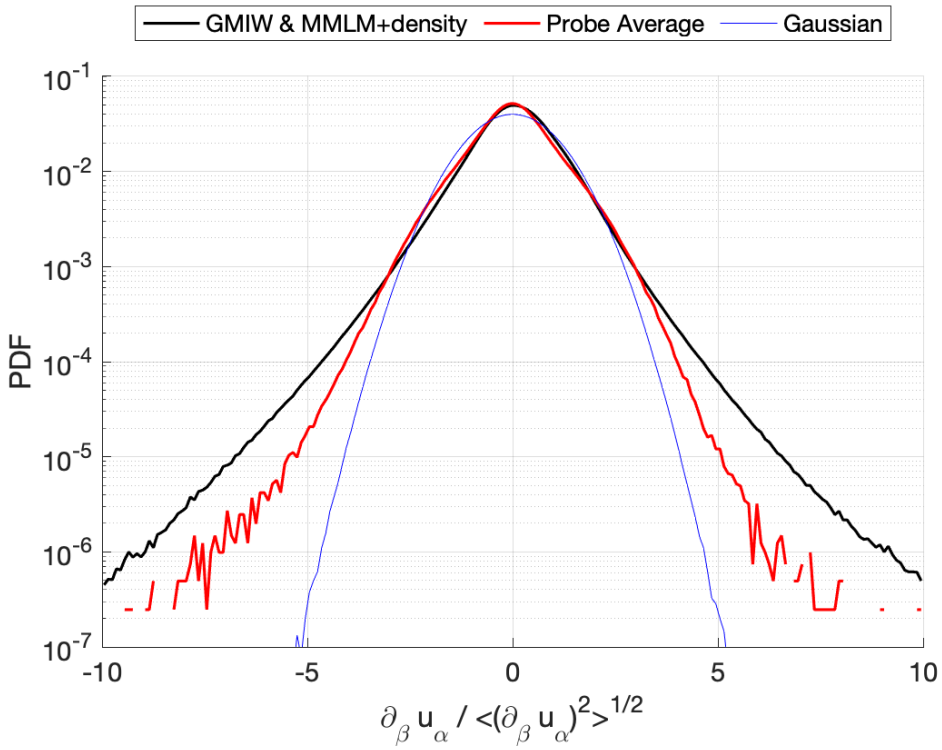

Figure 7.13: Velocity gradient.

Intended to be blank.

Chapter 8

Summary and Conclusions

A synthetic turbulence realization was developed which captures the intermittency and non-Gaussianity of ocean velocity turbulence and scalar microstructure. It builds upon existing models, adds complexity, and crosses multiple scales. The resulting realization has <1 m horizontal and 10 cm vertical spacing and covers 300 m horizontally x 300 m horizontally x 25 m deep.

The turbulence predictions were favorably compared to ocean data where similar gradients and comparable spectra were observed in both the synthetic turbulence realization and probe data. The realization can be used to increase the understanding of ocean turbulence. Three dimensional velocity and density fields can be generated with this methodology with ocean conditions of interest in lieu of acquiring ocean field measurements (which can also have unpredictable conditions, for example after fronts with large mixing events may have passed). This method is less costly than acquiring data (most expensive) and than using more traditional computational methods such as a LES code.

The synthetic realization method discussed here is expandable to larger regions by increasing the number of tiles overlaid in any particular direction. While not done as part of this work, there is nothing that prevents the method from being applied to tile vertical tiling as well. This work could also be expanded to create a set of overlapping realizations to generate realistic

looking movies or a series of snapshots of ocean data.

The number of tiles needed was not explored in detail; it may be of potential interest to develop metrics for how many tiles are needed to maintain the synthetic turbulence realization fidelity shown here. For example, if one tile is sufficient, this would further reduce the computation time and cost benefits of this method. If multiple tiles are still needed, then one might ask what is the right ratio for the number of unique realizations to overlapping tiles.

While this method is expandable to different grid resolutions, it should be noted that the resolution of the GMIW will also then need to be adjusted accordingly. The largest wavenumber from the GMIW realization (smallest scales) was approximately the smallest wavenumber of the MMLM+density realization (largest scales). This allowed for the simple addition methodology discussed in Chapter 6.

References

[1] W. Munk. "Evolution of Physical Oceanography, Scientific Surveys in Honor of Henry Stommel". In: ed. by B. A. Warren and C. Wunsch. MIT textbook, 1981. Chap. 9 Internal Waves and Small-Scale Processes.

[2] J. Callies. "Submesoscale turbulence in the ocean". Doctor of Philosophy. MIT, 2016.

[3] J. C. McWilliams. "Submesoscale currents in the ocean". In: *Proceedings of the Royal Society A* 472 (2016). DOI: 10.1098/rspa.2016.0117.

[4] A. Mahadevan and A. Tandon. "An analysis of mechanics for submesoscale vertical motion at ocean fronts". In: *Ocean Modelling* 14 (2006). DOI: 10.1016/j.ocemod.2006.05.006.

[5] J. C. McWilliams. "A survey of submesoscale currents". In: *Geoscience Letters* 6 (3 2019). DOI: 10.1186/s40562-019-0133-3.

[6] Y. Desaubies and M. C. Gregg. "Reversible and Irreversible Finestructure". In: *Journal of Physical Oceanography* 11 (1981). DOI: 10.1175/1520-0485(1981)011<0541:RAIF>2.0.CO;2.

[7] C. Meneveau and K. R. Sreenivasan. "The multifractal nature of turbulent energy dissipation". In: *J. Fluid Mech* 224 (1991). DOI: 10.1017/S0022112091001830.

[8] J. S. Turner. "Oceanic Fine- and Microstructure". In: *Oceanography*. Ed. by Peter G. Brewer. New York, NY: Springer US, 1983.

[9] C. Rosales and C. Meneveau. "Anomalous scaling and intermittency in three-dimensional synthetic turbulence". In: *Physical Review E* 78 (2008). DOI: 10.1103/PhysRevE.78.016313.

[10] J. M. Klymak and J. N. Moum. "Oceanic Isopycnal Slope Spectra. Part I: Internal Waves". In: *Journal of Physical Oceanography* 37 (2007). DOI: 10.1175/JPO3073.1.

[11] I. P. D. DeSilva, A. Brandt, L. J. Montenegro, and H. J. S. Fernando. "Gradient Richardson number measurements in a stratified shear layer". In: *Dynamics of Atmospheres and Oceans* 30 (1 1999). DOI: 10.1016/s0377-0265(99)00015-9.

[12] S. A. Thorpe and R. Jiang. "Estimating internal waves and diapycnal mixing from conventional mooring data in a lake". In: *Limnology and Oceanography* 43(5) (1998). DOI: 10.4319/lo.1998.43.5.0936.

[13] D. E. Kelley, H. J. S. Fernando, A. E. Gargett, J. Tanny, and E. Özsoy. "The diffusive regime of double-diffusive convection". In: *Progress in Oceanography* 56 (2003). DOI: 10.1016/S0079-6611(03)00026-0.

[14] R. Schmitt. "Double Diffusion in Oceanography". In: *Annual Review of Fluid Mechanics* 26 (1994). DOI: 10.1146/annurev.fl.26.010194.001351.

[15] R. Stressing and J. Peinke. "Towards a stochastic multi-point description of turbulence". In: *New Journal of Physics* 12 (2010). DOI: 10.1088/1367-2630/12/10/103046.

[16] D. K. Wilson. "Turbulence Models and the Synthesis of Random Fields for Acoustic Wave Propagation Calculations". In: *Army Research Laboratory* ARM-TR-1677 (1998).

[17] C. Rosales and C. Meneveau. "A minimal multiscale Lagrangian map approach to synthesize non-Gaussian turbulent vector fields". In: *Physics of Fluids* 18 (2006). DOI: 10.1063/1.2227003.

[18] J. A. Colosi. *Sound Propagation through the Stochastic Ocean*. New York, NY: Cambridge University Press, 2016. Chap. 3.

[19] C. Rosales. "Synthetic three-dimensional turbulent passive scalar fields via the minimal Lagrangian map". In: *Physics of Fluids* 23.075106 (2011). DOI: 10.1063/1.3609280.

[20] C. Garrett and W. Munk. "Space-Time Scales of Internal Waves: A Progress Report". In: *Journal of Geophysical Research* 80.3 (1975). DOI: 10.1029/JC080i003p00291.

[21] C. Garrett and W. Munk. "Internal Waves in the Ocean". In: *Annual Review of Fluid Mechanics* 11 (1979). DOI: 10.1146/annurev.fl.11.010179.002011.

[22] K. L. Polzin and Y. V. Lvov. "Toward Regional Characterizations of the Oceanic Internal Wavefield". In: *Reviews of Geophysics* 49 (2011). DOI: 10.1029/2010RG000329.

[23] J. M. Klymak.

[24] S. B. Pope. *Turbulent Flows*. Cambridge University Press, 2000.

[25] B. I. Shraiman and E. D. Sigga. "Scalar Turbulence". In: *Nature* 405 (2000). DOI: 10.1038/35015000.

[26] W. D. Smyth and J. N. Moum. "Length scales of turbulence in stably stratified mixing layers". In: *Physics of Fluids* 12.6 (2000). DOI: 10.1063/1.870385.

[27] E. Kunze, A. j. Williams III, and M. G. Briscoe. "Observations of Shear and Vertical Stability from a Neutrally Buoyant Float". In: *Journal of Geophysical Research* 95.C10 (1990).

[28] K. L. Polzin. "Statistics of the Richardson Number: Mixing Models and Finestructure". In: *Journal of Physical Oceanography* 26 (8 1996).

[29] H. Tennekes and J. L. Lumley. *A First Course in Turbulence*. MIT Oress, 1972.

[30] U. Frisch. *Turbulence: The Legacy of A. N. Kolmogorov*. Cambridge, England: Cambridge University Press, 1995. DOI: 10.1017/CBO9781139170666.

[31] E. C. Fine, J. A. MacKinnon, and M. H. Alford. "Microstructure Observations of Turbulent Heat Fluxes in a Warm-Core Canada Basin Eddy". In: *Journal of Physical Oceanography* 48 (2018). DOI: 10.1175/JPO-D-18-0028.1.

[32] B. S. Chinn, J. B. Girton, and M. H. Alford. "The Impact of Observed Variations in the Shear-to-Strain Ratio of Internal Waves on Inferred Turbulent Diffusivities". In: *Journal of Physical Oceanography* (2016).

[33] S. A. Thorpe. *An Introduction to Ocean Turbulence*. Cambridge University Press, 2007.

[34] D. Li, S. T. Salesky, and T. Banerjee. "Connections between the Ozmidov scale and mean velocity proïňĄle in stably stratiiňĄed atmospheric surface layers". In: *Journal of Fluid Mechanics* 797 (2016). DOI: 10.1017/jfm.2016.311.

[35] G. G. Katul, A. G. Konings, and A. Porporato. "Mean Velocity Profile in a Sheared and Thermally Stratified Atmospheric Boundary Layer". In: *Physical Review Letters* 107 (2011). DOI: 10.1103/PhysRevLett.107.268502.

[36] A. K. Peterson and I. Fer. "Dissipation measurements using temperature microstructure from an underwater glider". In: *Methods in Oceanography* 10 (2014). DOI: 10.1371/journal.pone.0229839.

[37] S. K. Lee, L. Djenidi, and R. A. Antonia. "Spectral method for determining mean dissipation rates of turbulent kinetic energy and passive scalar variance". In: *18th Australian Fluid Mechanics Conference* (2012).

[38] M. L. Waite. "Stratified Turbulence at the Buoyancy Scale". In: *Physics of Fluids* 23.066602 (2011). DOI: 10.1063/1.3599699.

[39] G. de Haan and V. Jeanne. "Robust Pulse Rate From Chrominance-Based rPPG". In: *IEEE Transactions on Biomedical Engineering* 60.10 (2013). DOI: 10.1109/TBME.2013.2266196.

[40] M. Fröjd and A. Horner. "Sound Texture Synthesis Using an Overlap-Add/Granular Synthesis Approach". In: *Journal of the Audio Engineering Society* 57.1/2 (2009).

[41] N. Pielawski and C. Wählby. "Introducing Hann windows for reducing edge-effects in patch-based image segmentation". In: *PLoS ONE* 15(3) (2020). DOI: 10.1016/j.mio.2014.05.002.

[42] *Thermistor Basics*. Application Note AN-TC11 Rev. A. Wavelength Electronics. 2013.

[43] D. Y. Lai, V. T. Paka, D. P. Delisi, A. V. Arjannikov, and S. A. Khanaev. "An Intercomparison Study Using Electromagnetic Three-Component Turbulent Velocity Probes". In: *Journal of Atmospheric and Oceanic Technology* 17 (2000). DOI: 10.1175/1520-0426(2000)017<0980:AISUET>2.0.CO;2.

[44] A. Soloviev, R. Luksd, S. DeCarlo, J. Snyder, A. Arjannikov, V. Turenko, M. Baker, and D. Khlebnikov. "A Near-Surface Microstructure Sensor System Used during TOGA COARE. Part I: Bow Measurements". In: *Journal of Atmospheric and Oceanic Technology* 15 (1998). DOI: 10.1175/1520-0426(1998)015<0563:ANSMSS>2.0.CO;2.

[45] *SEAWATER A Library of MATLAB Computational Routines for the Properties of Sea Water*. Report 222. Version 1.2. CSIRO Marine Laboratories. 1994. URL: https://github.com/ashao/matlab/tree/master/external/seawater.

[46] Ch. Renner, J. Peinke, R. Friedrich, O. Chanal, and B. Chabaud. "Universality of Small Scale Turbulence". In: *Physical Review Letters* 98(12) (2002). DOI: 10.1103/PhysRevLett89.124502.

[47] A. Linklater. "Design and Simulation of a Towed Underwater Vehicle". Master of Science. Virginia Polytechnic Institute, 2005.

[48] A. Wade. "Catenary Best Fit". In: *Ohio Journal of School Mathematics* 6 (2010).

[49] A. Hatibovic, P. Kádár, and G. Morva. "Comparison of the Length of the Catenary Curve and its Parabolic Approximation in the Span of an Overhead Line". In: *2020 IEEE 3rd International Conference and Workshop in Óbuda on Electrical and Power Engineering (CANDO-EPE)*. 2020. DOI: 10.1109/CANDO-EPE51100.2020.9337759.

[50] Z. Wu, N. E. Huang, S. R. Long, and C. Peng. "On the trend, detrending, and variability of nonlinear and nonstationary time series". In: *PNAS* 104(38) (2007). DOI: 10.1073/pnas.0701020104.

[51] F. J. Harris. "On the Use of Windows for Harmonic Analysis with the Discrete Fourier Transform". In: *Proceedings of the IEEE* 66.1 (1978). DOI: 10.1109/PROC.1978.10837.

[52] *The Fundamentals of Signal Analysis*. Application Note 243. Hewlett Packard.

[53] *Understanding FFTs and Windowing*. Instrument Fundamental Series. National Instruments. 2019.